POLITECHNIKA
GDAŃSKA

Author of the doctoral dissertation: Łukasz Macewicz
Scientific discipline: Automation, electronic and electrical engineering

DOCTORAL DISSERTATION

Title of doctoral dissertation: Structural, optical and electrochemical performance of black phosphorus and black arsenic-phosphorus nanostructures

Title of doctoral dissertation (in Polish): Właściwości strukturalne, optyczne i elektrochemiczne nanostruktur czarnego fosforu i czarnego arseno-fosforu

Supervisor *signature*
Prof. PhD, DSc EE, Robert Bogdanowicz,

ABSTRACT

Black phosphorus (BP)-based nanostructures have drawn a lot of attention due to their tunable bandgap and extraordinary properties such as: high surface-to-volume ratio, large number of active sites, and prominent edges. However, low dimensional structures of black phosphorus oxidize easily, which hamper their application on a broader scale. One way to overcome these difficulties is to modify the black phosphorus structure by substituting some of the phosphorus atoms for arsenic atoms, forming black arsenic-phosphorus (b-AsP). Despite the broad variety of atomically thin, two-dimensional materials, those with a bandgap range between 0.3 and 1.5 eV are plainly missing. Black phosphorus and black arsenic-phosphorus nanostructures not only correspond to the visible and infrared spectral range, but also possess additional tuning capabilities, which can further influence their electronic properties. In this dissertation, the structural and optical properties of BP and b-AsP nanoflakes and nanoribbons have been investigated. Moreover, surface modification of electrode materials with BP and b-AsP to enhance their electrochemical performance and sensing possibilities was investigated. The electrode materials chosen for BP and b-AsP modification were titania nanotubes (TiO_2 NTs), commercially available gold array electrodes, and CVD-fabricated polycrystalline boron-doped diamond (BDD) films.

STRESZCZENIE

Nanostruktury czarnego fosforu przyciągnęły wiele uwagi ze względu na przestrajalną przerwę energetyczną i właściwości, takie jak: wysoki stosunek powierzchni do objętości, duża liczba miejsc aktywnych i ostre krawędzie. Jednak niskowymiarowe struktury czarnego fosforu łatwo się utleniają, co utrudnia ich zastosowanie na szerszą skalę. Jednym ze sposobów ominięcia tych trudności jest modyfikacja struktury czarnego fosforu poprzez zastąpienie niektórych atomów fosforu atomami arsenu, tworząc czarny arseno-fosfor. Pomimo szerokiej gamy atomowo cienkich, dwuwymiarowych materiałów wyraźnie brakuje tych o zakresie pasma wzbronionego w przedziale 0,3-1,5 eV. Przerwa energetyczna nanostruktur czarnego fosforu i czarnego arseno-fosforu nie tylko odpowiada zakresowi widmowemu w zakresie widzialnym i podczerwonym, ale również ma możliwości strojenia, które może dodatkowo wpływać na ich właściwości elektroniczne. W niniejszej rozprawie zbadano właściwości strukturalne i optyczne nanopłatków i nanowstążek BP i b-AsP. Ponadto przeprowadzono modyfikację powierzchniową materiałów elektrodowych wykorzystując BP i b-AsP w celu zwiększenia ich wydajności elektrochemicznej i możliwości sensoryczne. Materiałami elektrodowymi wybranymi do modyfikacji BP i b-AsP były nanorurki z tlenku tytanu (IV), komercyjnie dostępne elektrody ze złotymi wzorami oraz cienka warstwa polikrystalicznego diamentu domieszkowanego borem wytwarzane metodą CVD.

TABLE OF CONTENTS

LIST OF FIGURES

LIST OF IMPORTANT SYMBOLS AND ABBREVIATIONS

2D	– Two-dimensional
AC	– Armchair
AFM	– Atomic force microscopy
ALD	– Atomic Layer Deposition
b-AsP	– Black arsenic-phosphorus
BP	– Black phosphorus
RP	– Red phosphorus
WP	– White phosphorus
BDD	– Boron-doped diamond
BZ	– Brillouin zone
CBM	– Conduction band minimum
CE	– Counter electrode
DMF	– N,N-dimethylformamide
DOS	– Density of states
DW-PNTs	– Double-walled phosphorene nanotubes
EDX	– Energy-dispersive X-ray spectroscopy
FET	– Field effect transistors
hBN	– Hexagon boron nitride
IR	– Infrared
MOF	– Metal-organic framework
MOSFET	– Metal–oxide–semiconductor field-effect transistors
NMP	– N-methyl-2-pyrrolidone
MW PA CVD	– Microwave plasma-assisted chemical vapor deposition
PDMS	– Polydimethylsiloxane
PLD	– Pulsed laser deposition
RE	– Reference electrode
SEAD	– Selected area (electron) diffraction
SEM	– Scanning electron microscope

SW-PNTs	– Single-walled phosphorene nanotubes
TEM	– Transmission electron microscope
TiO_2 NTs	– Titanium dioxide nanotubes
TMDCs	– Transition metal dichalcogenides
UV-Vis	– Ultraviolet-visible
VBM	– Valance band maximum
vdW	– Van der Walls
WE	– Working electrode
ZZ	– Zigzag

LIST OF PUBLICATIONS

1. M. R. Molas, **Ł. Macewicz**, A. Wieloszyńska, Paweł Jakóbczyk, A. Wysmołek, R. Bogdanowicz and J. B. Jasinsk, “*Photoluminescence as a probe of phosphorene properties*,” npj 2D Materials and Applications 5:83 (2021).
2. **Ł. Macewicz**, K. Pyrchla, R. Bogdanowicz, G. Sumanasekera, and J. B. Jasinski, “*Chemical Vapor Transport Route toward Black Phosphorus Nanobelts and Nanoribbons*,” The Journal of Physical Chemistry Letters 12 (34), 8347-8354 (2021).
3. Robert Bogdanowicz, Anna Dettlaff, Franciszek Skiba, Konrad Trzcinski, Mariusz Szkoda, Michal Sobaszek, Mateusz Ficek, B. Dec, **Ł. Macewicz**, Konrad Wyrębski, Grzegorz Pasciak, Dongsheng Geng, Arkadiusz Ignaczak, and Jacek Ryl, “*Enhanced Charge Storage Mechanism and Long-Term Cycling Stability in Diamondized Titania Nanocomposite Supercapacitors Operating in Aqueous Electrolytes*,” The Journal of Physical Chemistry C, 124, 29, 15698–15712 (2020).
4. M. Rycewicz, **Ł. Macewicz,** J. Kratochvil, A. Stanisławska, M. Ficek. M. Sawczak, V. Stranak, M. Szkodo and R. Bogdanowicz, “*Physicochemical and Mechanical Performance of Freestanding Boron Doped Diamond Nanosheets Coated with C:H:N:O Plasma Polymer*,” Materials, 13, 1861. (2020).
5. A. Dettlaff, G. Skowierzak, **Ł. Macewicz**, M. Sobaszek, J. Karczewski, M. Sawczak, J. Ryl, T. Ossowski, and R. Bogdanowicz. “*Electrochemical Stability of Few-Layered Phosphorene Flakes on Boron-Doped Diamond: A Wide Potential Range of Studies in Aqueous Solutions*,” The Journal of Physical Chemistry C, 123, 33, 20233–20240 (2019).
6. B. Dec, M. Ficek, M. Rycewicz, **Ł. Macewicz**, M. Gnyba, M. Sawczak, M. Sobaszek and R. Bogdanowicz. “*Gas Composition Influence on the Properties of Boron-Doped Diamond Films Deposited on the Fused Silica*” Materials Science-Poland, 36(2), pp. 288-296 (2018).

CHAPTER 1: Introduction, goals and hypotheses

1.1 Introduction to black phosphorus

Phosphorus is an element in the fifth group of the periodic table. It exists in a number of allotropic varieties, with black phosphorus being the most stable form. Black phosphorus (BP) is a layered crystalline material and was first discovered in 1914 by Bridgeman by conversion from white phosphorus (WP) at an elevated temperature of 200 °C and pressure of 1.2 GPa [1]. Bridgeman also measured the density, compressibility, and electrical resistivity of black phosphorus as a function of pressure in a limited range of temperatures. These studies revealed black phosphorus to be a semiconductor with possible conversion to a metallic character when under high hydrostatic pressure.

Similar results were reproduced by Keyes who, using similar method, fabricated polycrystalline BP with a grain size of around 0.1 mm [2]. Afterwards, Brown and Rundqvist discovered that black phosphorus can be synthesized using the mercury or bismuth-flux method. In this method, black phosphorus crystallizes in an orthorhombic form with an infinite, puckered layer structure [3]. Brown and Rundqvist purified white phosphorus with a 15% HNO_3 solution and subsequently dissolved it in liquid bismuth. The mixture was kept at 400°C for 20 hours then slowly cooled to room temperature. The liquid bismuth was dissolved with 30% HNO_3 leaving needle-like black phosphorus crystals.

For nearly 100 years, many variants of high pressure and flux methods were commonly used for black phosphorus fabrication until Lange and colleagues, who in 2007 reported a low-pressure route for high-quality black phosphorus fabrication using a mineralizer as a reaction promoter under non-toxic conditions [4]. This method was based on the reaction of Au, Sn, SnI_4, and red phosphorus (RP) in evacuated silica ampules. The precursors were kept in 600°C for several hours and gradually cooled to room temperature. This method was revised 6 years later by Köpf, who proposed using Sn and SnI_4 as the only mineralization agents [5]. The optimization of the chemical vapor transport method and growing interest in graphene, few-layered hexagon boron nitride (hBN), and transition metal dichalcogenides (TMDCs) have led to a rediscovery of BP as an interesting addition to thin film materials. In the following years, new and exciting properties of mono- and few-layer thin BP have been discovered and studied toward a spectrum of novel applications ranging from electronic, optoelectronic, and spintronic devices to sensors and batteries with a few thousands of papers published since 2014.

In ambient conditions, bulk BP has a layered structure, however, unlike group IV layered materials such as graphene, silicene, and germanene, there are five outer shell electrons for each phosphorus atom. Black phosphorus has three possible crystalline structures: rhombohedral, simple cubic, and orthorhombic, which attracts the most attention due to its affiliation to the D^{18}_{2h} point group with reduced symmetry compared to the IV group counterparts [6]. The unit cell of crystalline BP consists of two layers and eight atoms with lattice parameters a = 3.31 Å, b = 4.38 Å, and c = 10.50 Å, and were first determined by Hultgren et al. using X-ray crystallography [7]. Each atom is bonded to three neighboring atoms at 2.18 Å, with two of them being in plane with the layer at 99° from each other, and the third in between the layers at 103° (Fig. 1). However, the asymmetry in the BP crystal structure results in an anisotropic compressibility, offering great discrimination of its structure under high pressure. Consequently, BP undergoes two reversible structural transition, from the orthorhombic to rhombohedral phase at 5.5 GPa and room temperature followed by a volume change and displacement of the puckered structure. With higher pressure, at around 10 GPa, it changes from the rhombohedral to simple cubic phase, which remains stable with pressure up to 60 GPa. Both transitions are nearly independent of temperature during this process [8]. Monolayer BP consists of two atomic layers of phosphorus atoms arranged in a puckered honeycomb lattice that is described by the C_{2h} point group, as presented in Fig. 1c [9]. The orthogonal unit cell of monolayer BP exhibits two configurations along the x and y directions known as the armchair (AC) and zigzag (ZZ) directions, respectively (Fig. 1a,b). The interlayer bonding in monolayer BP is dominated by P atoms with sp^3 hybridization, which results in three orbitals bonding two atoms augmented by lone pairs connected to each atom [10].

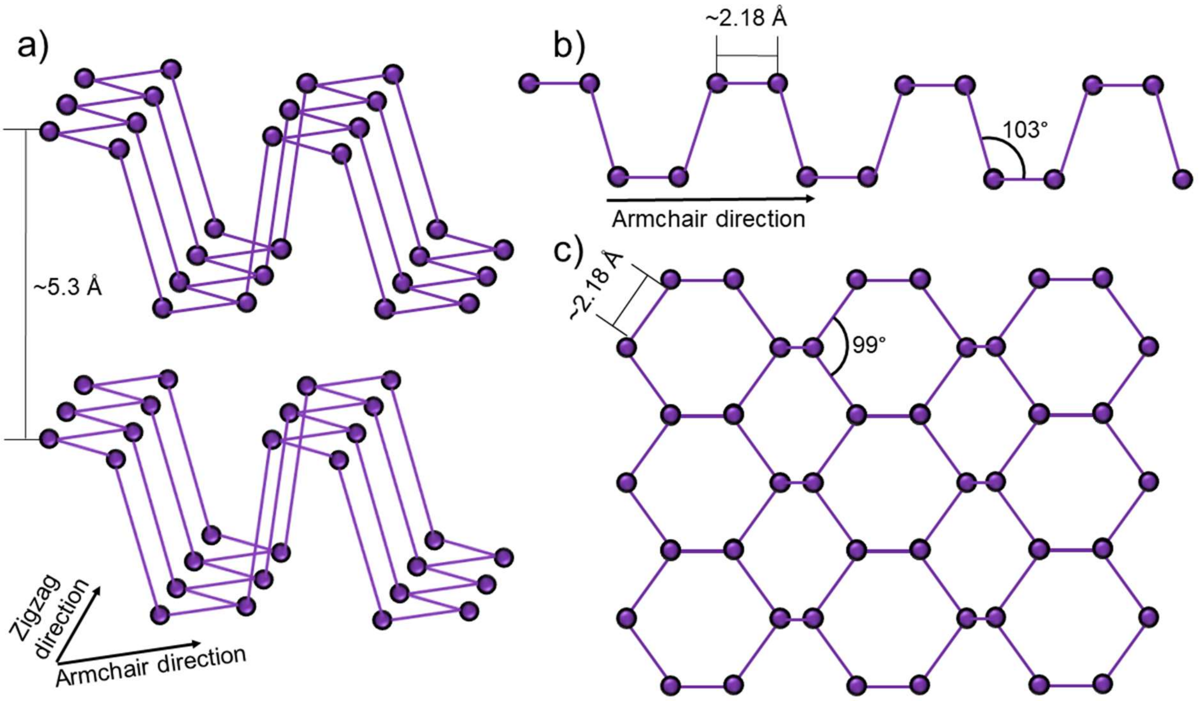

Figure 1. Black phosphorus structure: a) 3D representation b) lateral and c) top view.

1.2 Unique nature of black phosphorus structures

One of the most unique properties of black phosphorus is its thickness-scaling, tunable bandgap ranging from 0.3 eV for bulk BP to 1.5 eV for a monolayer (Fig. 2) [11]. The energy bandgap is a crucial characteristic of electronic materials and varies from 0, in graphene [12], to 5.8 eV, in hexagonal boron nitride [13]. Despite the wide variety of atomically thin, two-dimensional (2D) crystals, those with a bandgap range between 0.2 and 1 eV are noticeably missing (Fig. 3) [14]. Black phosphorus nanostructures not only correspond to the visible and infrared (IR) spectral range, but also possess additional tuning capabilities, which can further influence the electronic properties by implementing chemical functionalization, an external electric field or defect and strain engineering. These uncommon properties make BP especially attractive for optoelectronic applications, such as photodetection, photocatalysis and solar energy harvesting. Moreover, a BP monolayer can be altered between conducting and insulating states by surface or substitutional doping. It was demonstrated by Wang et al. that adatoms of carbon, boron, nitrogen, fluorine and oxygen can act as impurities, inducing mid-gap states that shift the BP monolayer character to metallic [15]. The high carrier mobility (1000 $cm^2/V\cdot s$)

and tunability as well as sufficiently flat morphology to confine electrons provide opportunities to implement thin BP nanostructures in biosensing applications [16,17].

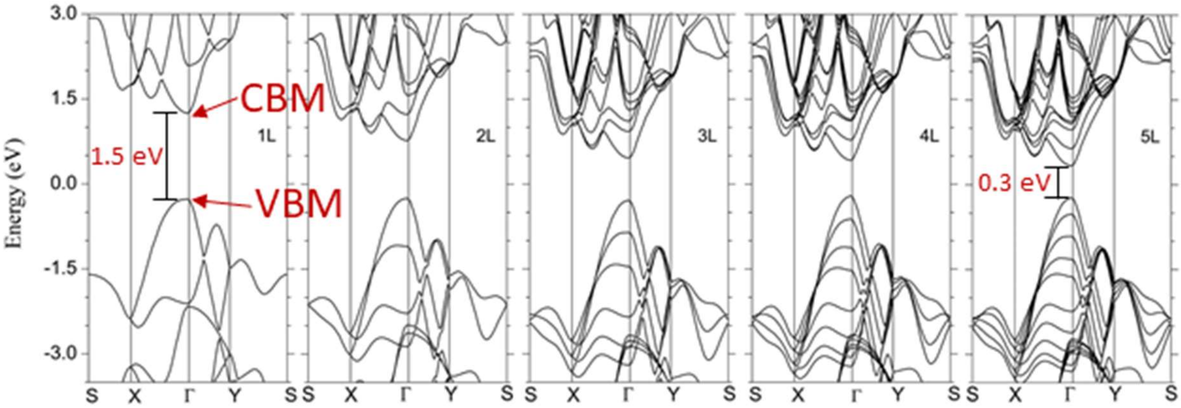

Figure 2. Band structures of BP nanostructures containing from 1 to 5 layers. Graph is reproduced from [18] under a Creative Commons license.

The unique structure of BP also influences its optical properties, with the optical responses exhibiting different behavior along the AC and ZZ directions. Moreover, the optical bandgap of BP also depends on the structure thickness varying from ~1.5 eV for a BP monolayer, known as phosphorene, down to 0.3 eV for bulk material [19]. In thin BP layers, the optical response is dominated by the excitonic effects, causing the energy of the optical bandgap to be lower than the energy of the corresponding electronic bandgap, as a result of the binding energy of excitons. In general, semiconductors, such as black phosphorus, can be divided into two groups depending on the character of their bandgap, which can be direct or indirect. In the case of the direct bandgap, the conduction band minimum (CBM) and the valance band maximum (VBM) are positioned at the same point of the Brillouin zone (BZ), as shown in Fig. 2. Whereas for the indirect bandgap, the analogous points are usually located in different valleys. As a consequence of the emitted photon carrying negligible momentum, the momentum conservation law is easily achieved only for a direct bandgap, where the carriers can recombine radiatively. On the other hand, the indirect bandgap recombination requires an additional mechanism involving scattering. Despite the high tunability of black phosphorus structures, the bandgap remains direct regardless of its thickness, and is located in the Γ valley of the BZ. Moreover, a high in-plane anisotropy of the optical properties of BP can be implemented for crystallographic axis determination [20].

1.3 Aim and hypotheses of this dissertation

The influence of various element on the properties of black phosphorus has been widely studied, however, there are few reports recognizing the capabilities of black phosphorus-arsenic nanostructures. The motivation for this thesis was to fabricate black phosphorus and black arsenic-phosphorus nanostructures and to investigate their structural, optical, electrochemical and photoelectrochemical properties, as well as demonstrating possible modifications of electrode materials, such as titania nanotubes or boron-doped diamond with BP and b-AsP coatings.

The aim of this thesis is to present possible fabrication methods of black phosphorus and black arsenic-phosphorus nanostructures, and to prove a higher air- and water-stability, as well as, an increase in electrochemical and photoelctrochemical performance after incorporating arsenic into black phosphorus structure, making it possible to utilize the material in specific optoelectronic, photovoltaic and sensing applications. Black phosphorus nanosheets, black phosphorus and black arsenic-phosphorus nanoribbons, as well as black phosphorus- and black arsenic-phosphorus-modified electrode materials such as a boron-doped nanodiamond layer and titanium dioxide nanotubes will be developed and investigated as part of the research.

The following research hypotheses were formulated in this dissertation:

Hypothesis I: Quantum confinement effects and the high surface-to-volume ratio of BP-based nanostructures increase the potential of this material for applications in electrical devices, sensors and as electrode materials.

Hypothesis II: Substitution of a portion of the phosphorus atoms with arsenic in BP-based structures minimizes its decomposition in water and air enabling electrochemical and electrical applications.

Hypothesis III: Surface modification of electrode materials such as boron-doped diamond and titania nanotubes with a b-AsP coating improves the photo-electrochemical and electrochemical properties of the newly formed heterostructures.

1.4 Structure of the thesis

In Chapter 1 of this dissertation, the fundamental parameters of black phosphorus are discussed. The development of BP fabrication methods, from the first BP synthesis to techniques implemented nowadays, is presented. The structure of black phosphorus is demonstrated and discussed as a source of its unique anisotropic properties. The scaling electronic properties of the BP structure are presented as a dependence between bandgap values and the thickness of the material. Lastly, the goals, motivation and hypotheses of this dissertation are presented.

Chapter 2 is an overview of various 2D layered materials, showing the differences and similarities between these 2D materials and black phosphorus. Firstly, graphene and boron nitride nanosheets are briefly discussed and compared to the electric and electronic properties of BP. Subsequently, two-dimensional transition metal dichalcogenides, which similarly to BP exhibit a tunable bandgap, are discussed. MXenes and oxide nanosheets are also compared in this chapter. The chemical stability and electronic properties of these materials make them efficient to utilize as electrode materials, however, due to the narrow bandgap of MXenes and the very wide bandgap of oxide nanosheets, they cannot be applied in optoelectronic and solar energy harvesting devices. Besides BP, other mono-elemental 2D materials are also presented in this chapter. The electronic properties of silicene, germanene and arsenene are briefly discussed and compared to phosphorene. The following parts of Chapter 2 consist of fabrication methods of 2D materials. The top-down and bottom-up approaches for low-dimensional BP structure are classified, discussed and presented. Then, zero-, one- and two-dimensional structures of black phosphorus are described. The structural and electronic properties of phosphorene nanosheets, nanoribbons and nanotubes are presented and discussed. Lastly, the degradation of BP in ambient conditions is discussed, with two strategies suggested to prevent BP from oxidizing. One of the presented methods includes changing the BP structure. Therefore, black arsenic-phosphorus structures are introduced, and changes in the structural and electronic properties in comparison to BP are discussed.

In Chapter 3, two electrode materials suitable for black phosphorus and black arsenic-phosphorus surface modification are presented. The first is titanium dioxide nanotubes. The structural and electrochemical properties, as well as fabrication methods of titania nanotubes are discussed. Various modification techniques of nanotubes are also described together with the possible impact that BP modification could have on the properties of the material. The second, boron-doped diamond electrodes, is also discussed in this chapter. The electrochemical properties of boron-doped diamond and its fabrication method are also described. It is shown that the properties of boron-doped diamond electrodes significantly depend on their surface morphology, boron concentration and surface modification, which suggests that BP and black arsenic-phosphorus modification of these structures can find application in wastewater treatment and biosensing devices.

Chapter 4 is an overview of the commonly used techniques utilized for the investigation of the photoelectrochemical and structural properties of BP and b-AsP structures. In this chapter, a three-electrode system used cyclic voltammetry and chronoamperometry is presented. Next, morphology imaging techniques of BP nanostructures are presented. Scanning and transmission electron microscopy, as well as atomic-force microscopy are shown to be vital tools in the investigation of BP nanostructures. Subsequently, the spectroscopic methods implemented for the investigation of the molecular structure of black phosphorus are described. Raman and UV-Vis spectroscopy are shown to be suitable for BP thickness and bandgap estimations, respectively.

Chapter 5 is a summary of the optical, electrochemical and structural properties of fabricated black phosphorus and black arsenic-phosphorus nanostructures. Firstly, the fabrication technique, a chemical vapor transport method, is described in detail. It is shown that the chemical vapor transport technique is suitable for the fabrication of both BP and b-AsP nanostructures, as well as surface modification of electrode materials with BP-based coatings. The following experiments are divided into two groups. First, BP structures and BP-modified electrodes are discussed. Then, changes in the electrochemical performance and optical properties between BP and b-AsP nanostructures are presented. In this chapter, liquid phase exfoliation is demonstrated to be a sufficient method for the fabrication of phosphorene flakes from bulk BP, but also for BP and b-AsP nanoribbon synthesis. The influence of three solvents used for liquid phase exfoliation on the surface morphology and stability of phosphorene flakes is discussed. Next, the fabrication method, surface morphology and optical properties of BP nanoribbons are demonstrated. Raman spectroscopy studies show the estimated thickness, structural orientation and crystallinity of BP nanoribbons. The following experiment demonstrates titania nanotubes modified with BP. The fabrication method, surface morphology, structural parameters and electrochemical performance are presented. High resolution transmission electrode microscopy and energy-dispersive X-ray spectroscopy reveal that after the modification process, phosphorus forms on both the inner and outer walls of the nanotubes. In the next experiment, b-AsP nanoribbons are investigated. The fabrication method, surface morphology, structural and optical properties, chemical composition and dimensions of the b-AsP nanoribbons are presented. In this study, the influence of the arsenic-to-phosphorus ratio on the final b-AsP microstructure is discussed. Raman studies of b-AsP structures can, similar to BP nanoribbons, be utilized for structural direction identification. Changes in the morphology and optical properties of b-AsP and BP nanoribbons are also presented. The following experiment describes the modification method of titania nanotubes with b-AsP. Structural, electrochemical and photoelectrochemical studies of b-AsP-modified nanotubes are presented in this section. The modified nanotubes exhibit high crystallinity and electrochemical stability, as well as a reversible redox behavior. The surface b-AsP modification of titania nanotubes is shown to have a positive impact on the photoelectrochemical performance of the material. Lastly, studies on other BP and b-AsP-modified electrode materials are presented. It is demonstrated that commercially available interdigitated array gold electrodes are suitable for growing BP and b-AsP structures. The needle-like BP and b-AsP structures exhibit an enormous surface-to-volume ratio and could be successfully utilized in sensing applications. In the last experiment presented in Chapter 5, boron-doped diamond modified with BP and b-AsP is presented. The fabrication and modification process of boron-doped diamond films is described. The surface morphology and structural properties of a b-AsP-modified boron-doped diamond electrode is demonstrated. Moreover, the electrochemical performance and the comparison of BP and b-AsP-modified boron-doped diamond is presented. The electrochemical studies reveal an increase in the electrochemical responses for black arsenic-phosphorus boron-doped diamond in comparison to black phosphorus modification.

Chapter 6 is the last chapter of this dissertation. It contains the summary of the theoretical part and experimental studies presented in this dissertation. Also, conclusions drawn from the experimental part are discussed and the directions for possible further research are demonstrated.

CHAPTER 2: Overview of 2D layered materials

2.1 Two-dimensional materials

Ever since graphene was fabricated, there has been growing interest in 2D nanomaterials and their properties. The continuous development of fabrication methods and possible applications of graphene has triggered active research into other layered materials, leading to the discovery of:

- boron nitride nanosheets (BNNSs),
- transition metal dichalcogenides (TMDCs),
- MXenes,
- oxide/hydroxide materials, and
- mono-elemental 2D semiconductors such as germanene, silicene and phosphorene.

2D nanomaterials are primarily studied for their electronic properties, hence the importance of their bandgap values. A comparison of the 2D materials family and their bandgap values is presented in Fig. 3. A better understanding of low-dimensional materials and their properties will make it possible to either implement them in various novel devices or combine them into heterostructures, creating more specialized technological solutions.

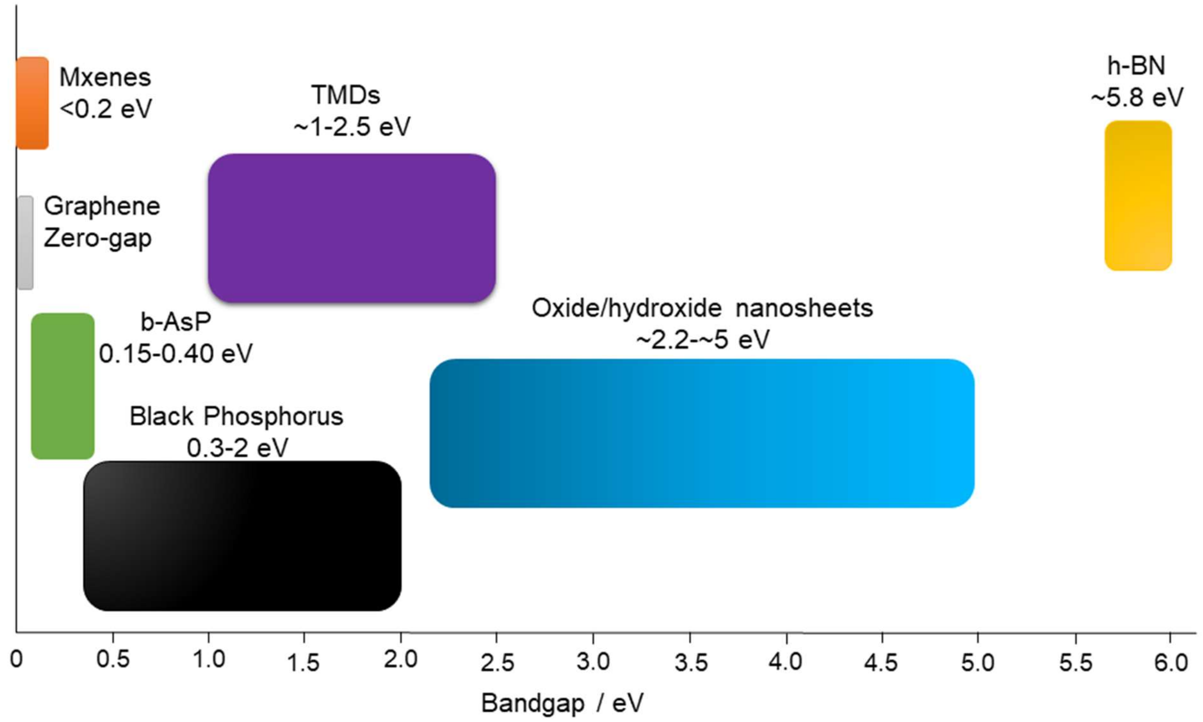

Figure 3. Comparison of electronic bandgap values of common 2D materials.

2.1.1 Graphene and boron nitride nanosheets

Graphene, as the first fabricated 2D nanomaterial, is still considered to be the most representative in the 2D materials family. Similar to diamond and fullerene, graphene is one of the allotropes of carbon. It consists of a single carbon atomic layer in a hexagonal arrangement. In graphene, each carbon atom bonds with three neighboring atoms with C-C sp^2 hybridized bonds of the length of 1.42 Å. These strong covalent bonds are the source of its various interesting properties such as high mechanical strength, Young's modulus of 1 TPa and intrinsic strength of 130 GPa, good thermal stability above 3000 W/m K and high carrier mobility at room temperature of 2.5 x 10^5 cm^2/ V s [21,22]. Graphene has many derivatives such as graphene oxide and reduced graphene oxide, and is accessible for functionalization. Porous graphene oxide can be utilized as an oxidative catalyst in the conversion of SO_2 to SO_3 [23,24] and as a photocatalyst for H_2 generation. On the other hand, nitrogen-containing graphene exhibits exceptional oxygen reduction activity, which can be used in fuel cells [25]. As a result of the well-known and yet undiscovered properties of graphene and its derivatives, graphene has become a compelling nanomaterial for a wide range of physical and chemical applications [21].

Due to its structural similarities with graphene, BNNS has become the second most researched 2D nanomaterial. Boron nitride (BN) is constructed from the same number of nitrogen and boron atoms. Like graphene, BN occurs in 4 allotropes with 4 different crystalline forms, among which hBN is the most stable under ambient conditions and is isostructural to graphite [26]. Moreover, h-BN and graphene share comparable mechanical and thermal properties, and both have good lubrication and an ultra-flat surface. Nonetheless, the main difference between graphene and h-BN is their bandgaps. Hexagonal boron nitride is an insulator with an extremely large bandgap (~5.8 eV), whereas graphene exhibits a metallic character as a zero-bandgap material. In comparison to BP, apart from clear differences in their electronic structures, few-layer BP conducts electrons at a similar rate to graphene [27].

2.1.2 Two-dimensional transition metal dichalcogenides

Two-Dimensional Transition Metal Dichalcogenides have gained a high amount of attention due to their semiconducting properties. Unlike graphene with metallic properties and h-BN, which is an insulator, TMDCs exhibit a tunable bandgap with various electronic structures. Compound such as MoS_2 have a controllable bandgap, which changes with thickness scaling, varying for monolayer and bulk structures or by combining them into heterostructures [28]. Moreover, the chemical and physical properties of TMDCs can be influenced by incorporating different chalcogens and transition metals. Furthermore, the structure of 2D TMDCs is also crucial with different properties for nanosheets [29] and nanoribbons [30]. The tunable bandgap and its possible transition from indirect to direct together with the immense liberty when designing their structure, put TMDCs at the top for potential application in a number of research areas such as photocatalysis as well as next-generation electronics and optoelectronics [31].

The main difference between few-layer TMDCs and few-layer BP lies in their electronic structure. Most TMDCs exhibit an indirect bandgap, whereas, as previously mentioned, BP has a direct bandgap regardless of its thickness, which is beneficial for optoelectronic applications [32]. Also, the carrier mobility of few-layer BP is higher than for most 2D materials, including TMDCs [33].

2.1.3 MXenes

MXenes are a relatively new class of 2D nanomaterials including nitrides, carbonitrides and transition metal carbides, which can be described with the general formula Mn þ1Xn. The most common approach to the fabrication of MXenes is by etching the A layer, being Al or Si, in the MAX phase of a hexagonal structure, with M being a transition metal such as Ta, Zr, Hf, Nb, Ti, V, Mo or Cr and N or C as X. The n layers of X in MXenes are covered by n þ1 layers of M and passivated by hydrogel, fluoride or oxygen groups, known as surface termination – T. The termination group is usually determined by the etching conditions, post-treatment processes and the M element. The properties of MXenes can be tuned by choosing an appropriate composition, due to their versatile chemistry [34]. The electronic properties can be tuned by switching the surface termination or metal atom; for example Ti_3C_2 can be modified by adding Mo, which changes the character of the material from metallic to semiconducting [35].

Since their discovery, MXenes have shown enormous potential in multidisciplinary application, due to their ease of functionalization, excellent conductivity, tunable surface chemistry and high hydrophilicity. In recent papers, MXenes have been studied for their possible applications in photocatalysis, adsorption and membrane separation. The sorption capabilities of MXese-based nanomaterials distinguish them from conventional carbon and graphene-based sorbents, making them an interesting substitute for the removal of toxic dyes and compounds or ions. MXenes and few-layer BP exhibit high electrical conductivity, as well as good ion storage capability. The electronic properties, chemical stability and structural configurations of MXenes and BP make them efficient to utilize as electrode materials in various types of batteries [36]

2.1.4 Oxide/hydroxide nanosheets

Most hydroxide and oxide nanosheets are fabricated by exfoliation of their 3D-layered counterparts. 2D structures of $LiLaTa_2O_7$, $LiCa_2Ta_3O_{10}$, $KTiNbO_5$, and KTi_2NbO_7 have been experimentally obtained by the intercalation method followed by mild ultrasonication. This method is highly controllable, with the lateral dimensions and number of layers being easily adjusted by choosing a different solvent or changing the sonication conditions. It can also be utilized for the fabrication of oxide and hydroxide nanosheets on a broad scale. The replacement of small with bulky ions during the intercalation process, such as tetrabutylammonium or nitrates, facilitates the exfoliation to individual nanosheets by weakening the electrostatic forces between the layers [37].

The variant composition of layered metal oxide and hydroxide nanosheets can be utilized in the development of various electronic and optical properties and used for diverse applications. However, they exhibit a large bandgap even comparable to monolayer BP, making them inefficient to implement in solar energy harvesting or optoelectronic devices [38].

2.1.5 Mono-elemental 2D materials

Despite its high mobility, the symmetrical structure of graphene is the main reason its bandgap is difficult to open, which results in graphene-based devices showing less tunable electrical conductivity. Thus, in recent years, a considerable amount of effort has been put into the fabrication of other mono-elemental 2D semiconductors. 2D materials were first isolated decades ago, however, due to an abundance of possible applications, they have regained significant interest. Structures based on black phosphorus, antimony, bismuth and arsenic have come into the spotlight. These mono-elemental materials are being heavily studied for their properties, which can differ significantly by thickness-scaling, doping and changes in their crystal structure. Moreover, few-layered structures of these elements can be easily fabricated using mechanical exfoliation of their bulk counterparts as well as via vapor deposition on surfaces. Mono-elemental 2D materials are chemically stable and due to their electronic properties, they can be implemented in energy-related and biosensing applications [39].

One of them, silicene, a 2D silicon material, has a tunable bandgap and can be applied for semiconducting devices such as field-effect transistors. Bulk silicon has strong Si-Si covalent bonding, which forbids silicene to be synthesized by various exfoliation techniques. Because of that, silicene is usually fabricated using the CVD method on Ag, ZeB_2, or Ir surfaces. Silicon and carbon are in the same group on the periodic table, however, unlike graphene, silicene has a buckled structure, formed by pseudo Jahn-Teller distortion breaking down the hexagonal ring or silicene. Moreover, silicene is highly reactive with its intrinsic spontaneity to form sp^3 bonds and extremely sensitive to both oxidation and reduction processes. It is, however, difficult to transfer silicene structures for device applications due to its poor stability even under vacuum [40]. The first reported silicene application is dated to 2015, when Tao et al. showed a field-effect transistor based on this material [41]. The reactive surface of silicene was protected by alumina deposition, since oxidation usually alters its bandgap, which was demonstrated by Du et al. who confirmed this phenomenon by Raman and STM measurement of silicene with various oxidation levels [42].

2D semiconductors based on germanium and tin have also been proposed. Germanene and stanene, respectively, can be obtained in an analogous manner to silicene. Stanene was fabricated on a BiTe and Au surface [43], while germanene was successfully synthesized in Ge_2Pt, Au and Pt [44]. Both materials have a buckled structure, which makes them eligible for the same applications as silicene.

As was mentioned, most 2D semiconductors feature a bandgap of either 2.0 eV or higher, or close to zero-gap, which may restrict their applications for solar energy harvesting and optoelectronic devices operating in the visible and UV spectral range. Arsenic crystalizes with a rhombohedral layered structure, which is its most stable allotropic form, usually named gray arsenic or β-As. The rhombohedral structure of arsenic is similar to the structure of BP in the sense of consisting of puckered, six-membered rings of atoms. However, unlike in BP, layers of gray arsenic are not bonded by true van der Waals forces, but rather the interactions of atomic orbitals between the individual layers. In bulk β-As, the 4p orbital overlap produces its semimetal character and good electron conductivity [45]. Moreover, Zhang et al. have reported that gray As retains its metallic character even if the structure is exfoliated to a three-layer structure. Further reduction of the arsenic structure down to a bi- and monolayer was calculated to shift its bandgap to 0.37 and 2.49 eV, respectively [46].

2.2 Fabrication methods of 2D materials

In this part, various techniques for 2D materials fabrication will be described. All of the low-dimensional materials fabrication methods can be classified into two possible approaches: top-down and bottom-up (Fig. 4). The top-down approach consists of breaking down bulk materials, while the bottom-up approach involves assembling low-dimensional materials from atoms and molecules. Most of the preparation methods are based on a top-down approach with exfoliation being the most commonly used. However, not all methods can be applied for every layered material. Some, such as unzipping of nanotubes is strictly limited to graphene fabrication [47].

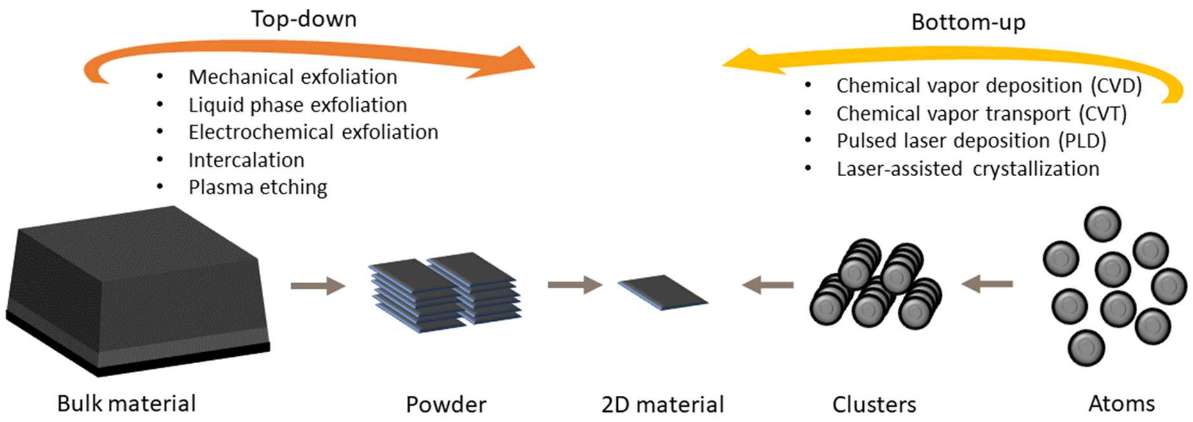

Figure 4. Fabrication methods of 2D materials.

As mentioned in Chapter 1, BP is a layered material which exhibits strong in-plane chemical bonds, but rather weak out-of-plane van der Walls (vdW) bonds. As a result, BP can be reduced to a single atomic layer in the vertical direction. This process is called exfoliation and is the most used technique for the fabrication of thin layers of BP. Phosphorene, a monolayer of black phosphorus, possesses significantly different optical, electrical and chemical properties from its bulk counterpart [48]. Exfoliation of BP can be carried out by applying various top-down and bottom-up techniques, the same as with other layered materials. The first successful attempt to fabricate a phosphorene monolayer was accomplished with mechanical exfoliation by applying blue Nitto tape and subsequently peeling off layers from a polydimethylsiloxane (PDMS) substrate [49].

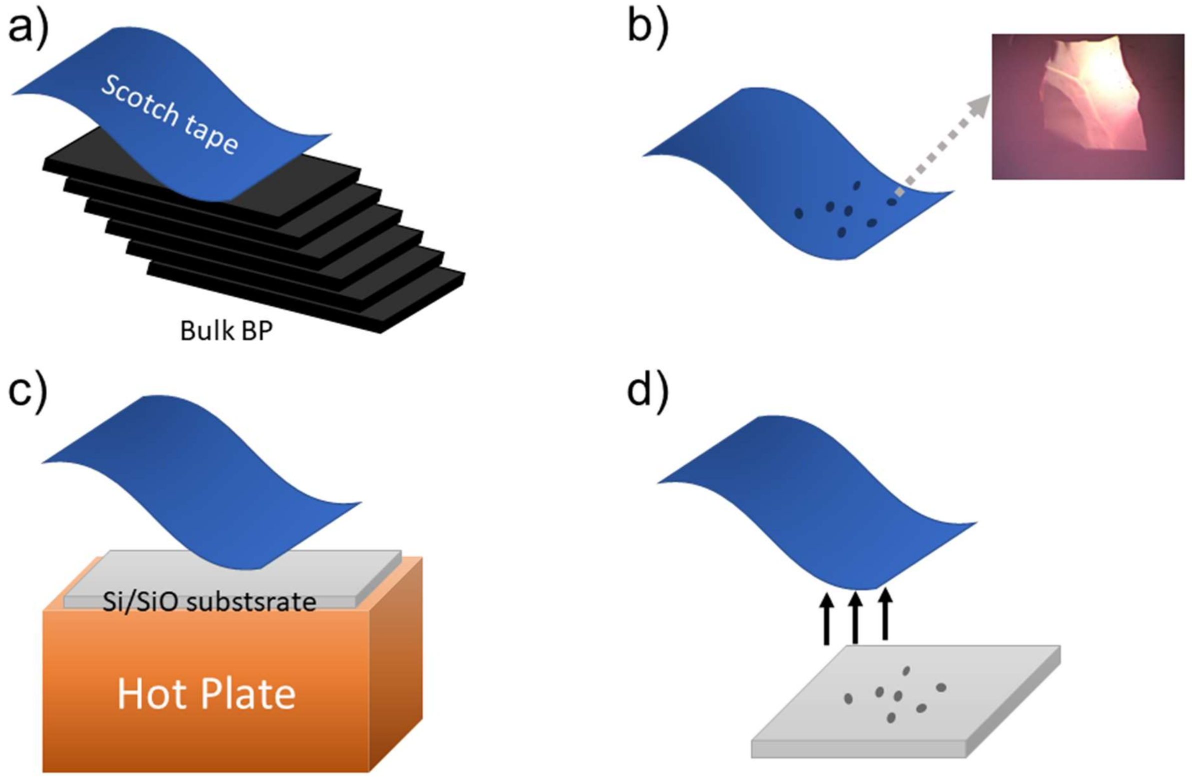

Figure 5. Mechanical exfoliation process of BP.

2.2.1 Mechanical exfoliation

The mechanical exfoliation technique was first used to isolate single-layer graphene in 2004. In this process, the ideal case is that a layered material can be peeled from the bulk crystal layer-by-layer. There are two routes for mechanical exfoliation, which are by normal and lateral forces. Using the normal force easily overcomes the van der Waals attraction and separates two layers of a layered material apart by utilizing micromechanical cleavage with Scotch tape (Fig. 5a), which sticks to tape surface (Fig. 5b) and can be transferred onto another substrate (Fig. 5c) by applying temperature high enough to overcome the adhesive properties of the scotch tape, leaving the exfoliated material on the surface of the chosen substrate (Fig. 5d). The ability of BP to self-lubricate in the lateral direction also makes it possible to exert a lateral force to induce relative motion between BP layers. The mechanical exfoliation can be used for the production of high-quality 2D materials of limited dimensions and is often the easiest step in conducting measurements of layered 2D nanostructures [50].

2.2.2 Liquid phase exfoliation

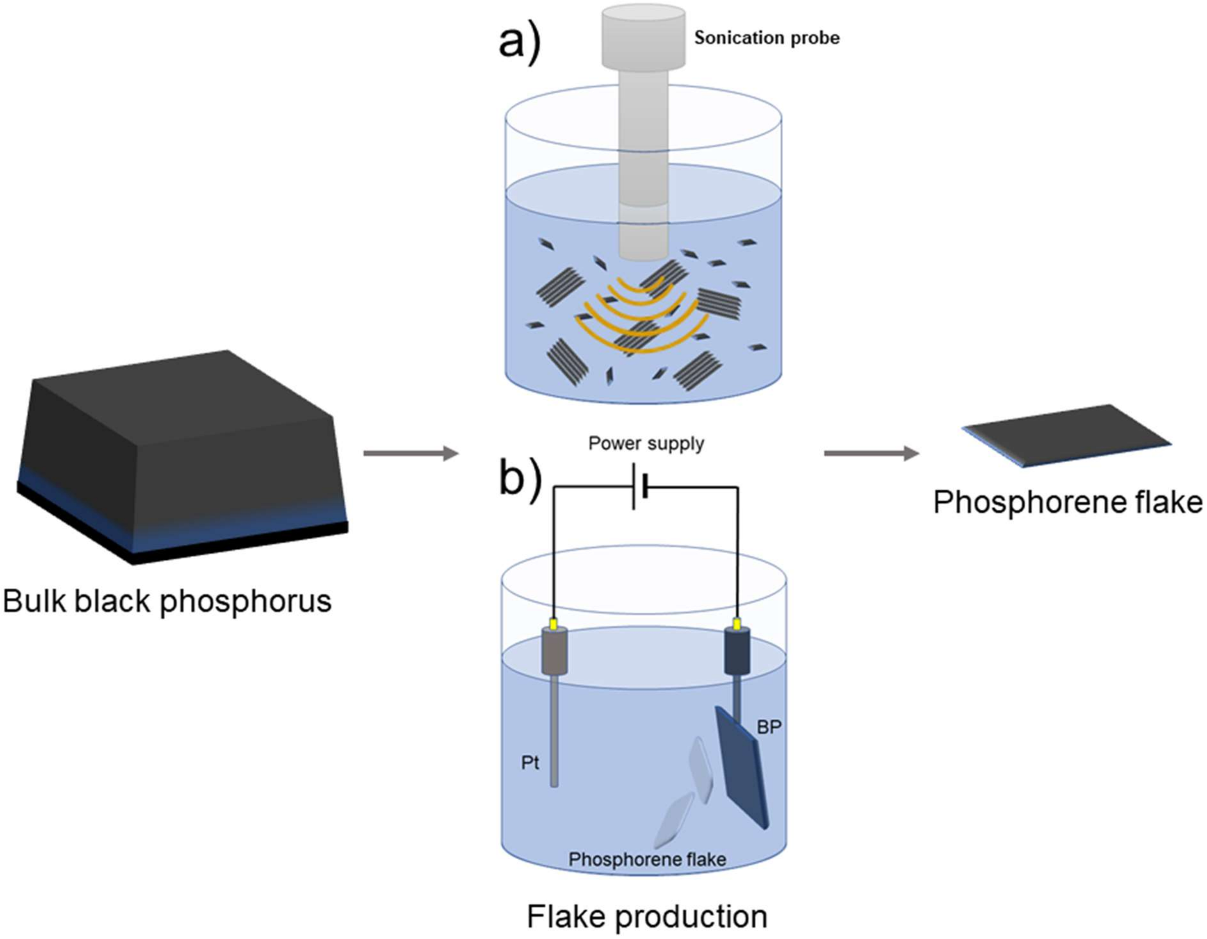

Figure 6. Phosphorene flake fabrication via a) liquid phase exfoliation and b) electrochemical exfoliation methods.

In layered materials, the van der Waals attractions among adjacent layers are weak enough to let them slide across each other in the direction perpendicular to the c-axis, but the attraction is strong enough to make complete exfoliation into individual layers challenging [51]. The first attempt by Brodie to produce single-layer graphene sheets by exfoliation dates as far back as 1859 [52]. Since then, many unsuccessful attempts have been made to produce solutions for the large-scale production of graphene. Successful exfoliation requires overcoming the van der Waals attractions between the adjacent layers. One of the most effective and straightforward methods to reduce the strength of the van der Waals attractions is liquid immersion, where the potential energy between adjacent layers is controlled by the dispersive London interactions, which in the presence of a solvent are significantly reduced with respect to vacuum [53].

In the past decades, it has been found that interfacial tension plays a key role when a solid surface is immersed in a liquid medium. If the interfacial tension between the solid and liquid is high, there is poor dispersibility of the solid in the liquid. In the case of BP flakes in solution, if the interfacial tension is high, the flakes tend to adhere to each other and the work of cohesion between them is high (i.e., the energy per unit area required to separate two flat surfaces from contact), hindering their dispersion in the liquid. Solvents with surface tension (viz. the property of the surface of a liquid that allows it to resist an external force, due to the cohesive nature of its molecules) $\gamma \sim 40$ mJ m^{-2} are the best solvents for the dispersion of flakes of BP and other layered materials, since they minimize the interfacial tension between the solvent and the surface of the material. Unfortunately, the majority of solvents with $\gamma \sim 40$ mJ m^{-2}, such as N-methyl-2-pyrrolidone (NMP – 40 mJ m^{-2}), N,N-dimethylformamide (DMF – 37.1 mJ m^{-2}), and ortho-dichlorobenzene (o-DCB – 37 mJ m^{-2}), have some disadvantages, e.g., NMP is an eye irritant and may be toxic to the reproductive organs, while DMF may have toxic effects on multiple organs. In general, sample preparation for electrical measurements requires complete removal of solvents, since the presence of remaining solvent can greatly impact the device performance. Thus, dispersion of layered materials in low boiling solvents is preferable. On the other hand, most low boiling solvents, e.g. water, ethanol, and chloroform, unsuitable for the purposes of direct exfoliation [54].

Brent et al. have adapted liquid exfoliation for the fabrication of few-layer phosphorene, applying ultrasonication to BP in NMP [55], as demonstrated in Fig. 6a. The liquid exfoliation route enables phosphorene fabrication on a decisively wider scale and, by adding NaOH during sonication, allows OH-adsorption on the surface which leads to the production of water-stable phosphorene flakes. Not long after that, Yasaei et al. investigated the influence of specific solvents on the exfoliation process, which revealed that an aprotic and polar solvent, such as DMF, can improve the stability of phosphorene dispersions [56]. Moreover, utilizing a mixture of aprotic solvents with ionic sulfonated polymers during liquid exfoliation can result in simultaneous separation and passivation of phosphorene layers and even cause morphological transformations into various nanostructures, as shown by Kumar et al. [57].

2.2.3 Electrochemical exfoliation

Since the successful fabrication of the first 2D materials, there has been growing interest in developing high yield and purity, scalable synthesis routes for industrial production and research purposes. One of the newer methods is electrochemical exfoliation, where a potential difference is applied between a layered bulk material anode/cathode in an electrolyte-containing medium. At first, the majority of the exfoliated, layered materials resulted in the fabrication of relatively thick flakes, however, using electrolytes containing H_2SO_4, they started to exhibit good exfoliation efficiency [58].

This method is a promising approach for the preparation of 2D materials. It is mostly implemented for graphene, but with growing interest, for semiconducting TMD materials. Most of the conducted experimental works with electrochemical exfoliation include anodic preparations, which cannot be applied for phosphorene or silicene because of the resulting oxidation of the structure. The cathodic methods, however, can be utilized for the fabrication of thin semiconducting layers of high quality, resulting in materials of good conductivity applicable for batteries and optical devices [59]. Later, Erande et al. utilized electrochemical exfoliation for the production of phosphorene nanosheets [60]. This method is conducted by immersing BP crystal, which served as a working electrode, in 0.5 M Na_2SO_4 with a platinum wire as the counter electrode and applying a positive bias voltage (Fig. 6b). The exfoliation process can be achieved by applying more than one technique at a time. Uniform BP flakes can be isolated by plasma-liquid exfoliation and application of a high 2 kV voltage at a BP electrode submersed in DMF [6].

2.2.4 Intercalation

The increasing success of graphene and boron nitride resulted in more interest in the electrical, optical and chemical properties of other 2D layered materials. The unique crystal structure of layered materials provides an opportunity to tune various properties by controlling their thickness or by introducing guest species at the van der Waals gap, which is known as intercalation [61]. This process is demonstrated in Fig. 7.

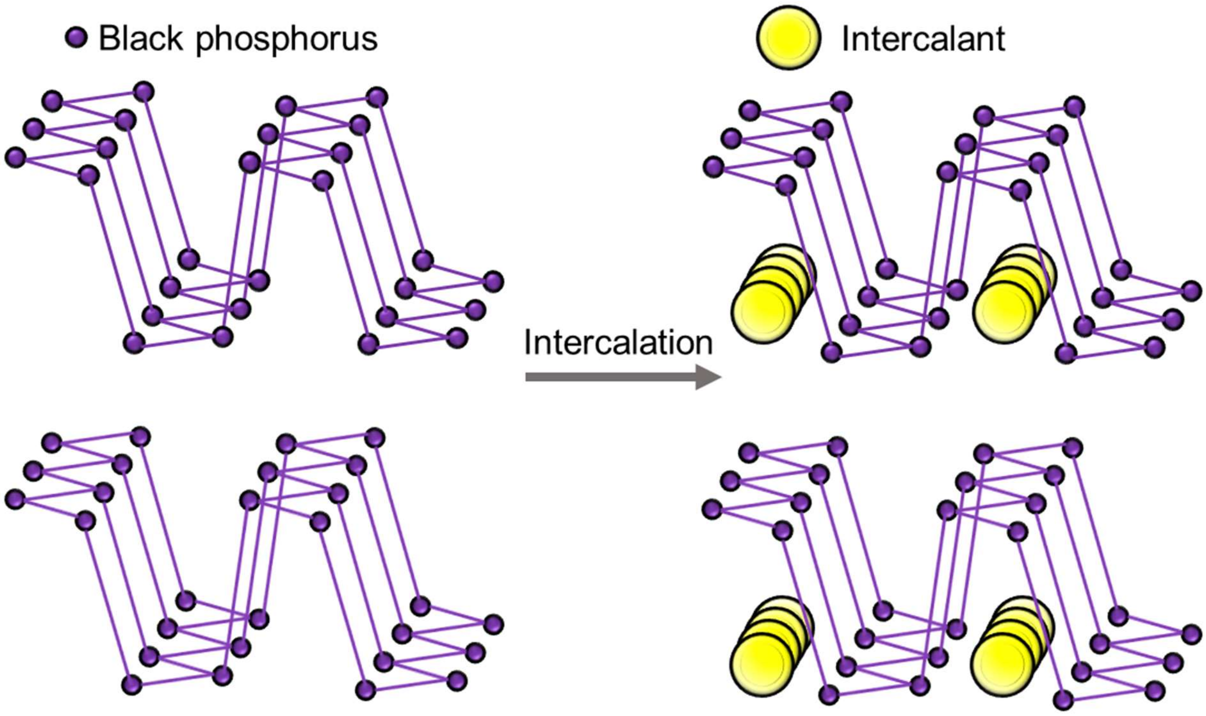

Figure 7. Schematic of intercalation process of black phosphorus.

Thus, novel possible applications of 2D layered materials in the fields of spintronics, optical sensors, catalysts and transistors have been investigated. It was reported that due to the intercalation of various functional building blocks, 2D metal chalcogenides can develop novel plasmonic and photonic applications. The plasmonic responses of noble metals have also been successfully tuned through the intercalation process, influencing the shape of chemically synthesized nanostructures [62].

The intercalation method can also be utilized for pristine few-layer black phosphorus fabrication as well as BP intercalation compounds, usually with alkali metals. The first attempt at BP intercalation dates back to 1987, when Nishii et al. presented the effects of iodine intercalation on a bulk black phosphorus structure and its electrical properties [63]. This method regained a lot of attention when BP nanostructures were first fabricated. Huang et al. predicted that the semiconducting character of bilayer phosphorene can be shifted to superconducting by Li intercalation [64]. This method was also utilized for the first experimental fabrication of phosphorene nanoribbons [65].

2.2.5 Plasma etching

Plasma treatment is a widely implemented and effective technology for multiple purposes such as the cleaning, etching, and surface modification of low-dimensional materials. Moreover, plasma systems can be utilized for generating a mixture of reactive species to treat a number of surfaces, such as semiconductors, metals, glasses, and plastics. Plasma systems engage one or more process gases, e.g., O_2, which after converting to a gas plasma contains a collection of reactive species, such as ions, electrons, or photons. In the treatment chamber, these species interact with the surface of the treated sample, as presented in Fig. 8, resulting in chemical reactions including the breakdown of molecules, electron transfer, polymerization, and the removal and addition of functional groups [66].

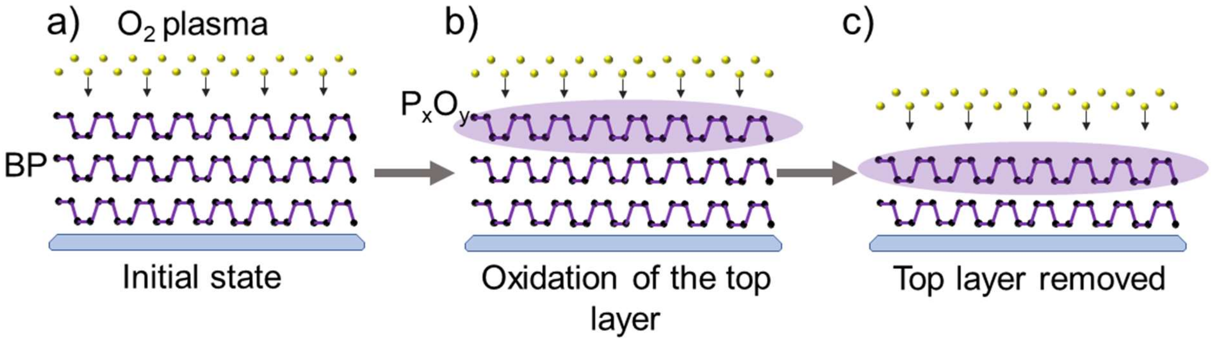

Figure 8. Plasma etching process of black phosphorus layers.

Plasma etching is one of the most common applications of plasma treatment. During this process, a generated gas plasma bombards the sample, breaking down the materials at the surface to smaller volatile molecules that are removed by the vacuum system. With plasma treatment, it is possible to etch off the entire top layer of the material, as well as parts of the surface by using various masks. However, the active species of gas plasma interact exclusively with the top layers of the sample and may not be effective when treating bulk materials. Moreover, the type of the occurring reactions can be controlled by the selection of a specific gas, resulting in various outcomes of the treatment [67].

The plasma-assisted fabrication method was proposed by Lu et al., who synthesized a BP monolayer by transferring a piece of few-layer phosphorene onto a Si/SiO_2 substrate and thinning using argon plasma [68]. This method, unlike liquid exfoliation, is not capable of producing a large number of phosphorene samples at once, nevertheless it is precise and fast and can be applied for the fabrication of high-area phosphorene nanosheets of specific dimensions. The approach demonstrated by Lu et al.

was later expanded to bigger-scale production of phosphorene flakes thinner than 10 nm by Huang et al. [69].

Apart from the top-down methods, BP thin layers can be produced by a number of bottom-up approaches, such as laser-assisted crystallization from red phosphorus [70], chemical vapor deposition, and chemical vapor transport.

2.2.6 Chemical vapor deposition

The first MoS_2 nanosheet grown using the CVD method was reported in 2012, where S vapor was used to sulfurize a Mo metal film, creating an atomic-layered MoS_s on a SiO_2/Si substrate [71]. Chemical vapor deposition can be utilized to fabricate a range of 2D materials, including TMDCs, MXenes, and mono-elemental films [72].

For example, a MoO_3 precursor powder and suitable growth substrate were placed in the upstream and downstream zones, respectively, in a quartz tube furnace [73]. The MoO_3 was partially reduced to form MoO_{3-x} species by the S vapor. Then, it was subsequently conveyed downstream for further reaction with the S vapor to produce monolayer MoS_2 with high crystal quality. Generally, the latter route preferably forms monolayer TMDCs. In contrast to the fabrication of sulfides, H_2 may be required to facilitate the reduction of Se species during selenization due to the latter's difficult reduction. Zhao et al. synthesized metallic VSe_2 and $TaSe_2$ nanosheets under a mixed Ar/H_2 flow [74]. However, restricted by the high melting points of some metal and metal oxide precursors, these precursors are difficult to vaporize and react with gaseous chalcogen precursors in the CVD process, posing a challenging task to grow the corresponding TMDCs. Han et al. proposed that salt could decrease the melting point of the reactants and facilitate the formation of intermediate products (metal oxychlorides), increase the overall reaction rate, and promote growth [75].

CVD-grown 2D MXenes possesses high crystal quality, crystal orientation, large domain size, and thickness uniformity and continuity, which could be selectively engineered for energy electrocatalysis applications. Because of rapid progress, a variety of 2D TMD nanosheets have been successfully synthesized [76]. Chemical vapor deposition is also used for red phosphorus thin layer and polycrystalline nanodiamond fabrication [77].

The CVD technique was introduced as a BP thin film fabrication route by Li et al. in 2015 [78]. In this method, a thin red phosphorus film is deposited on a substrate from red phosphorus powder via chemical vapor deposition and subsequently converted into black phosphorus by applying pressure of at least 8 GPa in an anvil cell. In the following year, Smith et al. further developed this method, showing that red phosphorus films can be obtained from both RP powder and BP pieces [79]. The theoretical calculations revealed that BP thin layers can be directly synthesized via CVD using a selected metal substrate, such as Sn, Ag, or Au [80]. It is, however, yet to be experimentally achieved.

2.2.7 Chemical vapor transport

A number or crystal growth processes proceed from the gas phase. One of the possible routes for the fabrication of bulk crystal as well as regular structured layers is using the chemical vapor transport method. This technique includes a heterogeneous reaction showing that a condensed phase, usually a solid, can be volatilized in the presence of a transport agent and a gaseous reactant, which can be deposited in different forms, such as bulk crystals, as presented in Fig. 9. The process will take place if the external conditions of the chemical equilibrium vary for crystallization and volatilization. Usually, various temperatures are used for volatilization and for crystallization (Fig. 9) [81].

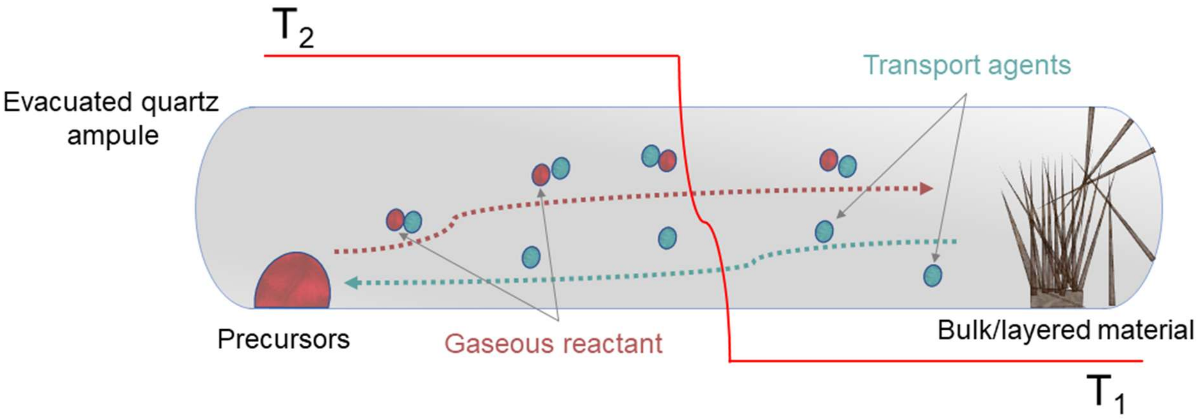

Figure 9. Chemical vapor transport route toward the fabrication of bulk/layered materials.

The chemical transport of elements has been widely studied for many metals and semi-metals. As for the typical non-metals, such as phosphorus, its volatility does not need to be increased in the sense of a CVT reaction due to its high vapor pressure. Generally, those elements that feature high vapor pressures can be efficiently transferred into the gas phase via sublimation or distillation. There are, however, metals with a low melting temperature, such as tin, lead and gallium, which can only be obtained in liquid form at most. Thus, the chemical vapor transport technique can only be implemented for elements with low vapor pressures and high melting temperatures [82].

The gas phase reactions are performed with hot-wire and CVD processes or by using closed reaction vessels, which is the main route for bulk black phosphorus synthesis. All of the above are based on the same thermodynamic principles and together create an enormous range of possible synthesis alternatives with many elements that can be crystallized with chemical transport reactions [83].

It is also possible to affect the initial bulk BP production process by changing crucial parameters of the CVT method leading to the fabrication of various BP microstructures. These structures can also be subjected to the exfoliation process resulting in the fabrication of a handful of exciting BP nanostructures such as nanoribbons, nanobelts, and nanowires. The CVT method is widely discussed in the experimental section as it is the primary technique implemented for the black phosphorus and black arsenic-phosphorus nanostructures presented in this dissertation.

2.3 Low-dimensional structures of black phosphorus

Downsizing BP structures to a low-dimensional regime cause changes in the electronic structure, inducing quantum confinement effects by broadening the bandgap and modifications in the density of states (DOS). While two-dimensional structures exhibit a quantum confinement in one direction, reducing in the other directions can lead to one-dimensional (1D) and zero-dimensional (0D) structures. Moreover, low-dimensional materials exhibit properties unobtainable for three-dimensional structures (3D), including an enormous surface-to-volume ratio, prominent edges, and a large number of active sites. These properties and the ability to effectively engineer the bandgap make BP nanostructures a competitive alternative to apply in novel technologies such as photovoltaics, electrochemical energy conversion and storage, catalysis, and sensing applications [84,85].

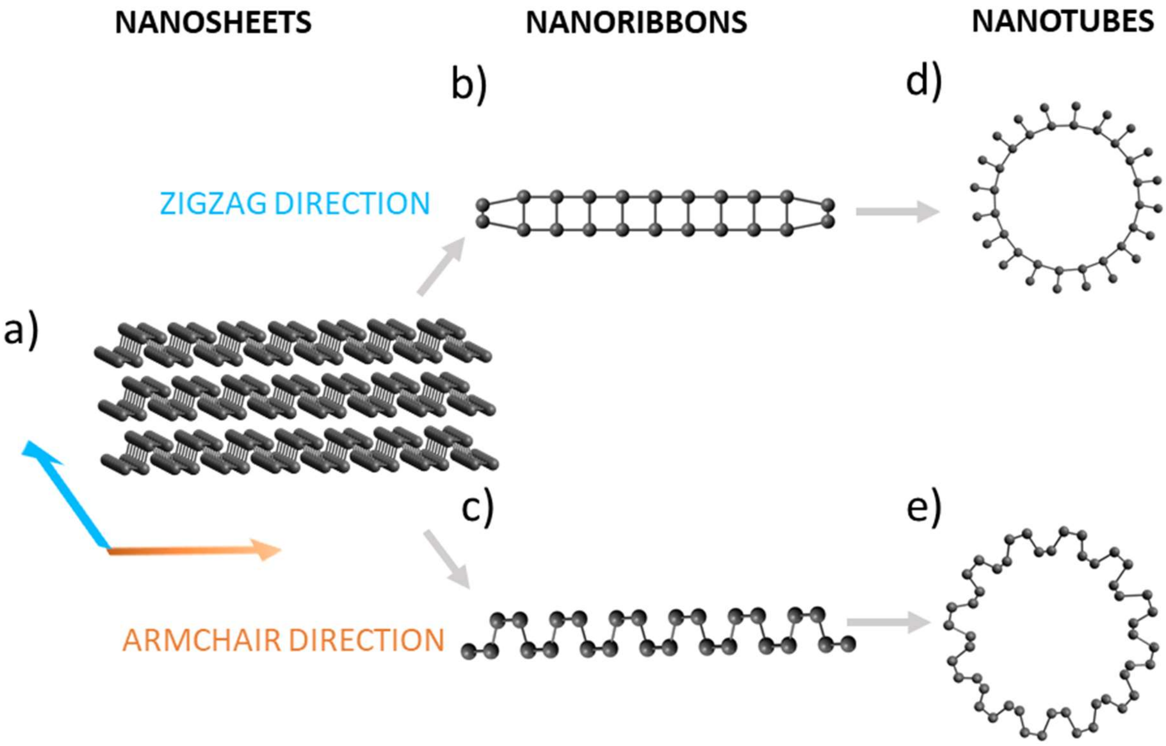

Figure 10. Summary of black phosphorus nanostructures: a) BP nanosheets marked with zigzag and armchair directions, BP zigzag b) and armchair c) nanoribbon and BP zigzag d) and armchair e) nanotubes.

2.3.1 Black phosphorus nanosheets

A phosphorene nanosheet was the first BP 2D nanostructure fabricated with mechanical exfoliation by separating mono- and few-layer phosphorene from bulk BP crystal. Its structure consists of phosphorus atoms located on two atomic planes with a distance between them of around 1.90 Å. As in bulk BP, there are two bond types (in- and out-of-plane) and two distinguishable non-equivalent directions, which, as previously mentioned, are the armchair and zigzag directions (Fig. 10a). Due to its structure, phosphorene is a highly anisotropic material, including a band structure and optical properties such as polarization-dependent light absorption [86]. Moreover, the mechanical properties are also highly anisotropic, which was theoretically demonstrated by Zhang et al. [87].

According to calculations, monolayer phosphorene can withstand stress of 8 GPa in the AC direction and up to 18 GPa in the ZZ direction, which distinct phosphorene from WS_2 and MoS_2, with their band structure being extremely sensitive to strain. Furthermore, pristine BP nanosheets display a direct bandgap with a calculated value of 0.869 eV, which is responsible for its semiconducting nature. The direct bandgap also sets phosphorene apart from other 2D semiconductors, such as MoS_2 and WS_2, which exhibit an indirect-to-direct bandgap on transition to a monolayer [19].

Even though mechanical exfoliation is a high-quality approach for the fabrication of BP nanosheets, it is limited to laboratory scale investigations. This method is more difficult to implement at a larger scale due to phosphorene's instability in ambient conditions. There are some "bottom-up" techniques for the production of BP nanosheets, among which are chemical vapor deposition [79], and pulsed laser deposition (PLD) [88], both of which are time-consuming, costly and intrinsically unscalable. As a result, liquid methods, either by ultrasonication or electrochemical exfoliation, might be a possible solution to the wide-scale fabrication of BP nanosheets [89].

2.3.2 Black phosphorus nanoribbons

BP nanoribbons, an example of a 1D phosphorene nanostructure, are constructed from a single atomic layer and in order to exhibit quantum confinement in two directions, need to be less than 100 nm in width. Recent theoretical calculations reveal that BP nanoribbons surpass the mechanical and optical properties of monolayer phosphorene [90,91]. Furthermore, changes in the nanoribbon dimensions affect the properties, such as carrier mobility and electronic structure, which allows BP nanoribbons to be implemented in an even wider range of applications. Even though there are a number of possible fabrication methods of graphene nanoribbons, only few are applicable to phosphorene, leaving the production of phosphorene nanoribbons a great challenge [92].

The vital electronic and mechanical properties of a BP nanoribbon depend mostly on its edge structure [93]. AC nanoribbons (Fig. 10c) can be fabricated by separating a BP monolayer parallel to the AC direction, while ZZ nanoribbons (Fig. 10b) can be produced by cutting a BP monolayer perpendicular to the AC direction. One of the few possible fabrication methods of ZZ nanoribbons is ultrasonication in a polar solvent, such as Nafion or DMF [94]. Excluding the outermost edge atoms, ZZ nanoribbons can be responsive to Peierls distortion and unit cell doubling, they undergo little structural relaxation, however [91]. Recent theoretical studies predict pristine ZZ nanoribbons to exhibit a metallic character, which does not change with the nanoribbon width. However, pristine AC nanoribbons are semiconducting with an indirect bandgap, which decreases with the width scaling [95]. The accessible bandgap engineering and significant strain effect of AC nanoribbons makes it easily applicable in field effect transistors (FET), strain sensors, and infrared photodetectors.

The morphology and structural properties of black phosphorus and black arsenic-phosphorus nanoribbons are more broadly described in Chapter 5 of this dissertation. A novel fabrication method, as well as the structural and optical properties of the nanoribbons, can be found in that section.

2.3.3 Black phosphorus nanotubes

Single-walled phosphorene nanotubes (SW-PNTs) and double-walled phosphorene nanotubes (DW-PNTs) have only been investigated with computational methods, without successful experimental attempts yet to be reported. The theoretical studies predict the production of SW-PNTs by rolling up a phosphorene layer along the AC or ZZ directions forming AC SW-PNTs (Fig. 10e) and ZZ SW-PNT, respectively (Fig. 10d). The calculations have demonstrated that for diameters of 1.2–1.9 Å, the optimized unit-cell length in the axial direction equals 3.30 Å for SW-PNTs. While changes in the diameter of AC PNTs have no effect on the unit-cell length, it increases from 4.13 Å to 4.48 Å with a diameter change from 12 Å to 17 Å in the case of ZZ PNTs [96].

Both zigzag and armchair SW-PNTs exhibit a semiconducting character, however, ZZ nanotubes can transition into a more semi-metallic behavior [95]. According to theoretical studies by Yu et al., AC PNTs have a thin direct bandgap, which can be further reduced by compressive strain [96]. Moreover, the compressive strain can also induce higher carrier mobility, as well as an increase in the PNT diameter. Considering the enormous difference in electron and hole mobility, AC PNTs might be recognized as an n-type semiconductor finding application in optoelectronic devices and metal–oxide–semiconductor field-effect transistors (MOSFETs).

DW-PNTs have been reported to be more stable than SW-PNTs and according to Fernández-Escamilla et al. might be more stable than phosphorene nanosheets [97]. Computational studies reveal that to fabricate the most stable DW-PNTs, the distance between the internal and external nanotube needs to be similar to the distance of between the atomic layers in bulk BP. Furthermore, the bandgap of DW-PNT has been reported to be smaller than those of SW-PNTs, and could be influenced by tuning the diameter of both the external and internal nanotube.

2.3.4 Degradation-prevention methods toward air-stable black phosphorus-based nanostructures – black arsenic-phosphorus

Despite the many extraordinary properties of BP nanostructures, there is a significant problem that humpers their application, which is the rapid degradation of BP in ambient conditions. The reason for such a susceptibility to degradation has been connected to the unstable bonding structures of free lone pairs of phosphorus atoms. The oxidation has also been related to a synergetic effect of water and oxygen, where water reacts with the surface oxide creating oxygen dissociations, which drives the oxygen. The BP degradation has been reported to depend mostly on the light intensity and oxygen concentration [98].

Thus, two kinds of strategies have been developed to overcome or slow the degradation process of BP. One of the viable solutions is to create a barrier on the surface of the BP, including organic and inorganic coatings. Gamage et al. proposed a coating fabricated with hybrid metal-organic chemical vapor deposition (MOCVD) of 2 nm boron nitride followed by 3 nm of Al_2O_3 growth by atomic layer deposition (ALD), which according to the theoretical studies, can protect BP from oxidation for over 6 months (Fig. 11). Nevertheless, improving the stability of BP with coatings undoubtedly negates its applications for surface interactions, such as sensors and catalysis [99].

The second strategy includes functionalization of BP layers with surfactants, metal ions, and small molecules, resulting in a thin protective layer through various interactions. This method preserves the physical and chemical properties of the BP, however, the low binding energy between the BP and the protective layer reduces its reliability for electrical and electrochemical measurements.

Metal-organic framework (MOF) coatings have been reported to be efficient in overcoming BP’s limitations. MOFs consist of metal ions connected by organic ligands and can interact with lone pair electrons on the surface of phosphorus atoms, reducing the surface electron density, and as a result weakening the reactivity of the BP with water and oxygen. Moreover, MOFs are thermally and chemically stable and exhibit high porosity, large pore volume and open architectures, offering compelling permeability to liquid and gas molecules [100].

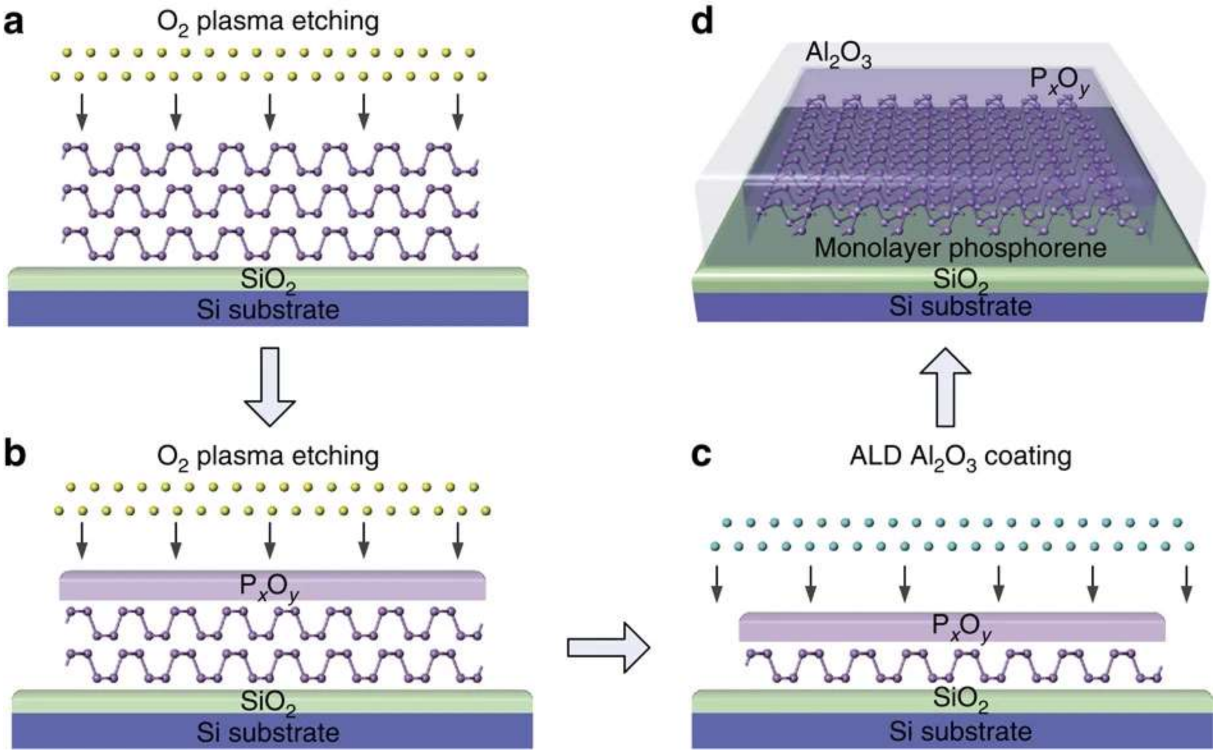

Figure 11. Process of BP monolayer coating with an Al_2O_3 protective layer by ALD. Reproduced from [99] under the terms of the Creative Commons CC BY license.

Recently, BP nanosheets have been investigated for their possible applications in biomedical nanotechnology due to their outstanding photothermal and chemotherapeutic properties. To adapt BP nanosheets for biomedical application, organic coatings would be required. Mo et al. reported a successful BP nanosheet surface modification process with a corona protein, which regulated macrophages in a positive way, making the further development of a biologically neutral and stable coating vital for BP applications in medicine [101].

As previously mentioned, the degradation of BP occurs easily in an air environment or aqueous solution, which leads to weakening of the material's photoelectric properties [102,103]. Despite many attempts, it is still challenging to obtain high stability while maintaining the desired optical and electrical properties of BP. Nevertheless, a different approach based on introducing substitute non-metallic atoms of arsenic into the BP structure has been proposed to improve BP's stability. The compound fabricated in this way is known as black arsenic-phosphorus (b-AsP), a derivative of 2D phosphide expressed by the formula b-As_xP_{1-x}. Introducing various amounts of As atoms into the BP structure influences the properties, improves the stability and vastly narrows the bandgap of the material, ranging from 0.15 to 0.35 eV [104].

Bulk b-AsP can be produced by implementing the CVT method; the same method as described for the fabrication of pristine BP crystals. In this method, gray arsenic and red phosphorus are used as starting materials. Moreover, their initial ratio will define the concentration of As and P atoms in the fabricated structure, allowing easy access to bandgap engineering. Layered b-AsP materials, similarly to BP, have a puckered honeycomb lattice, and the unit cell volume increases with the arsenic content. Thus, b-AsP materials exhibit strong in-plane covalent bonds and weaker van der Walls interactions, enabling exfoliation down to a single atomic layer. Furthermore, b-AsP structures exhibit similar electronic, structural, and optical properties to BP, including a tunable bandgap, high anisotropy, and high carrier mobility. In addition, b-AsP can form heterojunctions with other 2D materials, creating new possibilities for electronic devices. Moreover, low-dimensional b-AsP structures can find applications in mid-wave IR photoconductors due to their capability of fast photoresponse and low dark noise [105]. The research on b-AsP nanostructures is still in an early state, with most papers focused on bulk or mechanically exfoliated structures.

2.4 Future of two-dimensional materials

Several 2D materials, such as graphene, h-BN, TDMCs, MXenes, metal oxides, and mono-elemental 2D materials have been introduced in this chapter. Their fundamental electronic properties, commonly utilized fabrication methods, and comparison to BP structures have been discussed. BP nanostructures and their possible applications have been presented. Moreover, degradation-prevention methods of BP thin layers, including incorporating arsenic into the BP structure, have been proposed.

2D materials exhibit extraordinary optical, electronic, and chemical properties. However, the application of these materials in novel devices may require utilizing them as surface modifications of electrode materials or combining them into heterostructures. Novel heterostructures composed of single 2D crystals, can find applications in light-emitting and resonant tunneling diodes, and as tunneling transistors. In this dissertation, BP and b-AsP have been utilized as surface modifications of electrode materials to enhance their electrochemical performance and sensing possibilities. The electrode materials chosen for BP and b-AsP modification were commercially available Au electrodes and CVD-fabricated polycrystalline boron-doped diamond (BDD) films. The modification of titania nanotubes (TiO_2 NTs) with BP and b-AsP, and the increase in the electrochemical performance and solar-energy harvesting have also been reported.

CHAPTER 3: Characteristics of TiO_2 nanotubes and boron-doped diamond electrode materials

3.1 Characteristic and synthesis of electrode materials

In recent years, there has been increasing interest in the field of phosphorene and BP application. The chemical stability, and strong anisotropic optical and physical properties of BP and phosphorene are fundaments for the implementation of BP in biomedical applications [106], as well as phosphorene-based electronics and photonics devices [107,108]. Moreover, several scientific groups have studied the electrochemical performance of phosphorene-based electrode materials and their efficiency in electrochemical energy storage devices [109–111]. With the rapid increase in novel energy harvesting and storage devices, such as micro-solar cells [112], micro-supercapacitors [113], and K-ion batteries [114], there is a strong motivation for combining BP and b-AsP with various electrode materials. Herein, titanium dioxide nanotubes and boron-doped diamond electrodes and their fundamental properties, fabrication methods and modification possibilities are described in this chapter. Moreover, in the experimental section of this dissertation, the morphology, structural properties and electrochemical performance of TiO_2 NTs and BDD thin films modified with BP and b-AsP are presented.

3.2 Titanium dioxide nanotubes

Titanium dioxide is one of the most widely used materials for research in the field of photovoltaics and photocatalysis. The significant interest in this material results from its non-toxic nature and cheap synthesis, as well as high stability during exposure to solar radiation. However, there are some practical limitations to its use. Titanium dioxide is an n-type semiconductor with a bandgap of approximately 3.2 eV. The high value of the energy gap means that it is active only in the ultraviolet radiation range, which is only 5% of the entire spectrum of solar radiation [115].

There are three TiO_2 allotropic varieties occurring in the natural environment. They are anatase, rutile with a tetragonal structure, and brookite with an orthorhombic structure. Rutile has the highest thermodynamic stability, showing a lower total free energy than the other two phases. Anatase, in turn, is characterized by a higher mobility of carriers compared to rutile and a higher value of the energy gap. For rutile, its value is 3 eV, while the energy gap for anatase is 3.2 eV. In solar cells based on TiO_2, anatase is the more preferred allotrope due to its higher conductivity band boundary energy and lower electron-hole pair recombination ratio compared to the other phases [116].

The chemical and physical properties of TiO_2 depend not only on the energetic or electronic structure of the material, but also on its size, shape, and surface properties. The ordered morphology and the possibility of manipulating the geometric dimensions resulted in a significant increase in interest in one-dimensional nanostructures such as nanotubes, nanorods, and nanofibers [117]. As previously mentioned, nanotubes are vertically oriented, elongated cylindrical one-dimensional structures. The walls of titanium dioxide nanotubes are always multilayered, and the number of layers varies from 2 to 10. The nanotubes usually have a constant diameter, but with some fabrication methods, their inner diameter decreases with their length. Due to the nanometric size of titanium dioxide structures, there is a significant advantage in the surface to volume of atoms ratio in the material [118]. However, TiO_2 NTs have a high recombination rate of the generated electron-hole pairs. In recent years, TiO_2 nanotubes have gained a lot of attention thanks to their structure and properties, which has resulted is a lot of possible applications for this material, such as dye solar cells [119], supercapacitors [120], lithium-ion batteries [121], biomedical materials, and biosensors [122].

3.2.1 Fabrication methods of TiO_2 nanotubes

The methods of producing titanium dioxide nanotubes can be divided into two categories: without and with the use of a matrix. In the case of the methods requiring the use of a matrix, the resulting material accurately reflects the form of the matrix used. This group includes, among others, atomic layer deposition and chemical vapor deposition. Using these methods, it is possible to create regular structures at the nano and micro scale with the possibility of precise control of the morphology of the produced material. One of the main disadvantages is the need to remove the matrix after the synthesis is completed, which significantly increases the cost of the process. Another limitation to the wider use of the matrix methods is the need to maintain the high cleanliness of the surface of the materials to ensure adequate adhesion between the substrate and the resulting material [118].

In the case of nanotubes, however, the most common method of synthesis is without the use of a matrix. The main synthesis methods for this group are hydrothermal synthesis and electrochemical oxidation. In the hydrothermal method, a key role in the formation of the nanotubes is played by single- and multilayer titanate nanostructures, which, by bending and coiling, create a structure with nanotube geometry. One possibility of bending the titanate layers is the force that acts on a single surface layer that is exposed to an asymmetrical chemical environment. On both sides of the analyzed layer, different concentrations of H^+ and Na^+ ions were introduced, which resulted in an increase in the surface energy and, consequently, a bending of the structure. In hydrothermal methods, changing parameters such as the temperature, type of solution, synthesis time, or type of substrate allows for precise control of the morphology of the produced nanostructures [123].

For most applications, it is crucial to work with a continuous and regular layer of nanotubes, and because of that, the electrochemical oxidation method, also known as anodization, is preferred. Anodization is a process to create a compact or porous oxide layer on the surface of a metal. When a sufficiently high voltage is applied to the considered metal M, it is oxidized to M^{2+}, which forms the metal oxide $MO_{z/2}$ or is dissolved in the electrolyte. The opposite reaction is the reduction of protons, which results in the production of hydrogen at the cathode [124]. The fabrication process of TiO_2 NTs is controlled by the balance between the processes of anodic oxide production and the chemical dissolution of oxides in fluoride compounds. At the same time, the $[TiF_6]^{2-}$ ions form from the titanium cations transported by the electric field. The further growth of the oxide is controlled by an electric field and takes place through the transport of O^{2-} and Ti^{4+} ions deep into the forming oxide layer. The voltage applied to the system is constant, while the field inside the oxide decreases systematically due to its increasing thickness, which inhibits the ongoing process [125].

The process of the formation of titanium dioxide nanotubes takes place in two stages. Firstly, a surface oxide layer is created, which reduces the current flowing. In the next step, local activation of the surface occurs, and the pores begin to form in an unorganized manner. Due to the growth of the pores, the specific surface area and the current value increase. After some time, the pores begin to form larger structures, growing deeper into the oxide layer, and thus they begin to compete for the flowing current. If appropriate parameters are selected, the pores will grow at an equal speed, creating an ordered structure of nanotubes. To obtain highly ordered nanotubes, double anodization is used. In the first stage, the anodization process is conducted to produce nanotubes. The resulting nanotubes are then removed, for example, by etching in oxalic acid or sonication. After removing the nanotubes, regular pores form on the surface of the titanium, on which highly ordered nanotubes will form during the next anodization [126].

3.2.2 Modification of TiO_2 nanotubes

TiO_2 nanotubes are considered to be one of the most effective and environmentally friendly photocatalysts used for the photodegradation of a wide range of pollutants. However, they have significant drawbacks that substantially limit their prevalence in technological applications. The main one is that the bandgap of TiO_2 NTs (3.87 eV) is wider than that of TiO_2 particles (3.2 eV). The increase in the bandgap value is attributed to the quantization of electronic states in TiO_2 NTs and downsizing from 3D to low dimensional structures [127]. To improve the efficiency of TiO_2 NTs in visible light, many methods of modification are used, the main task of which is to induce a bathochromic shift, i.e., reducing the energy gap or introducing additional energy bands within the bandgap. Such a change shifts the absorption maximum toward longer wavelengths, from the ultraviolet to the visible light range in the case of titanium dioxide nanotubes [128]. Another possibility to improve the performance of TiO_2 NTs is to reduce the recombination rate of the carriers, which will result in a significant increase in photoactivity. The methods of modification of TiO_2 nanotubes can be divided into several groups depending on the type of material that affects the structure of the nanotubes.

3.2.3 Metal and metal ion doping

Another possibility of modification of TiO_2 nanotubes is doping with metals and metal ions. Surface modification with precious metals such as gold, silver, and platinum are of particular interest. It is related to the phenomenon of localized surface plasmon resonance, which significantly increases the photocatalytic properties of the nanotubes. The surface modification of TiO_2 nanotubes with noble metals or bimetallic nanoparticles also makes the excitation of photogenerated electrons easier when exposed to visible light. In addition to gold and platinum, doping with transition metals is also used. Metal admixtures can reduce the rate of carrier recombination, and increase the photoelectric efficiency [129].

One of the examples of metal doping is doping with niobium, which increases the concentration of electric charge carriers. Doping with manganese, chromium and iron increases the activity of TiO_2 nanotubes in visible light. Moreover, Fe^{3+} has been considered to be the most favorable metal ion dopant due to the similarity of its radius to Ti^{4+} and its low bandgap of 2.6 eV. When Fe^{3+} ions substitute Ti^{4+} sites, a new energy level within the bandgap of TiO_2 is introduced, enabling visible light absorption [130]. This can be attributed to the charge transfer transition between the conduction band of TiO_2 and the d-state electron of the dopant or from the balance band to the newly introduced energy level [131].

3.2.4 Coupled semiconductor composites

Another way to increase the efficiency of titanium dioxide nanotubes is to create a p-n junction between TiO_2 and a p-type semiconductor such as NiO, Cu_2O, or ZrO_2 [132–134]. The aim of this procedure is to reduce the recombination rate produced by photogeneration of hole-electron pairs. The generation of a p-n junction will create an internal electric field. In the initial state, the induced electric field will cause the region of the p-type semiconductor to be negatively charged, while the region of TiO_2 will be positively charged. When illuminating the junction, electron-hole pairs are generated, which are then separated by the generated internal electric field. The result will be a flow of holes toward the region of the negatively charged junction, and a flow of electrons toward the region of the positive sign. The processes of recombination of carriers are limited, which increases the photocatalytic activity of the system [135].

The modifications of TiO_2 nanotubes with narrow band semiconducting nanomaterials such as CdS and PbS quantum dots can vastly improve the photocatalytic activity. The charge separation due to the photogenerated electron transfer from CdS to TiO_2 significantly restrain the charge recombination [136]. Thus, the CdS-TiO_2 NT composite can be applied to reinforce the photocatalytic degradation of organic pollutants [137]. Moreover, the incorporation of wide bandgap energy semiconductors, such as ZnO, into TiO_2 nanotubes could contain the charge recombination and increase the photocatalytic activity [138].

3.2.5 Non-metal doping

Another possibility of modifying TiO_2 nanotubes is doping them with non-metals such as carbon, sulfur, phosphorus, or nitrogen. It is believed that the most effective of the above-mentioned is doping with nitrogen, due to the similar atomic radius compared to oxygen atoms, and the mixing of the p-energy states of the nitrogen with the p-states of the oxygen, which consequently leads to a narrowing of the energy gap. There are many methods of doping TiO_2 nanotubes with non-metals. Such techniques include sol-gel methods, ion implementation, CVD, CVT, and electrochemical doping [139].

Besides nitrogen, BP has also attracted a considerable amount of attention for highly efficient photo/electrocatalysts because of its layer-dependent bandgap and broad sunlight absorption from the UV to NIR regions. Zheng et al. demonstrated that constructing a heterojunction photoelectrode with BPQDs and TiO_2 nanotubes can significantly increase the photoconversion efficiency of titania nanotubes and can be utilized for photoelectrochemical water splitting [140]. Song et al. showed that doping a BP-TiO_2 composite with sulfur can lead to an air-stable, high-performance anode material for sodium-ion storage [141].

Due to its high chemical stability, BP is often considered to be a valuable material in biological systems [142]. Moreover, BP exhibits extraordinary electronic properties, which may have a positive influence on optoelectronic and solar-energy harvesting devices [143]. On the other hand, TiO_2 NTs are still struggling to unlock their full potential in that area, hampering their application on a broad, commercial scale. Combining these two materials might bring novel solutions and the commercialization of both TiO_2 NTs and BP nanomaterials. The main limitation is still the stability of BP thin layers, which may be overcome by utilizing b-AsP as a surface modification, which may result in air- and chemically stable TiO_2 NTs-b-AsP systems.

3.3 Boron-doped diamond

Diamond is a well-known material for its hardness and electrochemical stability. Different types of diamond electrodes have been investigated for many years, including: polycrystalline, microcrystalline, and nanocrystalline [144]. Specific interest is directed toward BDD films fabricated by CVD on various substrates. In diamond, each carbon atom is covalently boned to its neighbor, forming an extraordinarily strong crystalline structure. The BDD structure exhibits a tetrahedral lattice with some carbon atoms substituted with boron, which changes the electronic properties of the material from an insulating to a semiconducting character [145].

Boron-doped diamond electrodes exhibit remarkable chemical stability, a wide potential window, low surface adsorption, and high O_2 evolution overpotential and low background currents, making them suitable for use as anodes for electrochemical oxidation reactions [146], including wastewater treatment [147]. Modified BDD electrodes have found application in treating domestic sewage, nuclear wastewater, and dye wastewater from printing ventures [148]. Despite the excellent wastewater processing potential, fabrication of BDD electrodes is complex and expensive, blocking their application on a broader scale. However, surface modifications of BDD might further increase their electrochemical oxidation efficiency, making them more profitable to utilize in wastewater treatment devices. Modification strategies of BDD with metallic and non-metallic nanoparticles, biofunctionalization of diamond films, and using non-metal coatings, such as BP, can provide opportunities for nanoscale analytical devices to be anticipated in the near future.

3.3.1 Fabrication method of boron-doped diamond

BDD electrodes are usually synthesized using CVD techniques using methene (CH_4), hydrogen (H_2), and diborane (B_2H_6) as precursors [149]. The BDD electrodes presented in the experimental section, used as substrates for BP and b-AsP surface modification, were synthesized in a microwave plasma-assisted chemical vapor deposition (MW PA CVD) system. Highly doped, single-crystal p-type Si substrates were seeded by sonication in a nanodiamond suspension for 30 minutes and subsequently dried under a nitrogen stream and placed in the CVD system. The temperature was kept at 700 °C during the deposition process. The plasma was ignited by microwave radiation, with its power kept at 1300 W throughout the synthesis. The molar ratio of the CH_4-H_2 gas mixture was kept at 1% with a total gas flow rate of 300 sccm, and the process pressure was kept at 50 Torr. To fabricate a boron-doped diamond electrode, B_2H_6 was introduced to the gas mixture in an amount to match 10,000 B parts per million (ppm) C atoms.

3.3.2 Electrochemical performance of boron-doped diamond

BDD electrodes have been widely investigated in the literature for their electrocatalytic performance. The studies have shown that the electrochemical performance of BDD films can be improved by turning the CVD conditions, such as deposition time and temperature, or methane-to-hydrogen ratio, influencing the boron surface concentration, specific surface area and its roughness, and the sp^3/sp^2 ratio [150]. A higher boron doping concertation of BDD films can increase the surface carrier transfer efficiency, while a larger specific surface area could increase the electrochemical oxidation efficiency and reduce the interfacial reaction by creating more active sites at the BDD surface. The surface roughness has been reported to correlate to the wastewater treatment and degradation efficiency of BDD films [151]. Thus, changes in the BDD microstructure can effectively increase the electrochemical performance of diamond-based electrodes. Nonetheless, one of the most important parameters is the sp^3/sp^2 ratio, which reveals the quality of the fabricated BDD film. Higher values of the sp^3/sp^2 ratio correspond to stronger chemical stability, a wider electrochemical potential window, and higher O_2 evolution overpotential [152]. There are only a few studies on the effects of BP modification of BDD in the literature, one of which is described in the experimental section.

CHAPTER 4: Techniques for photoelectrochemical, optical and structural studies of black phosphorus-based materials

4.1 Cyclic voltammetry

Cyclic Voltammetry is one of the potentiodynamic electrochemical techniques based on measuring the electric current versus applied potential. The potential changes cause the electrode to undergo oxidation and reduction processes. The key parameters measured in cyclic voltammetry are the values of the cathode and anode current peak, as well as the anode and cathode peak potentials [153]. This method is frequently used as it provides qualitative and quantitative information about electrochemical reactions. In particular, it makes it possible to assess the influence of the electrolyte on the redox processes, as well as the location of the oxidation and reduction peak potentials. Currently, the most common measurements are carried out in the three-electrode system with a working electrode (WE), reference electrode (RE), and counter electrode (CE) (Fig. 12).

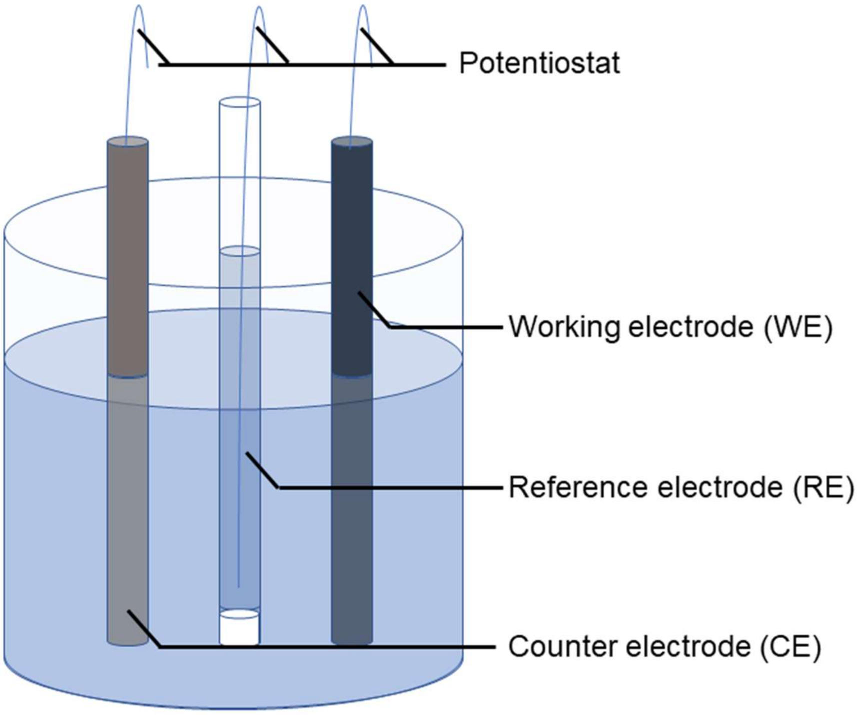

Figure 12. Three-electrode system used in electrochemical studies.

Cyclic voltammetry can be utilized in studies of the electrochemical properties of bulk and layered black phosphorus. Wang et al. reported that black phosphorus shows a significant oxidation peak at ~0.6 V (vs AgCl) corresponding to the oxidation of P^0 to P^{5+}, possibly forming H_3PO_4 as an end product [154]. They also studied the influence of pH of given solution on black phosphorus oxidation revealing that the highest currents occur at low pH, which indicates that the electrochemistry of black phosphorus can be utilized in various biosensing applications. Niu et al. reported that a black phosphorus nanosheet-modified glassy carbon electrode can be used for sensitive voltammetric detection of rutin [155]. Black phosphorus has also been implemented for hemoglobin immobilization. Li et al. showed that a black phosphorus and poly(3,4-ethylenedioxythiophene)-poly(styrenesulfonate)

(PEDOT:PSS) composite exhibits electrochemical stability and extraordinary electrocatalytic performance, and can be used for detection with satisfactory results [156].

4.2 Chronoamperometry

Chronoamperometric measurement consists in registering changes in the intensity of the current flowing through the electrode in relation to changes in the electrode potential over time. The measurement starts at a fixed potential where no electrochemical processes occur on the electrode. Then, the potential is abruptly changed to the value at which the oxidation or reduction process occurs. The potential is held for as long as the current signal is recorded. For a procedure involving successive changes of potential, the value of the potential in the first step is converted to the reverse potential, i.e. oxidation or reduction to the process occurring in the first phase of the test [157].

With regard to black phosphorus, chronoamperometry is often employed to investigate the durability of black phosphorus-based electrodes and their biosensing possibilities. Xu et al. adopted the rapid surface oxidation of phosphorene to achieve efficient heteroatom doping. Highly crystalline nitrogen-doped phosphorene has shown excellent electrocatalytic performance as a non-metallic catalyst for nitrogen (N_2) to ammonia (NH_3) conversion, and revealed good stability during chronoamperometric nitrogen reduction reactions [158]. Mayorga-Martinez et al. applied chronoamperometric measurements to evaluate the performance of phosphorene as a sensing material, presenting its ability toward H_2O_2 sensing [159].

4.3 Morphology imaging by electron microscopy

4.3.1 Scanning electron microscopy

Scanning electron microscopy (SEM) is a technique commonly used for imaging the surface of nanostructured materials. The imaging is conducted using a microscope in which an electron beam in a column is accelerated between an anode and a cathode. The presence of high vacuum in the column allows the electrons to travel efficiently. The electron beam interacts with the sample, colliding with its atoms, which results in a loss of kinetic energy, total absorption of the beam, reflection from or penetration through the sample under analysis. The main factors influencing the ratio of the number of reflected, penetrated, and absorbed electrons are the thickness of the sample and its chemical composition. Each of the generated radiation beams comes from different depths of the tested sample. The increase in the energy of the incident electrons is related to the depth of the area from which the signals are emitted. As a result of the interaction of the primary beam with the sample, several types of electrons are emitted, which can be used for not only imaging but also chemical composition analysis in the case of X-ray energy dispersive spectroscopy [160].

In practice, SEM is a vital tool for most experimental works. Since most low-dimensional materials cannot be seen under an optical microscope, SEM imaging is often a first step in confirming the successful fabrication of BP nanostructures. Moreover, the properties of nanostructures, including black phosphorus quantum dots [161], nanoribbons [162], and nanosheets [163], strongly depend on their dimensions. Therefore, information about the size of the fabricated structures is crucial for sample analysis. The limitations of scanning electron microscopy come from its setup, and thickness measurements without cross-section imaging are mostly inconclusive.

4.3.2 Transmission electron microscopy

In a conventional transmission electron microscope (TEM), a sample is irradiated with an electron beam of uniform current density. Electrons are generated in the electron gun by Schottky, thermionic, or field emission. The intensity distribution of the electrons behind the specimen is imaged with three to eight lenses onto a fluorescent screen. To obtain the desired resolution, the specimen needs to be thin, usually of the order of 5–100 nm for 100 keV electrons, varying for elemental composition and density of the object. For crystalline samples, a Bragg-reflected beam on-axis (dark field), or a primary beam (bright field) creates a diffraction contrast, which is important for crystal defects imaging. Moreover, if Bragg-diffracted electrons also cross the aperture, projections of atomic rows can be obtained by crystal-structure imaging. The conventional TEM is typically applied for the imaging of very thin nanostructures, and is usually utilized as an initial step for scanning transmission electron microscopy (STEM) and high-resolution transmission electron microscopy (HRTEM), which provide information about the chemical composition and crystallinity of the specimen [164].

4.3.3 Scanning transmission electron microscopy

The further development in the transmission technique resulted in the possibility to fabricate electron probes with a diameter of 0.2–10 nm. The nanometer-sized electron probes find application in analytical electron microscopy and enable the microscope to work in scanning transmission mode, allowing imaging of thicker samples and recording of backscattered and secondary electrons. The STEM can be utilized for investigating the chemical composition of fabricated nanostructures, revealing a sum spectrum of the elements detected in the considered region of the specimen [165]. This method is, however, inconclusive when investigating structures of specific allotropes, such as black phosphorus, but can be useful for heterostructures or composite nanomaterials.

4.3.4 High-resolution transmission electron microscopy

High-resolution transmission electron microscopy (HRTEM) is based on the wave-optical theory of imaging, which can be presented as a two-stage Fourier transform. The diffraction pattern is formed in the focal plane of the objective lens. TEM can provide a high resolution as a result of elastic scattering, which is a highly localized interaction process in the region occupied by the Coulomb potential of an atomic nucleus. In the case of inelastically scattered electrons, the angular distribution is concentrated. The diffraction pattern of the specimen is formed in the focal plane of the objective lens. Transmission electron microscopy can provide high resolution because elastic scattering is an interaction process that is highly localized to the region occupied by the screened Coulomb potential of an atomic nucleus. The angular distribution of inelastically scattered electrons is concentrated in narrower scattering angles, and even though the inelastically scattered electrons can pass through the objective diaphragm in bright-field mode, they do not contribute to high-resolution imaging [166].

Most information about the orientation and crystal structure is provided by the electron-diffraction pattern. Obtaining the selected area diffraction (SEAD) pattern in considered to be the most desired feature of TEM for the investigation of defects in a crystalline material or the crystal lattice itself. The SEAD patterns can be used to measure and calculate the averaged dimensions of the unit cell of black phosphorus nanostructures and their cell axial ratio, which for the fabrication of black phosphorus nanostructures would confirm the formation of the desired allotrope [167]. Qiao et al. utilized HRTEM to establish the lattice spacing between BP nanosheets, and to identify the (020) and (100) crystallographic planes of the BP structure [168].

4.4 Atomic-force microscopy

The atomic-force microscope (AFM) works by scanning a probe over the surface of a specimen to generate a map of the topography or height of the surface. Its key components are a force-sensing cantilever mounted on a scanner, which allows three-dimensional positioning with subatomic precision. An AFM operates differently from other microscopes, the image is not obtained by focusing a light or electron beam onto a surface, resulting in a two-dimensional image, as in optical or electron microscopes. With an AFM, it is possible to obtain a height profile of the sample, which is difficult when using SEM or TEM. Moreover, an AFM can operate in ambient conditions, making it possible to monitor biological reactions in real-time. It is also possible to implement ultra-high vacuum at cryogenic temperature and measure the hopping of individual atoms from a surface. An AFM has various additional modes that allow it to measure the electrical and thermal properties of a specimen, but its low cost and efficiency makes AFM an excellent imaging technique [169].

Since its invention in the 1980s, the AFM has been commonly implemented for studying various nanomaterials. The thickness, length and width and also topography of thin layers can be measured using this imaging technique. Watts et al. presented the accurate measurement of the heights and length of phosphorene nanoribbons using high-speed atomic-force microscopy (HS-AFM). This technique made it possible to count and estimate the distribution and the number of layers of the BP ribbon, as well as their width [65].

4.5 Investigation of molecular structures by spectroscopic methods

4.5.1 Raman spectroscopy

Raman spectroscopy is a technique that measures the inelastic scattering of photons, the so-called Raman scattering. Raman spectroscopy makes it possible to determine the structure and properties of particles that do not show rotational spectra nor oscillatory transitions. According to the quantum theory of radiation, as photons collide with atoms, an atom may gain energy, this is referred to as Stokes scattering, or lose energy – anti-Stokes scattering. During the collision of a photon with an atom, the system changes its initial energy state and the energy of the photon changes according to the principle of conservation of energy. Raman spectroscopy measures the intensity of the scattered wave as a function of frequency shift. Due to the fact that in Raman spectroscopy the electric field of the electromagnetic wave induces a dipole with which it then interacts, changing the frequency does not affect the position of the Raman signal, only its intensity[170].

According to theoretical studies, there are twelve possible lattice vibrational modes in black phosphorus, six of which are active. Yet only three modes can be detected by the incident laser, perpendicular to the black phosphorus plane. These modes are defined as A_g^1 (out of plane), B_{2g} and A_g^2 (in plane), which have been predicted to be found at 363 cm^{-1}, 442 cm^{-1}, and 470 cm^{-1}, respectively [171]. However, the peak positions in black phosphorus will shift with thickness scaling. Jasinski et al. reported the frequency difference of B_{2g} and A_g^2 modes to vary between 31 and 27.7 cm^{-1} for monolayer and bulk crystal, respectively [172]. Moreover, computational studies have demonstrated a strong dependence between the width and the vibrational properties of phosphorene nanoribbons. The A_g^2 modes shift toward higher wavenumbers and for narrow ribbons additional peaks, connected to the edge effects [173]. The Raman modes' positions and their shifts can not only define the crystalline structure of the material of black phosphorus, but also somewhat predict and compere the number of layers for structures with similar dimensions [174].

4.5.2 UV-Vis spectroscopy

Absorption spectroscopy involves the study of matter using electromagnetic radiation. In other words, the process of absorbing an electromagnetic wave by a substance. The absorption of ultraviolet (UV)-visible (Vis) radiation causes the excitation of an electron from the ground state to a state of higher energy. The Uv and vis ranges overlap each other with Uv ranging from 200 to 400 nm and vis from 400 to 800 nm and both are accessible in commercial spectrometers. In electronic spectroscopy, the probing particle is a photon exciting an electronic transition with no modification of the initial radiation [175].

UV-Vis spectroscopy is widely used for measuring the optical properties of materials, the possible adsorption of molecules on their surface, oxidation states, and electronic properties. The bandgap of semiconducting materials can be calculated from the UV-Vis adsorption using a Tauc analysis, which was demonstrated by Gao et al., who calculated the bandgap of phosphorene quantum dots fabricated with liquid phase exfoliation to be equal to 1.81 eV [176]. Liu et al. reported a change in the adsorption spectra of nitrogen-doped black phosphorus quantum dots after the introduction of a persulfate solution [177]. They also utilized adsorption spectra to show differences in optical properties between a hole-filled phosphorene and one with a continuous layer [178].

Chapter 5: Optical, electrochemical and structural properties of black phosphorus and black arsenic-phosphorus nanostructures

In this chapter, the fabrication methods and fundamental properties of BP and b-AsP nanostructures are presented. The studies described in this dissertation are my original work and a summary of my research. The fabrication method and investigation of the properties of BP-based structures were developed and conducted at the Gdańsk University of Technology and the Materials Characterization group at the University of Louisville Conn Center for Renewable Energy Research in cooperation with the Szewalski Institute of Fluid-Flow Machinery in Gdańsk and the Faculty of Physics at the University of Warsaw. All results, excluding electrochemical studies, presented in this dissertation were obtained by me:

- CVT processes,
- SEM imaging
- EDS mapping,
- Raman spectroscopy and spectra analysis,
- UV-Vis spectroscopy,
- AFM imaging and analysis,
- Photoelectrochemical studies,

or with my direct assistance:

- angle-dependent and temperature-dependent Raman spectroscopy,
- TEM and HRTEM imaging,
- EDS mapping and profiling of BP-TiO_2 NTs.

5.1 Chemical vapor transport for BP and b-AsP synthesis

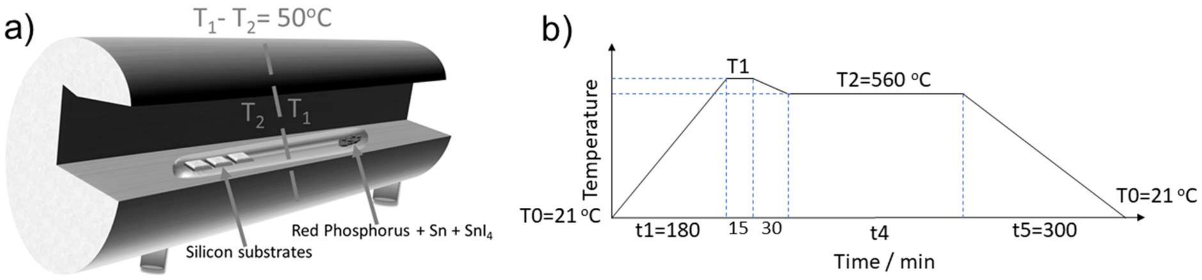

Figure 13. a) Schematic setup for BP and b-AsP nanostructures fabrication via CVT technique, b) temperature program designed for BP fabrication, temperatures are given for the hotter furnace zone.

Black phosphorus and black arsenic-phosphorus structures were fabricated using commercially available red phosphorus (250 mg), SnI_4 (5 mg), Sn (10 mg) and various amounts of As (for b-AsP structures) as precursors, which were placed in an evacuated quartz ampule. The reagents and silicon substrates were placed on opposite sides of the ampule. The tube was evacuated down to 10^{-5} Torr, using a pump system of my design, and sealed with an oxy-acetylene torch. The ampule was placed in a custom-made two-heating zone split tube resistance furnace (Fig. 13a) and underwent a two-step heating treatment followed by slow cooling to room temperature of 21°C. The specific temperatures of the hotter zone and annealing times are shown in Fig. 13b. The temperature gradient was to 50°C to ensure the phosphorus vapor transport process, with the reagents kept in a higher and silicon substrates in lower temperature (Fig. 13a). During the sealing process, the relative humidity in the laboratory was kept between 35%-40%.

In the first step of BP-based structures fabrication, I followed the CVT experimental details published by Köpf et al. for synthesis of bulk black phosphorus [5]. In this method, 500 mg of red phosphorus, 20 mg of Sn and 10 mg of SnI_4 were used as precursors, placed in an evacuated ampule and put through a specific temperature and time annealing process. With this starting point, I began to gradually lower the total mass of the precursors without changing the RP/Sn/SnI_4 mass ratio (Table 1.). The amount of final product seemed insufficient after lowering the mass of RP powder to 125 mg, therefore the precursor masses of 250 mg of RP, 20 mg of Sn and 10 mg of SnI_4 were used as standards for following experiments. In order to influence the balance of phosphorus vapor transport and deposition inside of the ampule I started placing silicon and gold or sulfur sputtered silicon substrates at the end of the ampule where phosphorus crystallization would occur. After the series of experiments with various substrates, times and temperatures obtaining mostly red (RP) and white phosphorus (WP) as final products, the conditions for black phosphorus (BP) columns fabrication was discovered (Exp-12 in Table 1). Afterwards, more changes in the fabrication procedure was made in order to explore the roles of precursors in the process. Nevertheless, after a few unsuccessful attempts, the thorough studies of obtained BP columns and their possible exfoliation became my priority closing the systematization of the fabrication process.

Table 1. Systematization of the fabrication process of BP-based structures: precursors masses, annealing times, maximum temperatures, substrates used and final products of the experiments.

No.	Precursors				Conditions			Product
	BP [mg]	RP [mg]	Sn [mg]	SnI4 [mg]	t4 [min]	T1 [°C]	Substrate	
Exp-1		500	20	10	720	610	none	bulk BP
Exp-2		250	10	5	720	610	none	bulk BP
Exp-3		125	5	2,5	720	610	none	bulk BP
Exp-4		250	10	5	720	595	Au on Si	RP layer
Exp-5		250	10	5	720	595	S on Si	BP/RP/WP layer
Exp-6		250	10	5	780	595	Au on Si	WP layer
Exp-7		250	10	5	840	595	Au on Si	RP/WP layer

Exp-8		250	10	5	720	610	Au on Si	RP/WP flakes
Exp-9		250	10	5	780	610	Au on Si	RP/WP crystals
Exp-10		200	8	4	780	610	Si	RP/WP crystals
Exp-11	220	250	10	5	840	610	Si	RP/WP crystals
Exp-12		**250**	**10**	**5**	**780**	**610**	**Si**	**BP columns**
Exp-13		500	20	10	780	610	Si	BP columns/BP crystals
Exp-14	260			6	780	610	Si	RP/WP layer
Exp-15		220		5	780	610	Si	RP/WP layer
Exp-16	110			2.5	780	610	Si	RP/WP layer

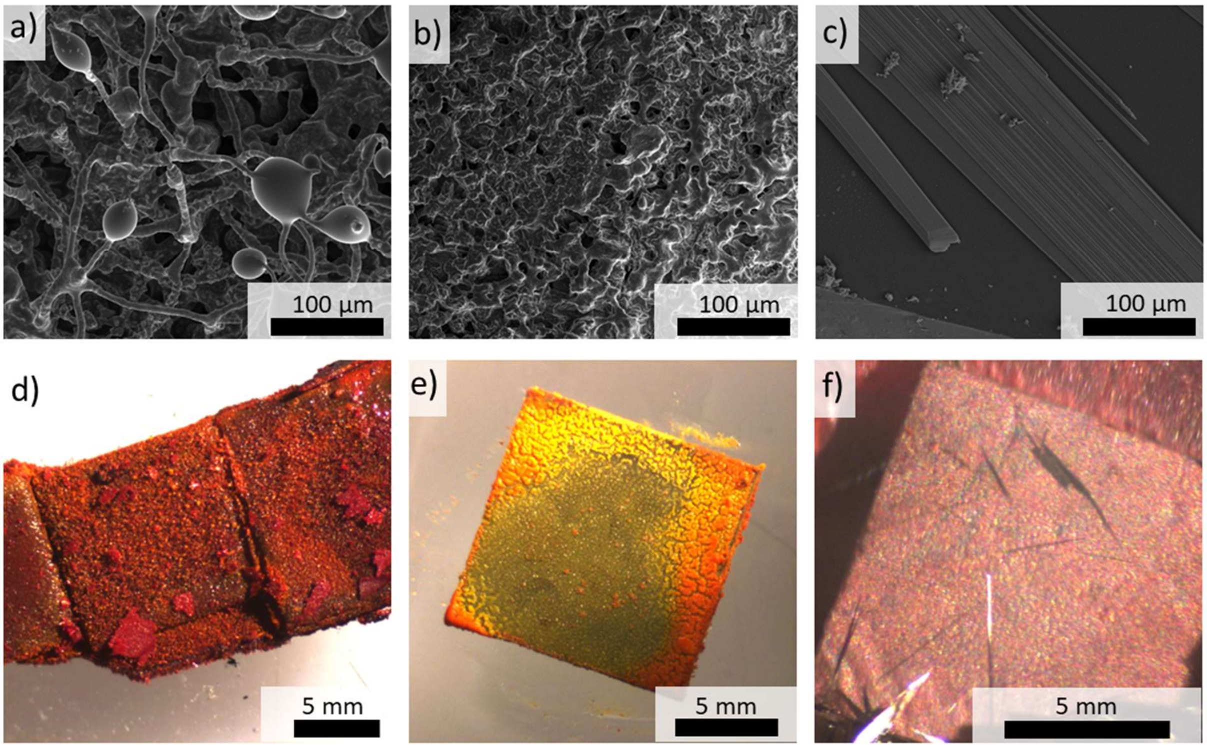

Figure 14. The summary of 3 phosphorus allotropes obtained by CVT method; a-c) SEM and d-f) optical microscope images of silicon substrates with synthesized red, white and black phosphorus respectively.

The cumulative results of 3 possible outcomes of the CVT process were used to identify the 3 phosphorus allotropes that can be obtained in this experiment. In order to do so, Raman spectra (Renishaw inVia Raman Microscope) and SEM images (FEI Nova 600) were collected. The optical microscope and SEM images as well as their Raman spectra are presented in Fig. 14 and 15, respectively. In most cases, the allotropes can be accurately identified with optical images (Fig. 14 d-f), as red, white or black colored layer is formed on the substrate. Sometimes however, more than one allotrope can be present in the final product (Table 1) and in order to confirm the crystallinity of the sample, SEM imaging or Raman spectroscopy must be conducted. Surface morphology of red phosphorus shows a spiderweb-like structure with smooth edges and inflated endings, similar to [179]. In case of white phosphorus, it is difficult to conduct additional studies of this allotrope since it reacts with oxygen, instantly burning on contact with air (the optical images were collected when the sample was still in the ampule). Nevertheless, the surface morphology of the burned out sample shows a layer without any specific crystallites, similar to the structure reported by Xiao et al. [180], who identified it as amorphous red phosphorus. Black phosphorus structures, presented in Fig. 14c and f, are characterized by well-defined elongated structures, sharp edges and layer stacking, clearly visible in higher magnifications of SEM images (more examples in section 5.3).

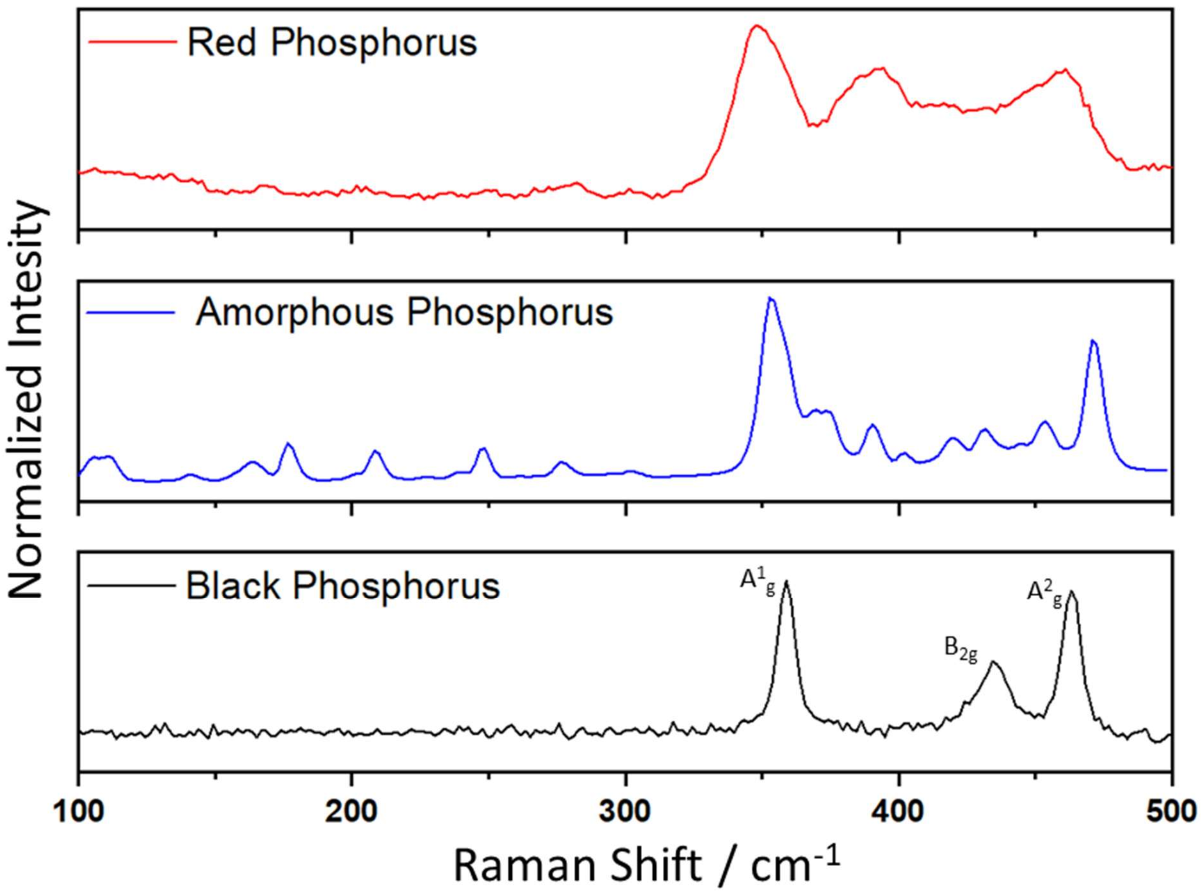

Figure 15. Raman spectra collected for red, red amorphous and black phosphorus synthesized on silicon substates using CVT technique.

However, the most decisive method for phosphorus allotrope identification is Raman spectroscopy. The exemplary Raman spectra recorded for RP, WP and BP are presented in Fig. 15. The results can be easily distinguished between the 3 allotropes with red phosphorus spectra (red line) showing a broad band with 3 maxima in range of 340-460 cm^{-1} [181]. The amorphous phosphorus (blue line), being the remnants behind white phosphorus, shows a complicated spectrum with multiple sharp Raman lines below 300 cm^{-1} [182]. The Raman spectra recorded for black phosphorus structures (black line) show

3 distinctive, narrow peaks corresponding to A^1_g, B_{2g} and, A^2_g vibrational modes with maxima around 362 cm $^{-1}$, 438,6 cm $^{-1}$ and 466 cm $^{-1}$ at room temperature respectively [183].

The fabrication method of BP structures described in this section in the primary technique used for BP and b-AsP nanostructures fabrication (excluding BP nanosheets) and surface modifications of electrode materials described in this dissertation.

5.2 Black phosphorus nanosheets

As previously mentioned, BP nanosheets can be fabricated by mechanical exfoliation of a BP crystal or via liquid-phase exfoliation of BP in organic solvents such as: NMP, DMSO, and Et_2O [184]. Liquid-phase exfoliation is more time-consuming and reduces the lateral size of the fabricated BP flakes when compared to mechanical exfoliation [56]. However, the size and concentration of the fabricated flakes can be influenced by choosing a specific solvent [184].

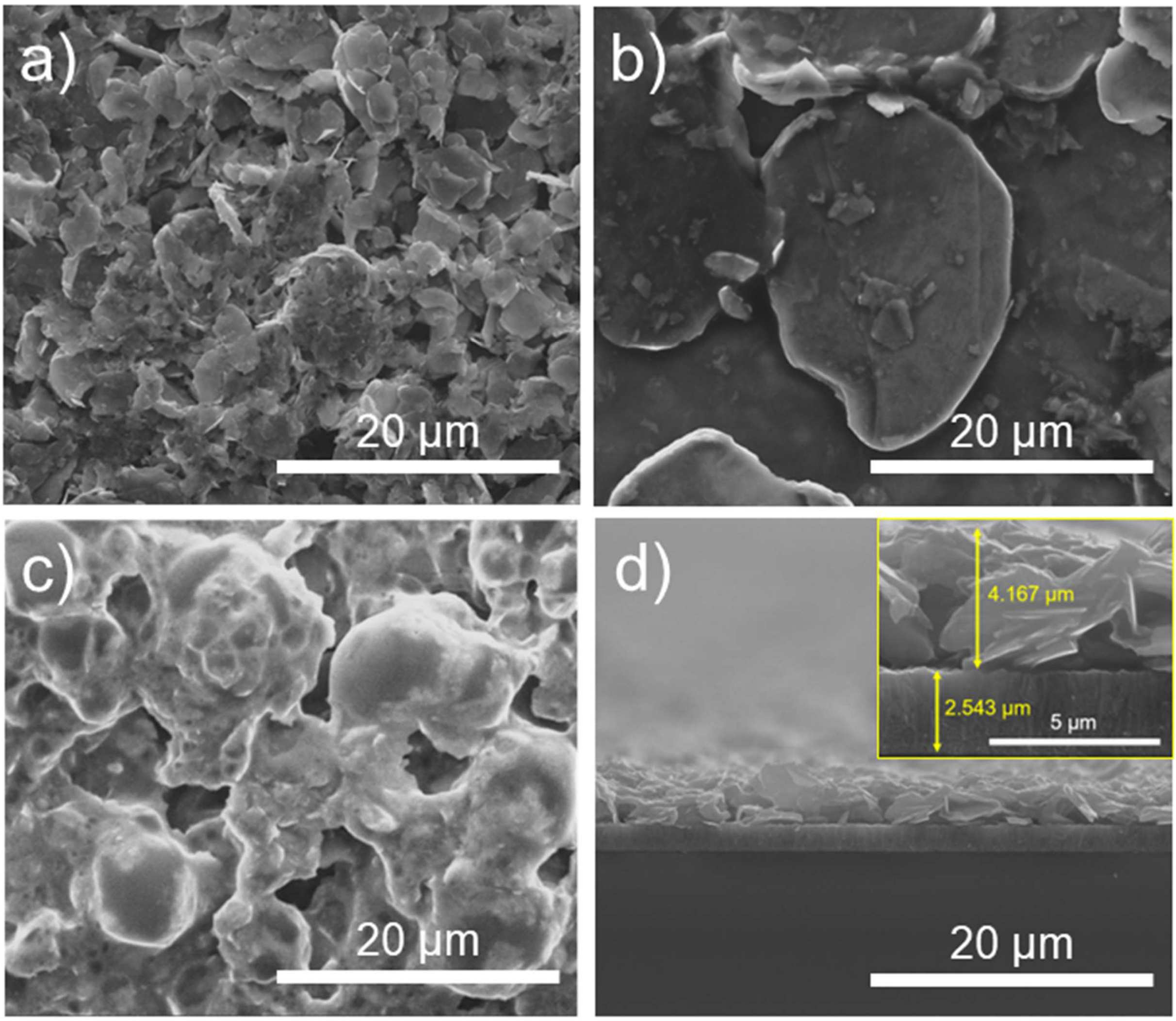

Figure 16. Surface morphology of BP flakes exfoliated in a) NMP, b) Et_2O and c) DMSO; d) cross-section SEM image of BP flakes exfoliated in NMP and drop-casted onto Si substrate.

To fabricate black phosphorus nanosheets, a pre-crushed BP crystal was added to three anhydrous solvents: NMP, DMSO, and Et_2O under an argon atmosphere. The exfoliation setup consisted of a horn probe ultrasonicator (Bandelin Sonopuls HD2200, 20 kHz, 50/50-time amplitude) and bath sonication (Polsonic 3, 160 W, 40 kHz). The samples were kept under a stream of nitrogen with a 2011 dm^3/h flow rate for cooling purposes. The sonication-aided exfoliation took 60 min, and the solutions were cooled for 10 min afterwards. The so-prepared solutions of exfoliated black phosphorus dispersed in 3 polar solvents were drop-cast on silicon wafers and moved to a vacuum oven for solvent evaporation.

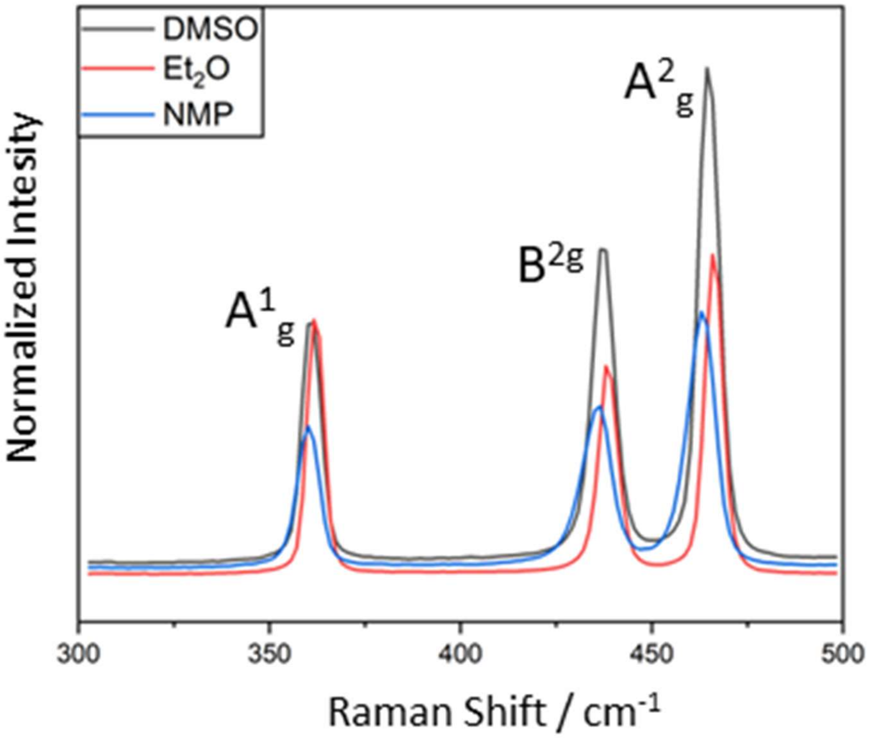

Figure 17. Raman spectra of BP flakes exfoliated in NMP, Et_2O and DMSO.

The surface morphology analysis of the BP flakes exfoliated in NMP (Fig. 16a), Et_2O (Fig. 16b) and DMSO (Fig. 16c) was carried out by scanning electron microscope (FEI Quanta FEG250). The SEM images reveal the exfoliation and drop-casting processes to be successful for BP sonicated in NMP and Et_2O, resulting in the formation of BP nanosheets of diverse sizes (Fig. 16a,b). Despite the surface morphology of the BP flakes exfoliated in DMSO not being as well defined, the distribution of presented structures is similar to the other samples, which may indicate that BP flakes successfully formed. However, the visible charging effect on the surface of the flakes may be caused by not fully evaporated DMSO from the Si wafer. To determine the thickness of the BP layer sonicated in NMP and drop-casted on the silicon substrate, a cross-section analysis was carried out (Fig. 16d), showing the thickness of the BP nanosheet layer to be 4.137 μm. Overall, the surface morphology analysis of all samples reveals a strong influence of the solvent chosen for the fabrication process on the shape, size, and distribution of the synthesized BP nanosheets.

The Raman spectra of BP exfoliated in 3 solvents were recorded on a confocal micro-Raman spectrometer (InVia, Renishaw) with an excitation wavelength of 514 nm, by an argon ion laser operating at 1% of its total power (10 mW). The Raman spectra show noticeable maxima near 363 cm^{-1}, 439 cm^{-1}, and 467 cm^{-1}, corresponding to A^1_g, B_{2g} and, A^2_g modes, respectively (Fig. 17) [171]. In the experiment, anhydrous polar solvents were used, which do not cause rapid decomposition of the phosphorene structure and for each spectrum, characteristic mods can be identified, corresponding to the molecular structure of phosphorene [185]. On the other hand, changes in the size of the nanosheets were observed due to different polarities similar to results reported by [56] and [186]. Moreover, the Raman spectra observed for the BP nanosheets sonicated in DMSO also exhibit modes characteristic of BP nanostructures, which, in contradiction to the SEM images, may indicate the successful formation of BP nanosheets during the liquid-exfoliation process. The observed Raman bands vary slightly in the position and width of the vibrational modes, with flakes exfoliated in NMP exhibiting a slight blue shift in comparison to the other samples. The computational studies show a correlation between the material strain and the vibrational frequency of each mode. A numerical simulation suggests that the blue shift can be attributed to a weak compressing strain [187]. This stress can be associated with bending forces occurring in thin films deposited on the substrate [188], which can also be observed in the SEM image of this sample (Fig. 16a).

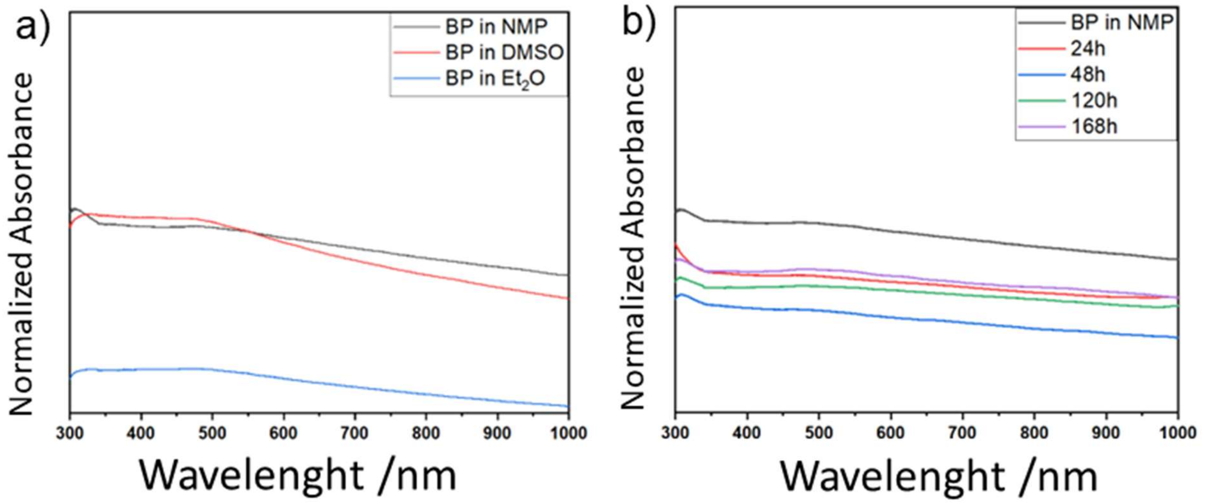

Figure 18. a) Absorbance spectra recorded for BP flakes exfoliated in NMP, DMSO and Et_2O immediately after synthesis and b) repeated for BP nanosheets exfoliated in NMP 24, 48, 120 and 168 hours.

Optical absorption spectra were obtained using double beam UV-9000, Metash spectrometer. The absorbance spectra were collected in a differential mode, subtracting data collected beforehand for specific solvent from the spectrum and averaged from 5 measurements with scanning speed of 1 nm/s and 0,1 nm resolution. The exfoliated BP nanosheets were kept in room temperature of 21^{o}C dispersed in solvents in vials covered with aluminum foil to prevent sunlight-induced structure reduction [189]. UV-Vis measurement can be a valuable tool, often used to obtain quantitative information about the BP thickness, and the stability of the fabricated structures [190,191].

Absorbance spectra of BP nanosheets fabricated by liquid phase exfoliation in NMP, DMSO and Et_2O are presented in Fig. 18a. The measurements were carried out for BP flakes dispersed in chosen solvents by diluting the solution in the appropriate solvent and followed by centrifugation. The absorbance spectra recorded BP nanosheets dispersed in DMSO and NMP revealed the sample to be optically active across the whole analyzed range, with the intensity increasing toward lower wavelengths, which was also reported by Lee et al. [192]. Moreover, the absorption spectrum shows an electronic band-to-band transition at 480 nm (2.48 eV). According to Woomer et al., this energy range corresponds to a system of 4-layer-dominated structures in the solution [193]. BP nanosheets dispersed in Et_2O exhibit low optical activity, which was also reported by [194]. Zhang et al. reported that, even if a solvent is capable of BP exfoliation, it may not suspend the material efficiently. Moreover, comparison of the BP concentration with the surface tension in different solvents shows that BP exfoliation yield increases monotonically with surface tension [195].

The surface morphology and optical activity of exfoliated BP nanosheets, revealed NMP to be the most efficient, out of the 3 tested solvents, with high optical activity of BP flakes and regularly covered surface of silicon substrate. The initial BP flakes absorbance dispersed in NMP was recorded directly after exfoliation and repeated after 24, 48, 120 and 160 hours (Fig. 18b), with the centrifugation repeated for each measurement. The UV-Vis absorption spectra show that the optical activity of BP flakes dispersed in NMP vastly decreases as soon as 1 day after the fabrication process, which can be attributed to reaction with residual water/oxygen in used solvent and could cause a small decrease in absorbance observed over the 2 days [65]. The optical activity of dispersed BP nanosheets increase after 5 and 7 days which may be caused by the continues oxidation process changing the BP surface to hydrophilic, leading to the P-P bond breaking. And subsequently, a local structural transformation from an orthorhombic lattice to rhombohedra-like symmetry [196].

The morphology of phosphorene flakes layer granting enormous surface-to-volume ratio, high optical activity and chemical stability (reported in my previous work [197]) enable this material to be implemented as sensors [198] and electrode materials [199], proving **hypothesis I**. Moreover, the enormous surface-to-volume ratio [200] and high biocompatibility [201] allow a singular BP sheets to be applied as platform for sensitive and specific biomolecule sensing [202] or field-effect transistor biosensors [202], applications unachievable for bulk material. The above mentioned applications of BP nanosheets and many more being continually reported [203–205] show the constant relevance of low-dimensional semiconductor materials in novel technological solutions.

5.3 Black phosphorus nanoribbons

In recent years, significant interest has been developed toward low-dimensional structures. As previously mentioned, downsizing 3D materials leads to structures that exhibit quantum confinement and develop extraordinary properties such as: enormous surface-to-volume ratio, large number of active sites, and prominent edges. Theoretical studies have shown that phosphorene nanoribbons could surpass the mechanical and optical properties of phosphorene nanosheets [206].

Moreover, by controlling the dimensions of the BP nanoribbons, one can influence their electronic structure and carrier mobility, as reported by Jing et al. [207]. The production of thin BP nanoribbons still remains a challenge with most techniques being either too expensive or too time-consuming to apply them for large-scale production [208,209]. In this study, a novel approach toward BP nanoribbons and nanobelts using a combination of the CVT technique and sonication is proposed.

In this study, Raman spectroscopy of BP columns was performed on a Renishaw inVia Raman Microscope, equipped with a 532 nm emission line Nd:YAG laser. The angle-dependent Raman measurements were performed using λ = 632.8 nm He–Ne laser (setup described in detail in section 5.5). Surface morphology of the samples was investigated using FEI Nova 600 scanning electron microscope. The thickness measurements of exfoliated BP nanoribbons were performed on an Asylum MFP-3D-Bio atomic force microscope and analyzed using Gwyddion open source software [210].

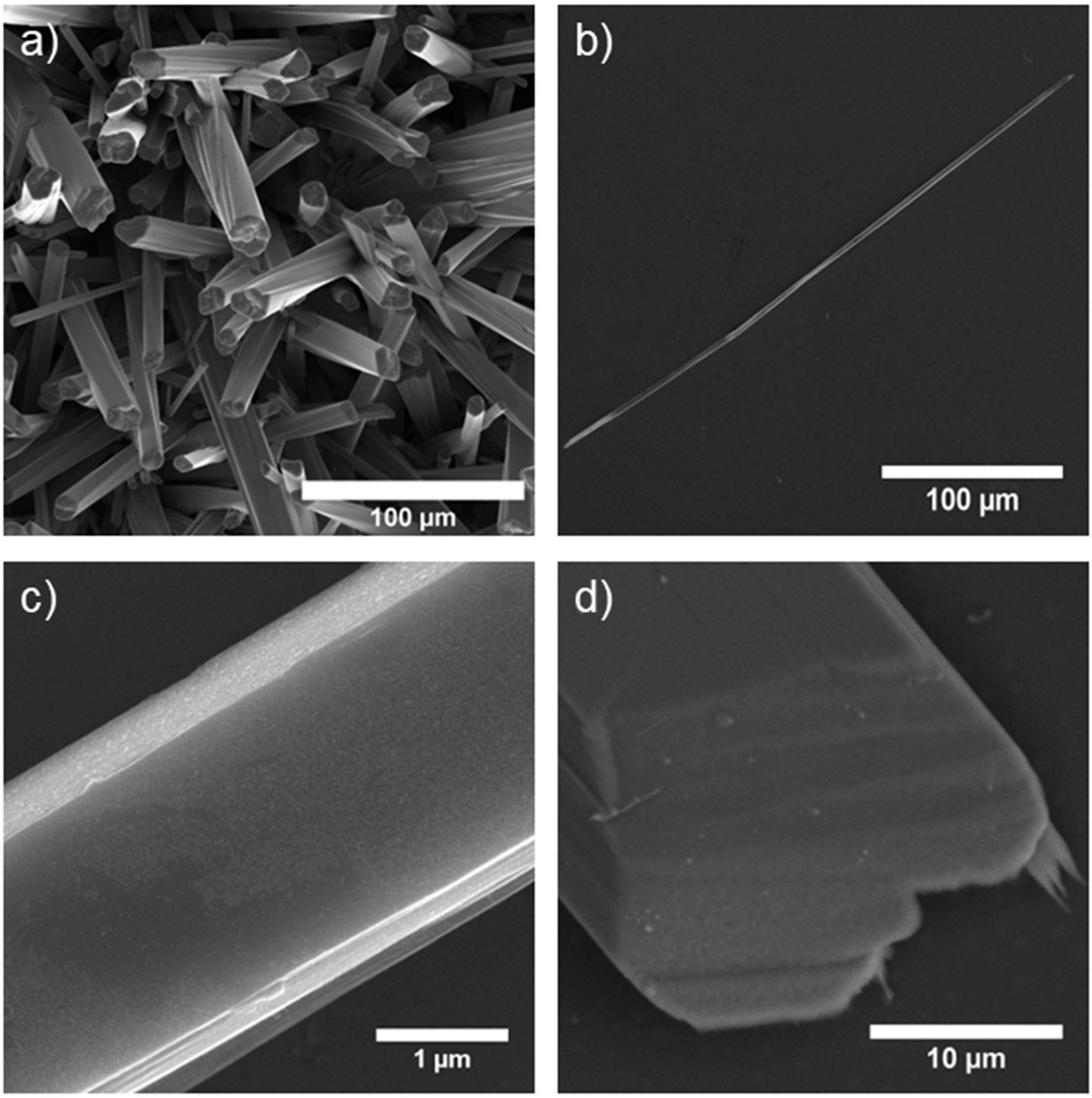

Figure 19. Surface morphology of BP a) column layer formed on Si substrate after CVT process, b) exfoliated single BP column; and enhanced SEM images of c) top surface and d) front of a single BP column.

The parameters of the fabrication process of BP columns are described in Table 1. of section 5.1 as Exp-12. After the synthesis and cooling the ampule to 21°C, a layer of BP columns had formed on the silicon surface (Fig. 19a). The sample was kept in an argon glove box to prevent any degradation. The SEM images of BP columns that are presented on Fig. 19a–d show the columns to form regular, layered structures of sharp edges, which can be easily exfoliated. The crystallinity of CVT-grown structures was investigated using Raman spectroscopy. The recorded spectra show 3 narrow peaks corresponding to A^1_g, B_{2g} and, A^2_g vibrational modes with maxima around 362 cm $^{-1}$, 438,6 cm $^{-1}$ and 466 cm $^{-1}$ [183]. The anisotropic structure changes of low-dimensional BP could induce an anisotropic variation of optical properties (Raman scattering) or electronic structure, which allows changes in intensity ratio in recorded Raman spectra as a function of thickness, according to theoretical predictions [211,212]. Hence the differences between intensities ratio of CVT-grown BP nanosheets and columns presented in figures 15, 17 and 20.

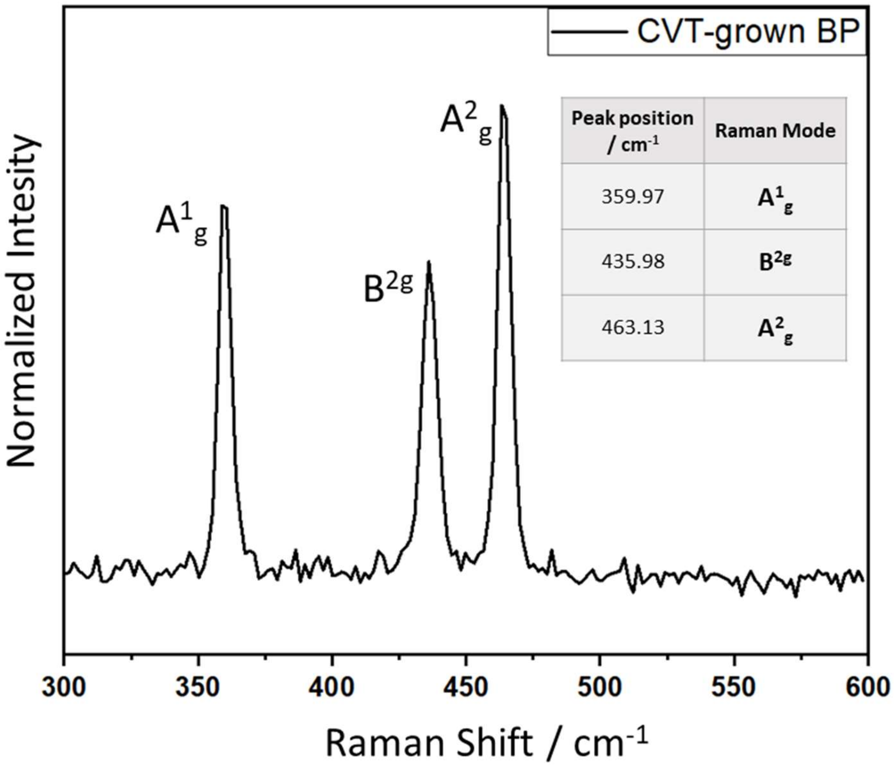

Figure 20. Raman spectra recorded for BP columns synthesized by chemical vapor transport.

To preserve the original width and length of the fabricated structures, the columns were subjected to ultrasonication and centrifugation in 5 ml of DMF (Fig. 21). The solution was subsequently drop-cast onto a clean silicon wafer and dried in a vacuum oven for further measurements. It can be seen, that nanoribbons exfoliated by this method have 1,38 μm in width, similar to the initial BP columns (Fig. 21b,c). Mechanical exfoliation could also be a valid method; however, it could break or deform such structures. More information and a broader analysis of BP columns fabricated with the CVT technique can be found in the previously mentioned paper [213].

In order to investigate the thickness of fabricated phosphorene nanoribbons, AFM studies was conducted. Figure 22a show AFM images of surface morphology of 2 phosphorene nanoribbons drop-casted on the silicon substrate. The BP nanoribbons were measured along the width and length using 2 profiling lines for each nanoribbons (Fig. 22b-h). The investigated nanoribbons have 0,16 and 0,14 μm in width respectively, which is lower than presented above, however grown BP columns differ in dimensions as presented in Fig. 19a and exfoliation process also affects narrower structures. Considering that monolayer phosphorene is slightly larger than the interlayer distance in the black phosphorous crystal (0,55 nm) is because that first layer sits slightly proud of the surface (ca. 35 nm).

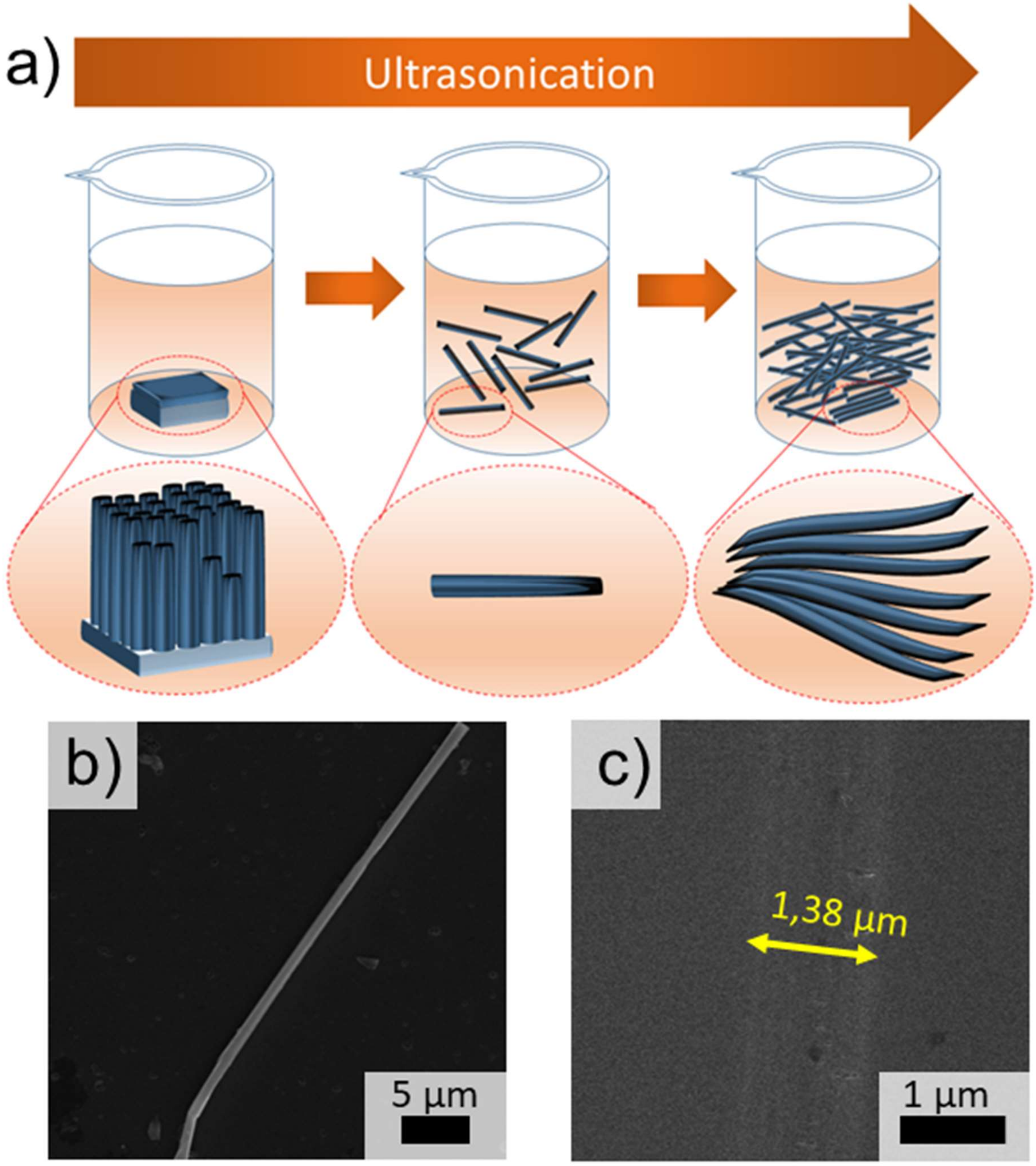

Figure 21. a) Exfoliation process of BP columns into BP nanoribbons, b) and c) SEM images of single BP column and phosphorene nanoribbon respectively.

However, subsequent layers stacking of BP layers will sit above the first layer at the same distance as is found in the bulk crystal. Therefore thickness of monolayer phosphorene would be around 0,9 nm, bilayer around 1,45 m, around 2nm in case of trilayer etc. [172,214]. Thus, the thickness measurements reveal the fabricated BP nanoribbons to be 1,6 and 1,3 nm at most, which corresponds to up to 2 layers of black phosphorus. The lengths of both nanoribbons are measured and are equal to 0,85 and 1,35 µm so the length to width ratio between 5-10, similar to majority of phosphorene nanoribbons fabricated using lithium intercalation reported by Watts et al. [65]. The crystallinity and structural orientation of fabricated nanoribbons is investigated using Raman angle-dependent spectroscopy.

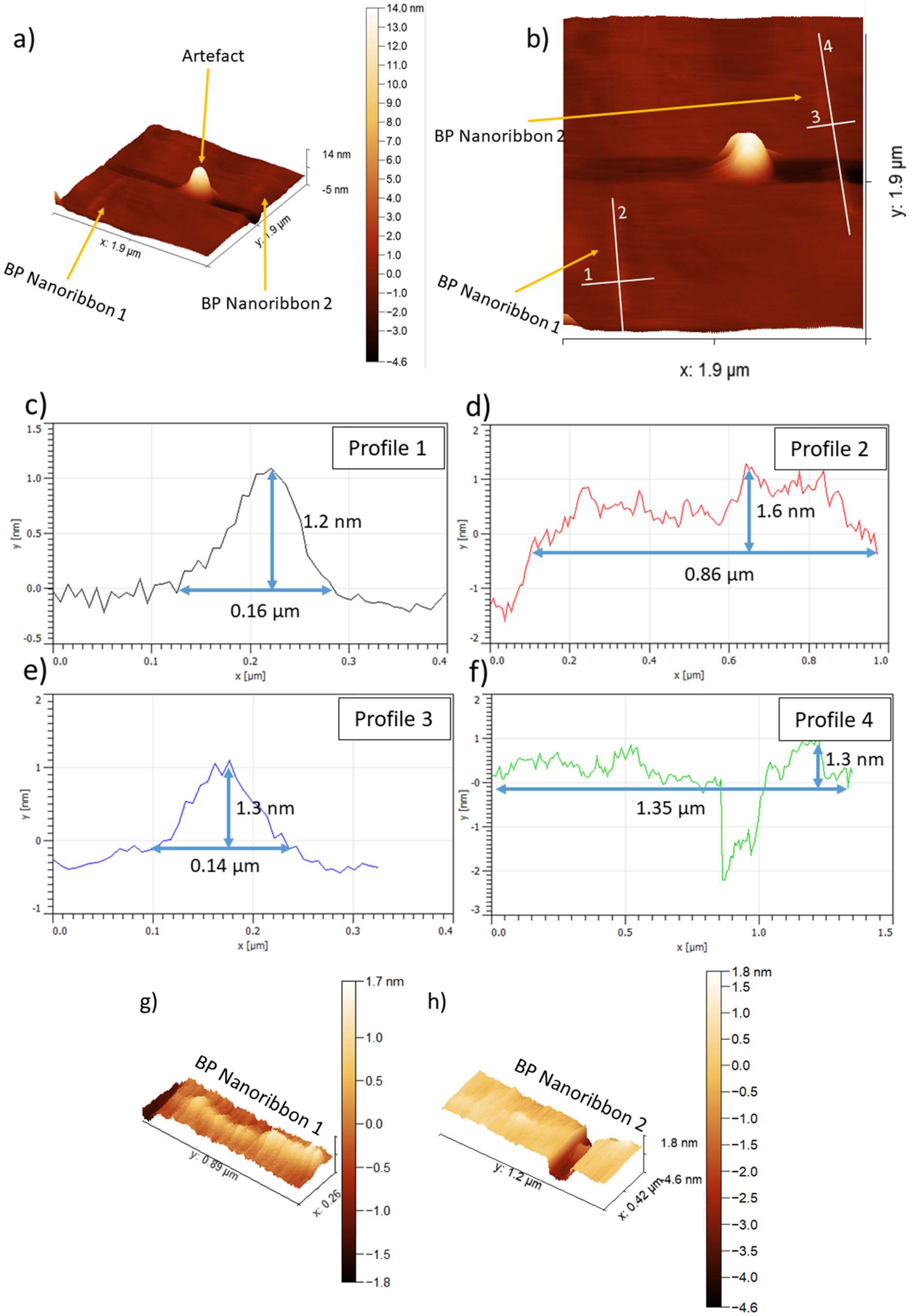

Figure 22. AFM studies of 2 phosphorene nanoribbon drop-cast onto a Si substrate a-b) and g-h) AFM images and c-f) line profiling across and along of the nanoribbons.

The Raman spectra recorded for BP nanoribbons show all A^1_g, B_{2g} and, A^2_g vibrational modes at 361,3, 437,7 and 465,1 cm^{-1} respectively, which is similar to spectra presented previously (Fig. 15,17,20) pointing to the nanoribbons to consist of black phosphorus. Instead of duplicating similar results, the comparison of the position of the vibrational modes in the Raman spectra of the fabricated nanoribbons (orange area) and the position of the Raman modes for BP nanostructures obtained by other scientific groups are presented in Fig. 23a [68,171,215,216].

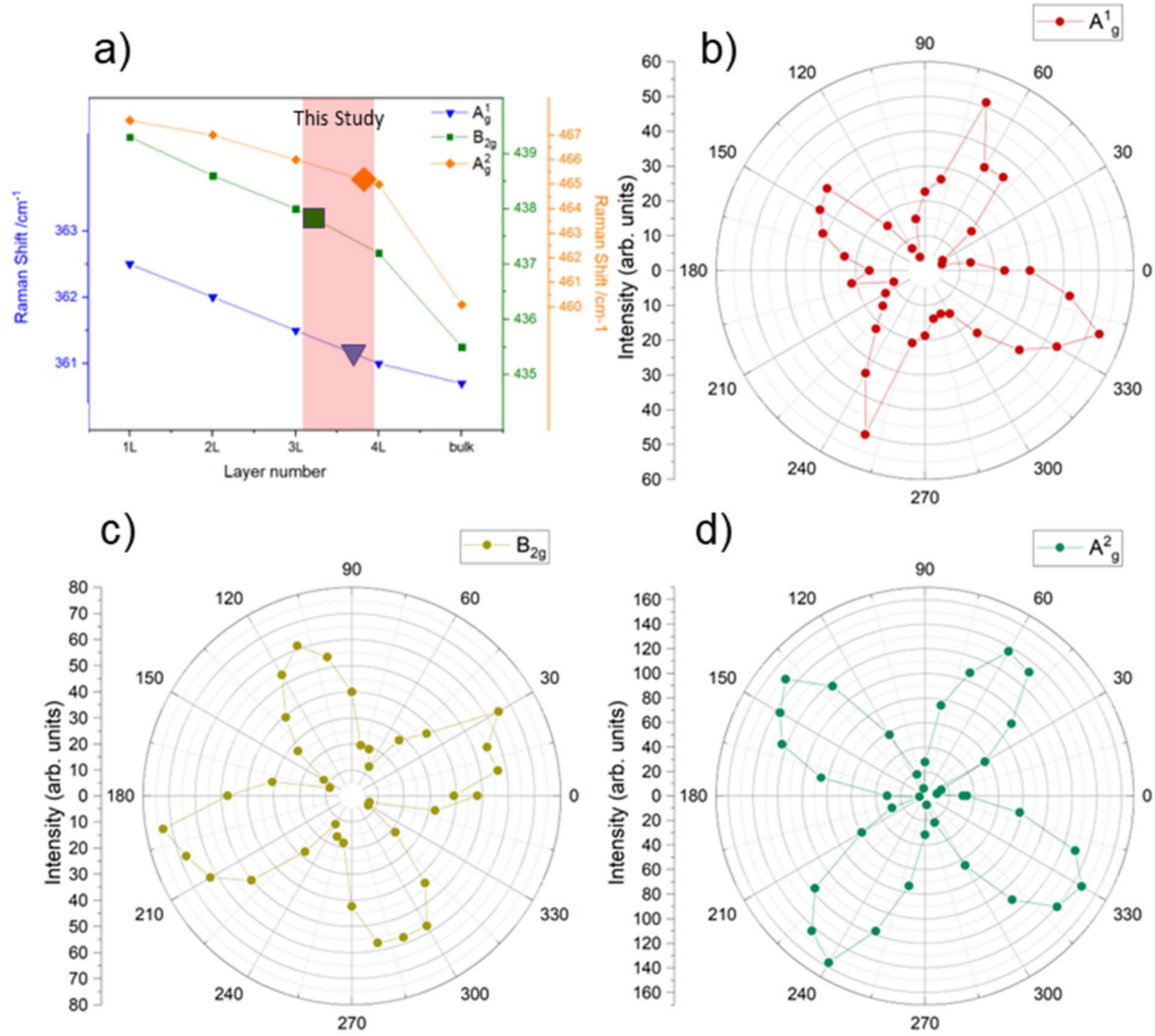

Figure 23. Raman studies of phosphorene nanoribbons: a) fabricated phosphorene nanoribbon vibrational modes' positions in comparison to literature, b–d) angle-dependent Raman spectra of 3 vibrational modes of phosphorene nanoribbon.

It is worth mentioning that the state-of-the-art Raman modes are mostly measured for phosphorene flakes and nanosheets, rather than nanoribbons, which may cause slight discrepancies in the presented results due to red or blue shifts caused by internal stress, and consequential to a high length/width ratio of the nanoribbons [217]. Nonetheless, the comparison of vibrational modes position of the obtained Raman spectra (Fig. 23a) further confirm the BP nanoribbons to consist of a few (less than 4) layers .

The structural orientation of the fabricated phosphorene nanoribbon was established using linearly polarized Raman measurements. The initial polarization plane angle was shifted by 54° relative to the longitudinal plane of the ribbon, which needs to be taken into account when analyzing Fig. 20c,e and f. It can be seen that all Raman intensities of the A^1_g, B_{2g}, and A^2_g modes are dependent on the polarization angle and show an angle period of 90°. Moreover, the A^1_g and A^2_g modes exhibit 4 intensity maxima at 0, 90, 180 and 270°, while the B_{2g} mode is shifted by 45° with maxima at 45, 135, 225, and 315°. According to Akhtar et. al, in the A^1_g and A^2_g vibrational modes, the phosphorus atom oscillates along the zigzag or out-of-plane directions, while the B_{2g} mode can be associated with armchair-direction oscillations [215]. These results reveal that the zigzag direction is the orientation of the fabricated BP nanoribbons that is in agreement with previously published computational studies suggesting the growth of BP columns to be more energetically favorable in the zigzag direction [213].

In summary, a novel approach to the fabrication of BP nanoribbons has been presented. The Raman studies confirm the monocrystalline nature of the fabricated structures and can be utilized for the designation of ZZ and AC directions. The dimensions of the fabricated structures can vary from a few hundred nm to a few µm, allowing separation of BP nanoribbons with specific optical and electronic properties [206,218,219]. Thus, the proposed fabrication method unlocks quantum confinement effects in BP nanostructures which allow this material to be widely applied in transistors [220,221] and sensing devices [222,223], proving **hypothesis I** of this dissertation.

5.4 Black phosphorus-modified TiO_2 nanotubes

In the last decade, titania nanotubes have attracted noticeable attention in nanomaterial science due to their inherent properties such as biocompatibility, chemical and physical stability, non-toxicity, and high corrosion protection. However, as mentioned in the previous chapters, TiO_2 NTs are active only in the ultraviolet area and have a high carrier recombination rate during photocatalytic processes [224].

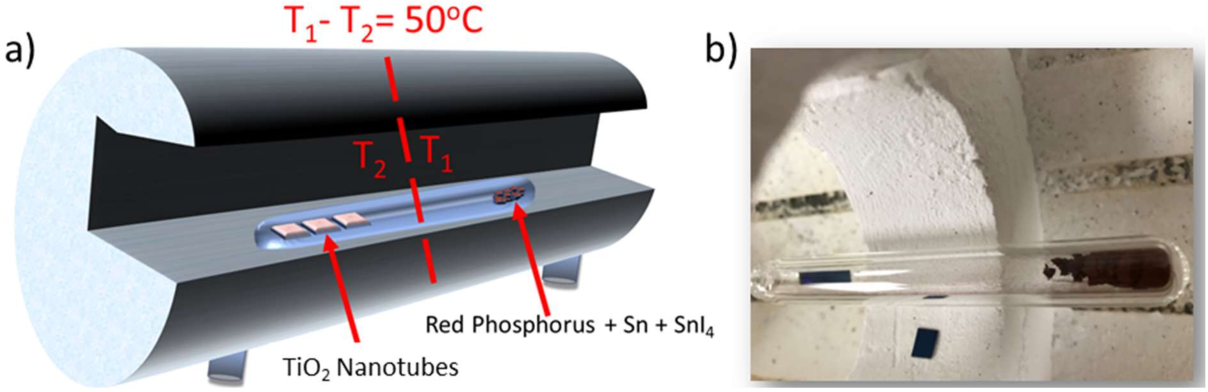

Figure 24. a) setup used for TiO_2 NTs modification with BP, b) optical image of the quartz ampule in the tube furnace with TiO_2 NTs and precursors.

Shifting the border of its photoresponse into the visible region would enhance its potential for solar energy harvesting and other applications such as optoelectronic switches [225] and photo-electrochemical sensors [226]. In general, there are two strategies two achieve this goal, which are bulk doping or surface modification of titania. In the former, nonmetals [227] or transition metals [228] are incorporated into the structure of titania introducing intra-bandgap acceptor and donor levels. The other approach, surface modification, is usually carried out by attaching various light absorbing structures, like quantum dots [229], transition metal complexes [230] and nonmetals [231], to the surface of nanotubes.

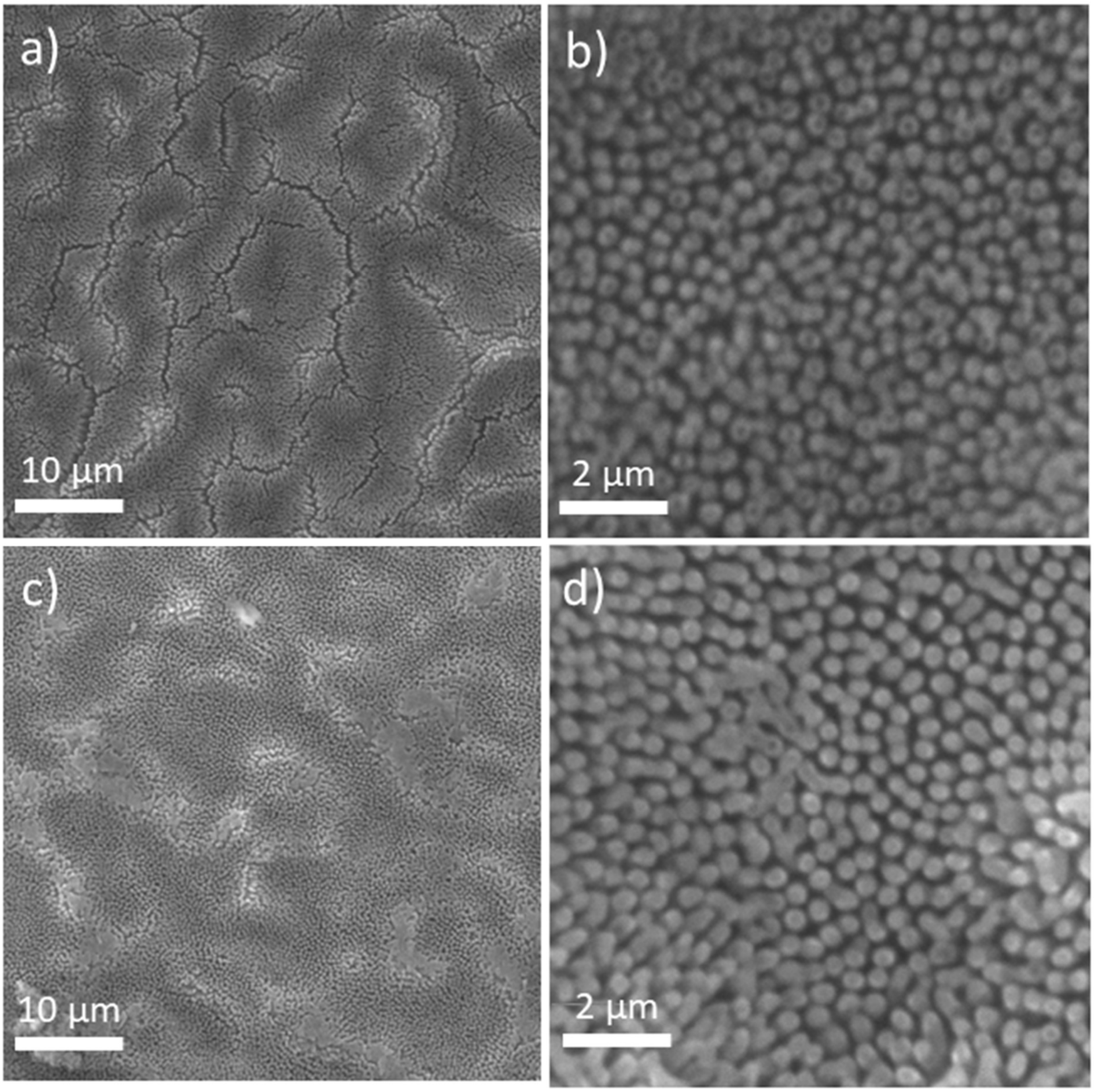

Figure 25. a–b) surface morphology of pristine and c-d) BP-modified TiO_2 NTs.

The previously described CVT technique was utilized to modify TiO_2 NTs with black phosphorus. Highly ordered titania nanotubes were fabricated using the 2-step anodization technique, as was described in chapter 3. The modification procedure was identical to the first step of the fabrication of the BP columns with the exception of replacing the silicon substrates with TiO_2 NTs (Fig. 24a,b).

In this study, Raman spectroscopy was performed on a Renishaw inVia Raman Microscope, equipped with a 532 nm emission line Nd:YAG laser. The analysis of Raman spectra was done using OriginLab software, which was utilized for peaks position identification [232]. Surface morphology of the samples was investigated with the same setup as BP nanoribbons (FEI Nova 600 SEM). The high resolution images, EDS mapping and profiling of BP-TiO_2 NTs were obtained with a FEI Tecnai F20 standard transmission electron microscope.

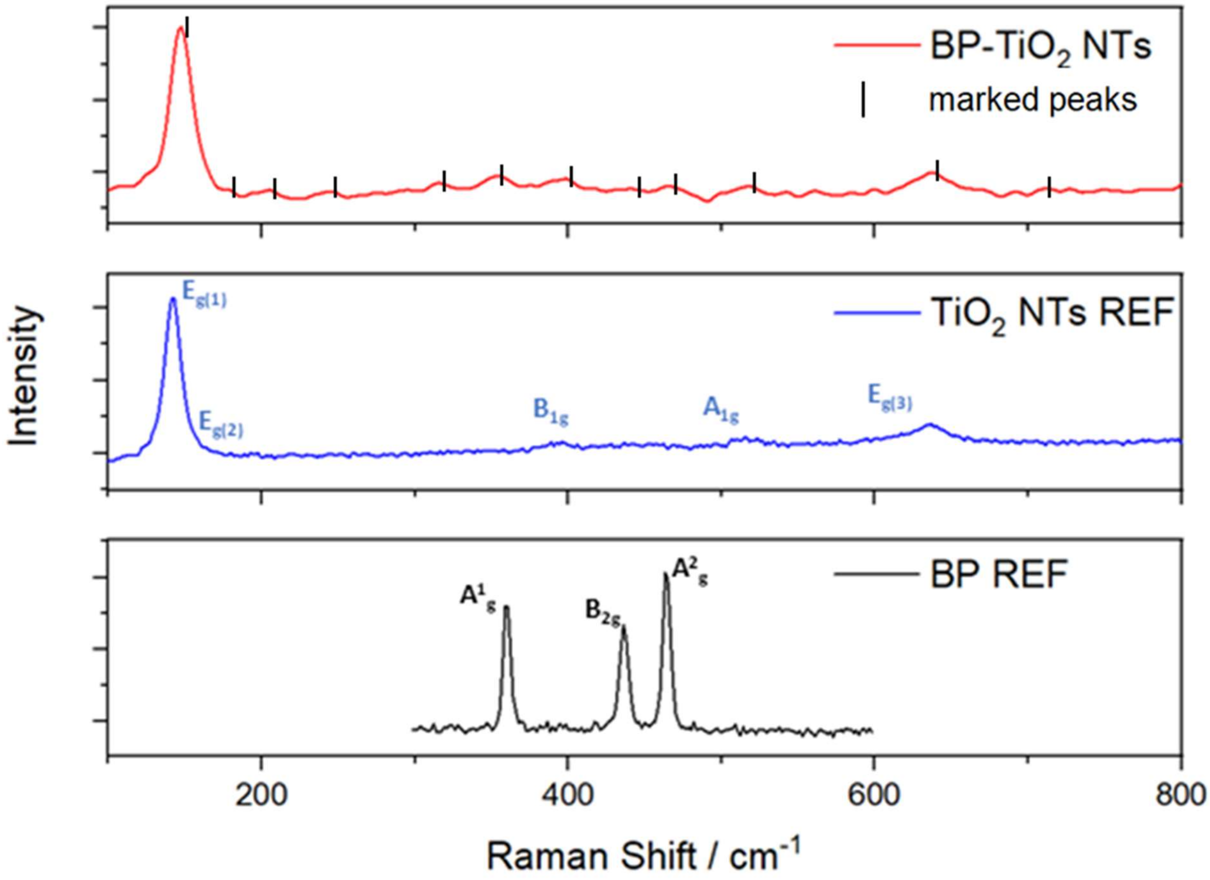

Figure 26. Raman spectra measured for BP (black), TiO_2 NTs (blue) and BP-modified TiO_2 NTs (red).

The SEM images (Fig. 25a–d) show the surface morphology of the pristine and BP-modified TiO_2 NTs. The nanotubes layer is regular with NTs having similar diameters (Fig. 25b) and some microcracks occurring over the entire surface, which is typical for these structures [233]. The BP-TiO_2 NTs macrostructure reveal the modification process to fill those cracks (Fig. 25c). Moreover, the high-magnification image (Fig. 22d) shows some nanotubes to be clogged or covered with a thin layer, which suggests the modification process to be successful and can be further confirmed with EDS and Raman studies. In order to prove the results of the modification process, Raman (Fig. 26) and TEM (Fig. 27,28) studies were conducted. The Raman spectra recorded for BP-TiO_2 NTs were analyzed using OriginLab software identifying all expected vibrational modes: A^1_g, B_{2g}, and A^2_g, characteristic for black phosphorus (black line) and the $E_{g(1)}$, $E_{g(2)}$, B_{1g}, A_{1g}, and $E_{g(3)}$ modes of anatase TiO_2 nanotubes (blue line) showing high crystallinity of the modified NTs.

Table 2. Marked peak position of Raman spectra recorded for BP-modified TiO_2 NTs, reference TiO_2 NTs and reference bulk BP and their attribution to corresponding vibrational modes.

Marked peak position / cm^{-1}			**Modes Identified as:**
BP-TiO_2 NTs	**TiO_2 NTs REF**	**BP REF**	
146,83	**142,13**	**-------**	**$E_{g(1)}$**

178,36	171,61	-------	$E_{g(2)}$
205,38	-------	-------	-------
244,49	-------	-------	-------
314,32	-------	-------	-------
354,18	-------	357,72	A^1_g
398,02	391,47	-------	B_{1g}
440,06	-------	436,6	B_{2g}
465,85	-------	464,21	A^2_g
517,62	516,79	-------	A_{1g}
637,41	635,97	-------	$E_{g(3)}$
711,67	-------	-------	-------

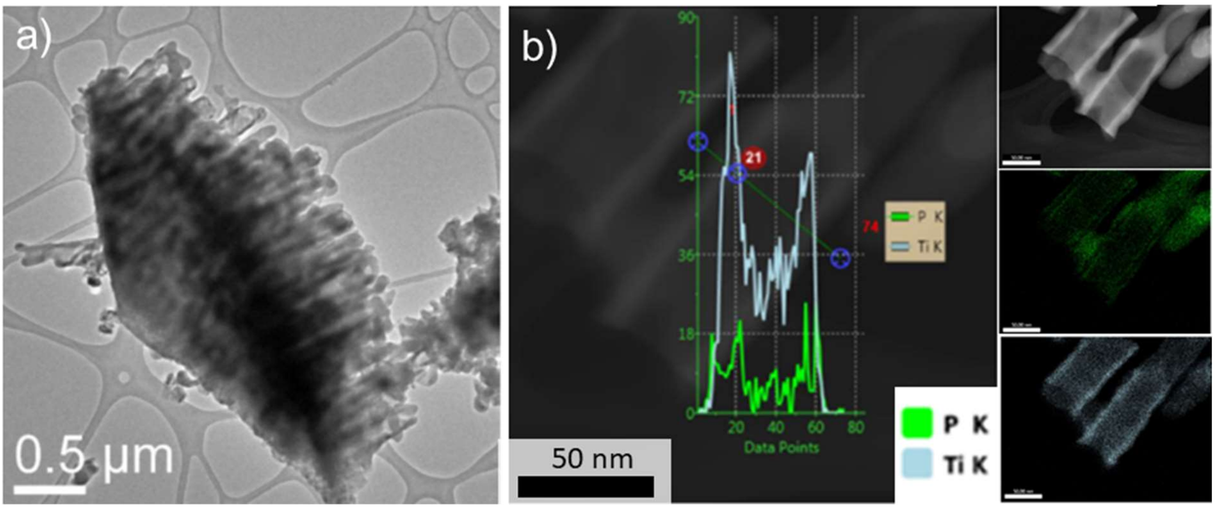

Figure 27. a) HRTEM image and b) EDS line profiling of a separated fragment of BP-modified TiO_2 NTs.

The positions of all identified Raman lines are listed in Table 2. There are some unidentified maxima present in the BP-modified TiO_2 NTs Raman spectra, that can be connected to the oxidation of the surface layer. Because the oxidation occurs layer by layer, which tends to completely changes the Raman signal of the top layers, leaving the underneath layers nearly unperturbed [234]. However, despite numerous reports of BP modifications of titania, there is very little to none information on this subject [235–237], presenting possibilities to gain insight into the structural and optical properties with additional Raman studies.

The TEM-based analysis was performed on a piece of BP-modified TiO_2 NTs substrate (Fig. 27a). The BP modification was further investigated using EDS line profiling (Fig. 27b) and mapping (Fig. 28). The results show the modified nanotubes to be around 60 nm in diameter (Fig. 28) with a thin phosphorus layer forming on both the inside and outside wall of titania NTs (right columns of Fig. 28). The EDS line profiling measurements further confirms the measured diameter of TiO_2 NTs also revealing the inner and outer layers of BP to be around 5 nm thick (Fig. 27b). The results suggests that by using TiO_2 NTs as a matrix and removing them after the modification process, it could be possible to produce phosphorene nanotubes, which are yet to be experimentally fabricated, as simulated by Bhuvaneswari et al. [238]. Overall, the presented results show that the CVT technique is applicable for TiO_2 NTs surface modification.

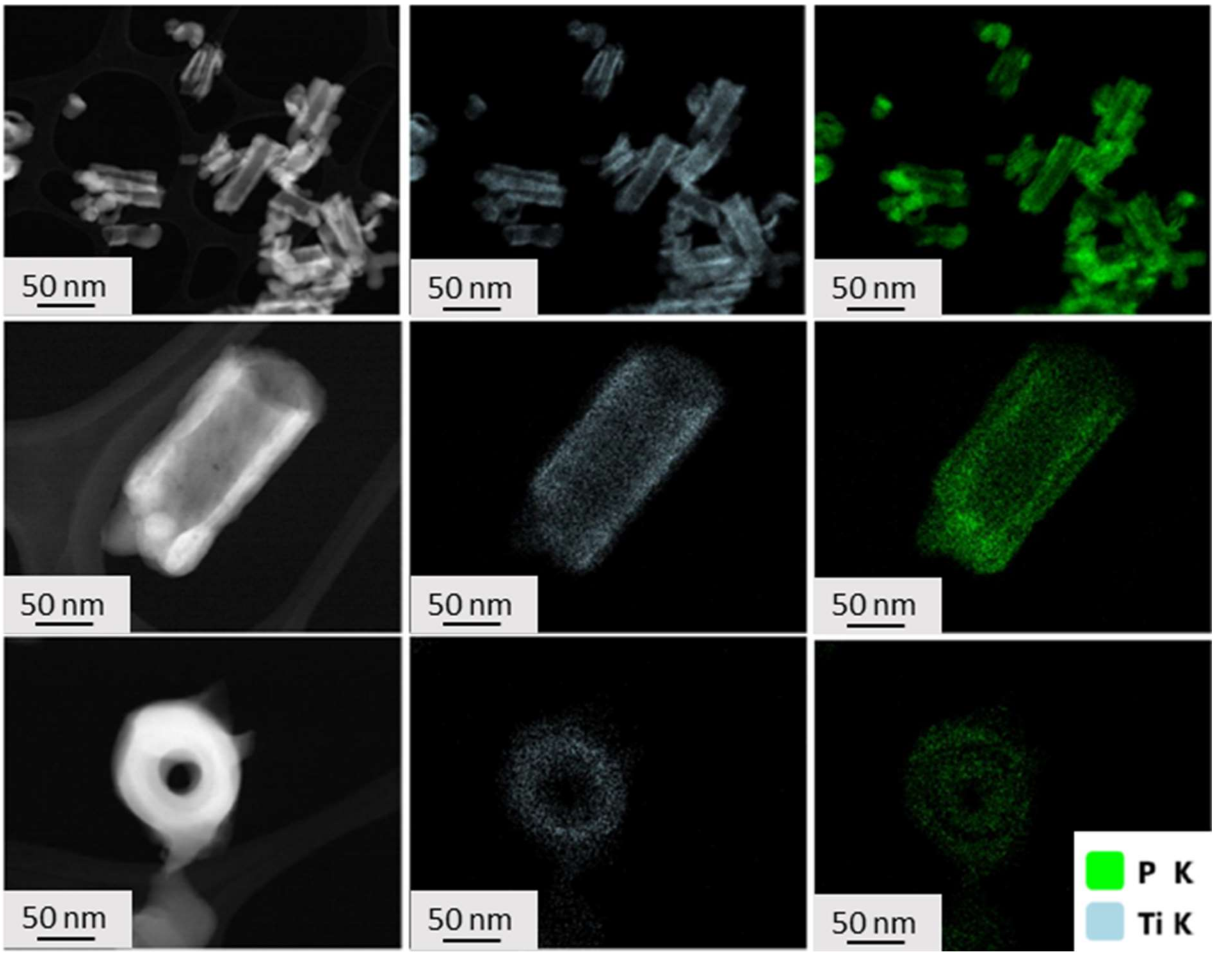

Figure 28. EDS mapping of a separated fragment of BP-modified TiO_2 NTs.

The main goal of the studies presented in this section was to establish, if the CVT technique is eligible for surface modification of TiO_2 NTs. The electrochemical performance and photoactivity of BP-modified TiO_2 NTs has shown very little improvement over pristine titania nanotubes probably due to the rapid oxidation of thin BP layer [191]. Nevertheless, the summary of the electrochemical studies is presented in figure 37. together with b-AsP-modified TiO_2 NTs (part 5.6).

5.5 Black arsenic-phosphorus nanoribbons

Black phosphorus nanoribbons have drawn a lot of attention, due to their extraordinary properties and tunable bandgap . However, as previously mentioned in chapter 2, phosphorene nanostructures oxidize easily [239], which holds back their application in devices on a broader scale. Nonetheless, one possible way to overcome these difficulties is the modification of the phosphorene structure by substituting some of the P atoms for As atoms. This new b-AsP structure is proven to be far more stable in ambient conditions [240,241], also narrowing the bandgap depending on the atomic composition of the structure, moving the optical activity of a single layer into near-infrared [242].

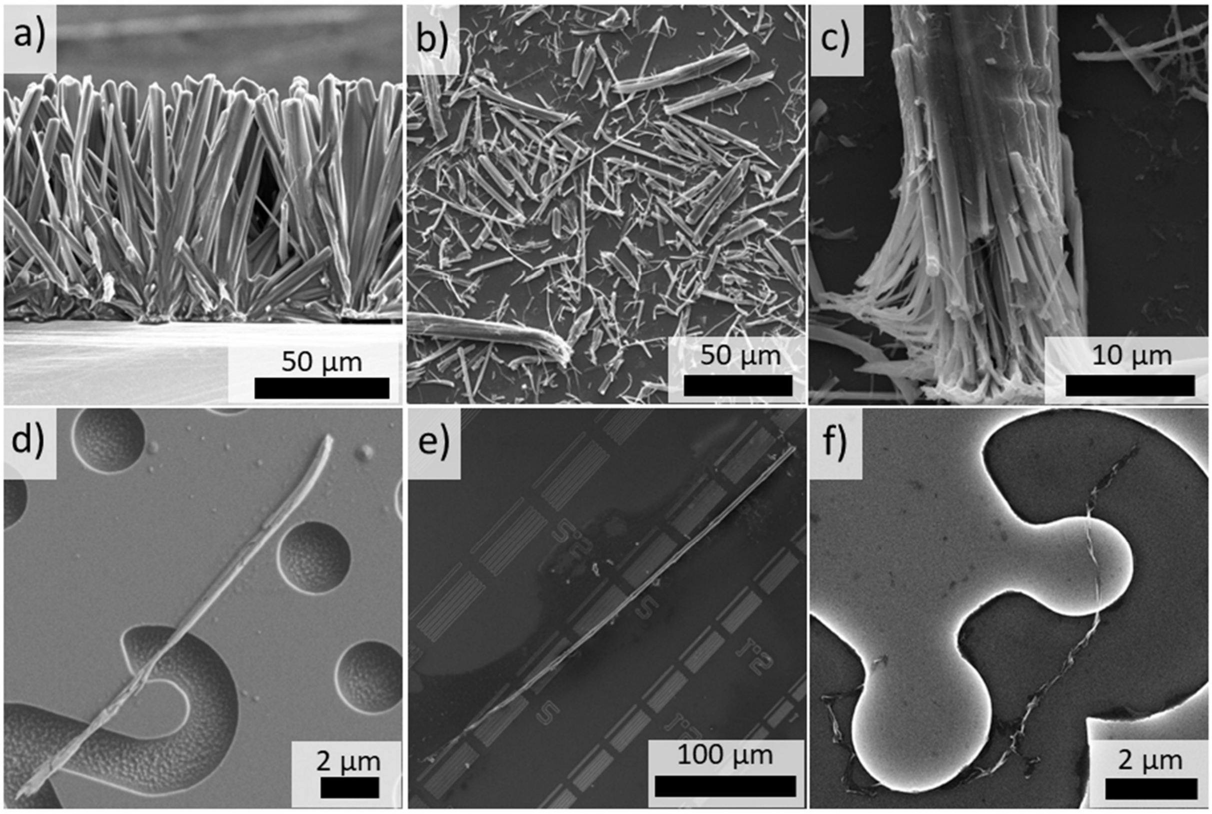

Figure 29. SEM images of a) b-AsP columns on silicon substrate, b) single b-AsP columns, c) initially exfoliated b-AsP columns and nanoribbons; surface morphology of a separated, initially exfoliated b-AsP column synthesized using d) 10, e) 20 and f) 50% of As to P atomic mass ratio.

In this study, the morphology of b-AsP ribbons and columns was obtained using Zeiss Sigma scanning electron microscope The chemical composition was examined using a Bruker XFlash 6|10 energy dispersive X-ray spectrometer. Single BP ribbon image and its dimensions were acquired using an NSV-VEECO-D3100 atomic force microscope operated in tapping mode under ambient conditions and analyzed using Gwyddion open source software [210]. The Raman measurements were performed using λ = 632.8 nm (1.96 eV) He–Ne laser. The signal was collected with a microscope objective, sent through a 1 m monochromator, and detected by using a liquid nitrogen-cooled charge-coupled device (CCD) camera. The excitation power focused on the sample was kept fixed at 1 mW during all measurements to avoid local heating. The temperature-dependent Raman measurements were performed by placing the sample on a cold finger in a continuous flow cryostat. The temperature was changed from 5 to 300 K in steps of 25 K with the signal collected from the sample after the stabilization of the temperature. The angle-dependent Raman spectra were collected in range from 0 to 360°, with a step of 10° and presented in form of angle versus intensity graph for each specific BP vibrational mode using OriginLab [232]. The air stability of BP and b-AsP nanoribbons was investigated using Raman spectra collected each day for a total time of 4 days for BP and 17 days for b-AsP structures.

Here, the CVT technique was applied to fabricate b-AsP nanoribbons with various concentrations of As. The fabrication procedure is similar to the approach used to form the BP nanoribbons. The reagent, of red phosphorus, Sn, SnI_4, and gray arsenic together with silicon substrates were placed in an evacuated quartz ampule. Similarly to the BP nanoribbons, after the CVT process, a regular layer of b-AsP columns was fabricated (Fig. 29a). Using ultrasonication in DMF, the b-AsP columns layer could be broken down to single columns (Fig. 29b) and eventually b-AsP nanoribbons (Fig. 29c). As is showed below, some of the b-AsP nanoribbons are not fully exfoliated, but they are of similar length and various widths, which suggests the possibility of obtaining b-AsP nanoribbons of specific dimensions and designing their electronic properties for suitable applications [93].

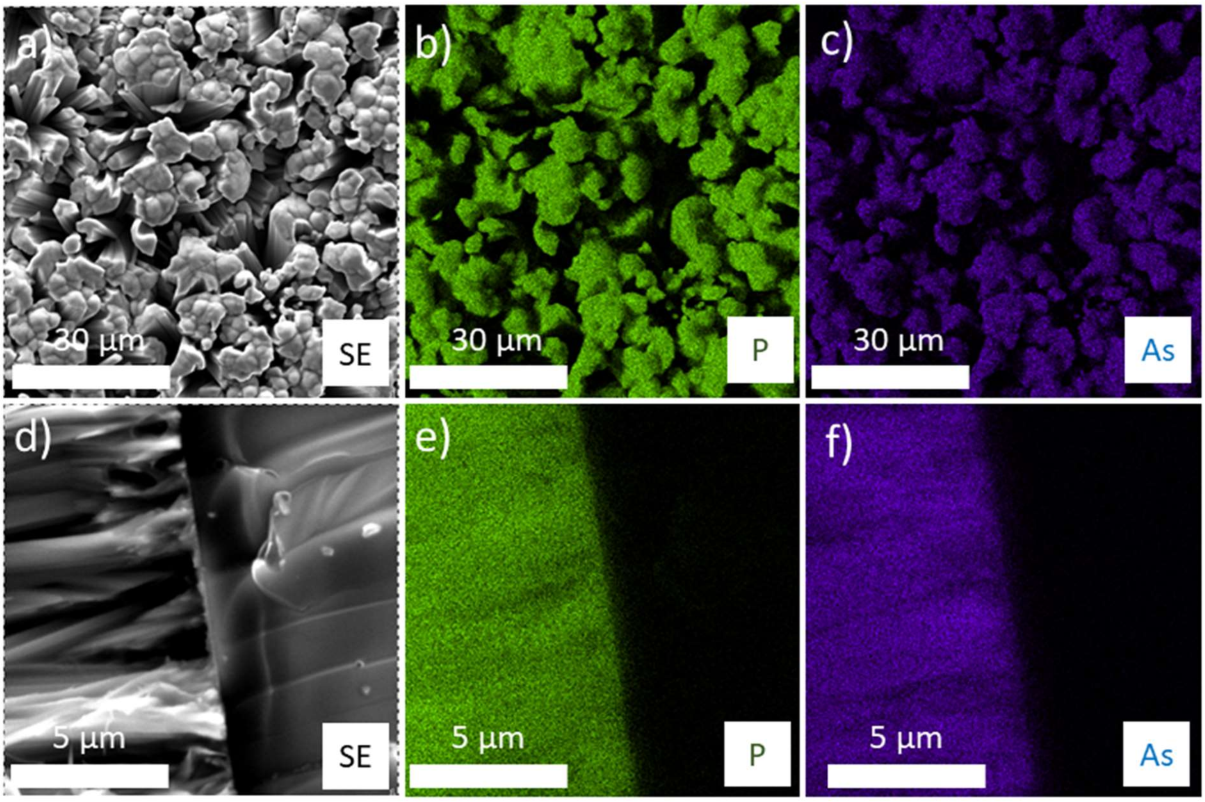

Figure 30. a–c) top and d–f) side view of b-AsP columns on silicon substrate; a,d) SEM images, b,e) phosphorus and c,f) arsenic EDS mapping.

The dimensions of the black arsenic-phosphorus nanoribbons are not the only factor influencing their properties. As previously mentioned, the arsenic concentration will also affect the bandgap width of the nanostructures. Three samples were prepared based on the red phosphorus to gray arsenic atomic mass ratio during the CVT process, which are b-$As_{0.1}P_{0.9}$, b-$As_{0.2}P_{0.8}$, and b-$As_{0.5}P_{0.5}$ (Fig. 29d,e,f, respectively). The b-AsP nanoribbons presented in Figs. 29d and 29e exhibit a similar surface morphology to monocrystalline BP nanoribbons, whereas increasing the As concentration to 50% of atomic mass seems to modify the appearance of the nanoribbons, concluding in twisted and possibly agglomerated nanostructures, as demonstrated in Fig. 29f, which is why the b-$As_{0.5}P_{0.5}$ was not further investigated. The difficulty in exfoliating b-AsP with a high arsenic content might indicate an enhanced interlayer interaction for the material. This phenomenon can be a viable example of the strength of the interlayer van der Walls interactions in layered materials, as previously reported by Liu et al. [243].

EDS studies were performed to establish if As atoms are present across the entire length of the nanoribbons. The studies revealed that both As, marked in purple, and P atoms, marked in green, are present at the top of the column layer (Fig. 30a,b,c). A cross-section analysis (Fig. 30d,e,f) reveled both elements to be visible at the root of the structure, further confirming that the b-AsP columns contain P and As across the whole structure.

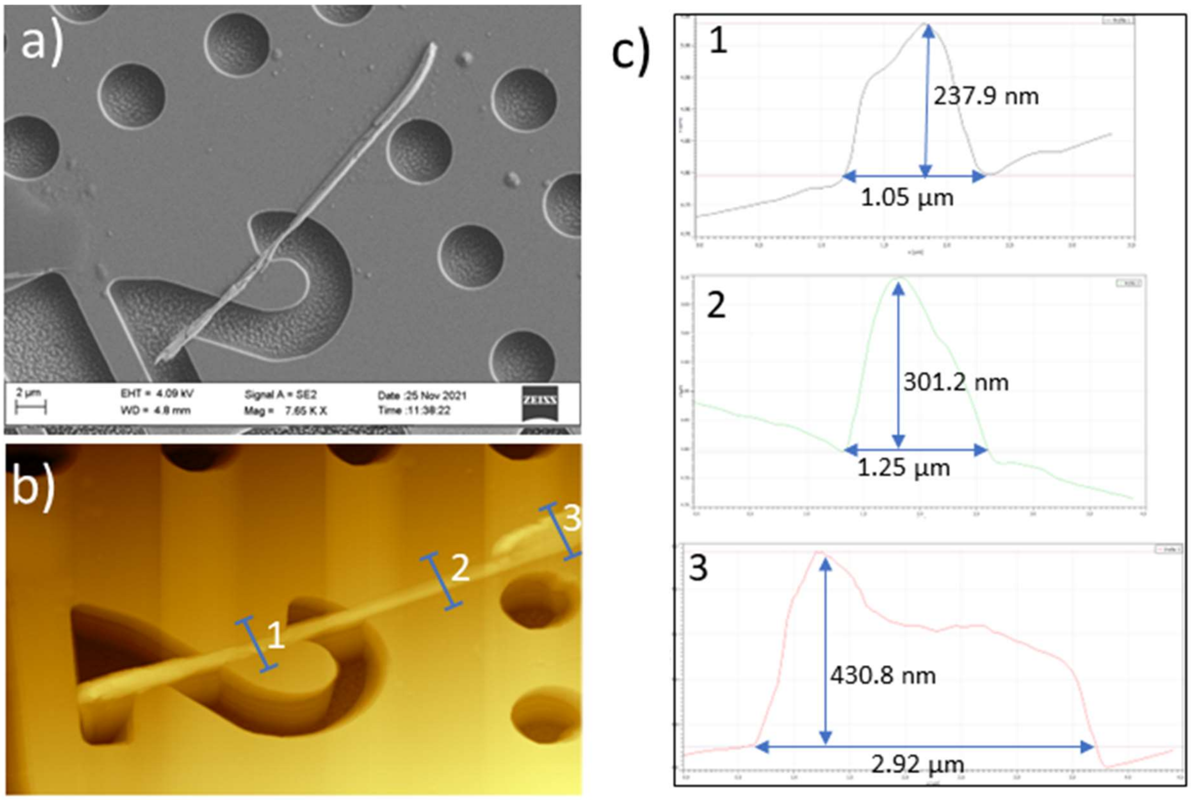

Figure 31. Surface morphology of a single b-AsP column collected with a) SEM, b) AFM and its width and height calculated at three points along the structure.

The following studies were performed on a single b-$As_{0.1}P_{0.9}$ ribbon in order to investigate if incorporating As into BP structure in weight concentration of as low as 10% can influence the air-stability of the material and to provide preliminary analysis of first, at that time, report on experimentally fabricated b-AsP ribbons. SEM, AFM, and EDX analyses were performed for a single b-$As_{0.1}P_{0.9}$ nanoribbon, as presented in Figs. 31 and 32. Fig. 31a) presents the SEM images of a single b-$As_{0.1}P_{0.9}$ nanoribbon with dimensions of around 1–3 µm in width and more than 40 µm in length. The AFM studies (Fig. 27b–c) shows the nanoribbon to have an increasing dimension toward one end of the nanoribbon, which could be associated with the b-AsP columns being slightly wider at the base of the structure. Nonetheless, the thickness measurements reveal the nanoribbon to be 237.9 nm at the thinnest and 430.8 nm at its thickest part. Shi et al. reported that the interplanar spacing in b-AsP is larger than in BP of indicating that the addition of As atoms may increase in lattice constant from 0,55 to 0,58 nm for b-$As_{0,83}P_{0,17}$ [244].

Using the same method of BP structure thickness calculation, as previously presented for BP nanoribbons (section 5.3) and assuming linear increase of the interplanar spacing with As concentration, the thickness is corresponding to around 423 and 767 of b-$As_{0.1}P_{0.9}$ with 0,56 nm spacing between layers.

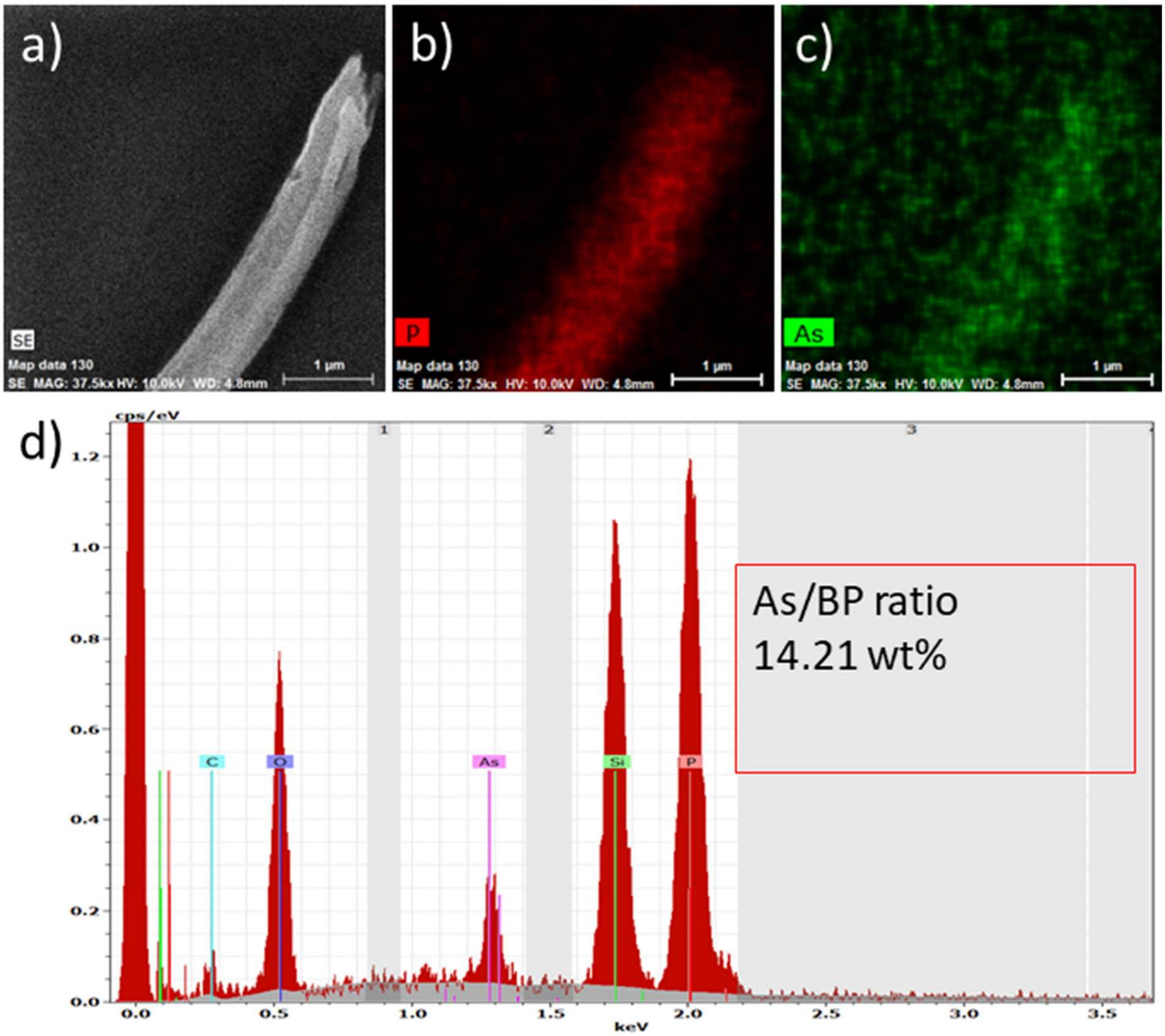

Figure 32. a) Surface morphology, b) phosphorus and c) As EDS mapping, d) EDS signal collected for a single b-AsP fabricated using 10% As/P atomic mass ratio.

The EDX measurements (Fig. 32) show the b-$As_{0.1}P_{0.9}$ ribbon to contains As and P atoms with an As/P weight ratio of 14.21% and taking into account the error of the measurement, this is close to the intended composition.

The orientation of the direction along the b-$As_{0.1}P_{0.9}$ nanoribbon, and its optical properties were investigated using Raman spectroscopy. Figs. 33a and 33b show the Raman spectra recorded for the nanoribbon at 6 K and 300 K, respectively. According to theoretical studies and the results published by other scientific groups, the vibrational Raman A^1_g, B_{2g}, and A^2_g modes of As are indistinguishable from the Raman spectra for a low As concentration, such as b-$As_{0.1}P_{0.9}$ [240,245,246]. Moreover, there is a visible separation of peaks for the phosphorus A^1_g, B_{2g}, and A^2_g modes, which is further developed at cryogenic temperatures. The high noise level of Raman spectra can be associated with a low thickness of the investigated structures and low excitation power of the laser used for these measurements [48,247].

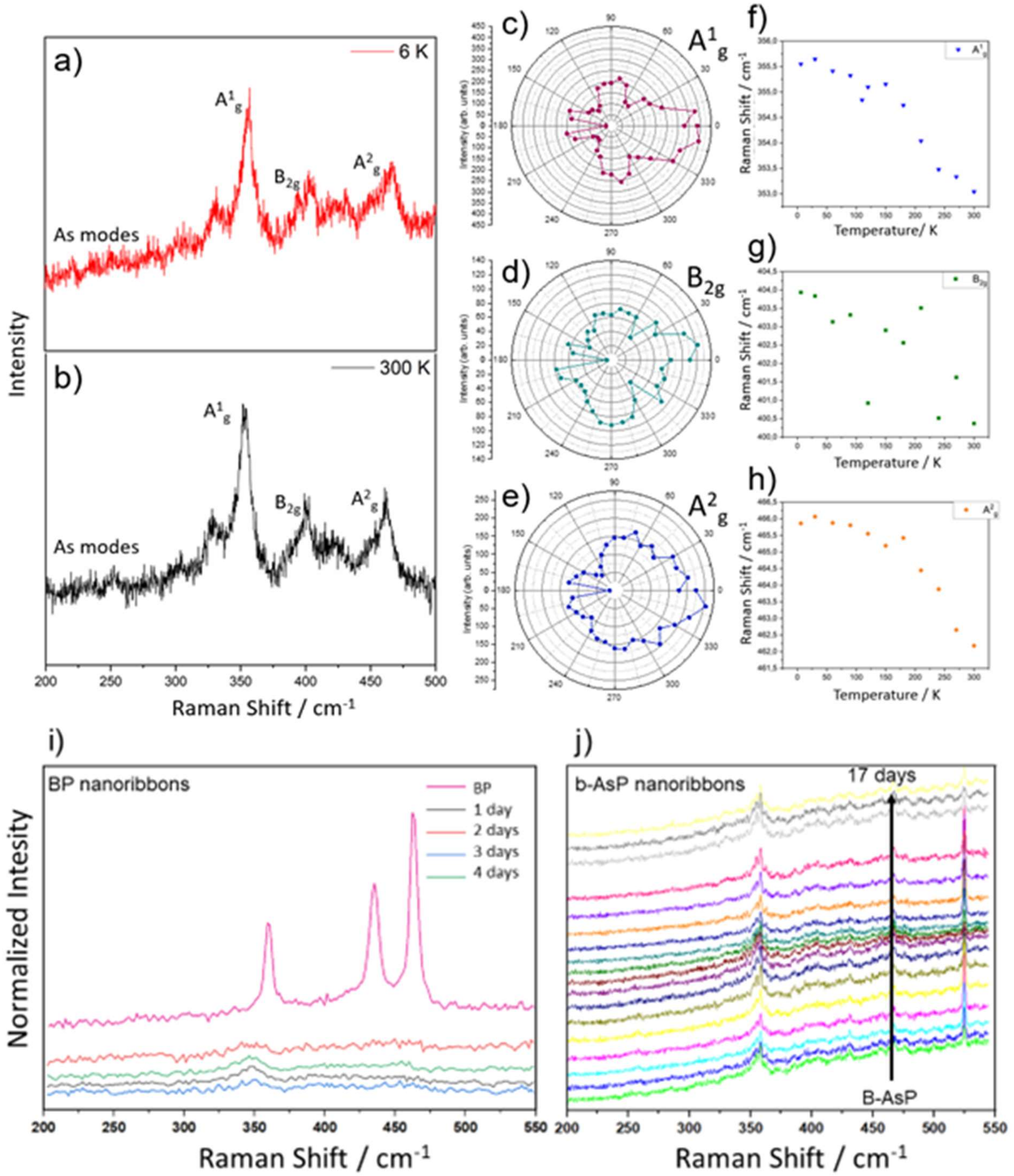

Figure 33. Raman studies of a single b-$As_{0.1}P_{0.9}$ ribbon; Raman spectra collected in a) 6 and b) 300 K, angle-dependent and temperature-dependent Raman spectra of c,f) A^1_g, d,g) B_{2g}, e,h) A^2_g BP vibrational modes. Raman spectra of i) BP and j) b-AsP nanoribbons collected in 1 day interval.

Following the identification of vibrational modes of the ribbon, polarization (Fig. 33c–e) and temperature (Fig. 33f–g) dependence measurement of A^1_g, B_{2g}, and A^2_g black phosphorus Raman modes were conducted. The linearly polarized Raman measurement showed the phosphorus Raman modes to act similarly, as for BP nanoribbons, with A^1_g and A^2_g corresponding to P atoms oscillating in the zigzag and out-of-plane directions [187]. Nonetheless, the B_{2g} mode exhibits an unusual behavior, with the periodical maxima being in similar positions to those of the A^1_g and A^2_g modes. This effect may be caused by structural changes when incorporating As atoms to the phosphorene structure [248]. The temperature-dependent measurement reveals a gradual blue shift in the positions of all vibrational modes. The A^1_g, B_{2g}, and A^2_g modes display a rapid blue shift when lowering the temperature of the sample from 300 K and stabilizing the position shift of the modes after reaching 100 K, which may suggest a weakening of the tensile stress in the nanoribbon structure [249].

Air-stability is a key factor, decisive if novel 2D semiconductors can be introduced into present and developing technological solutions [250–252]. As previously mentioned, thin layer of BP oxidize easily upon contact with air or water. However, as described in section 2.3.4 of this dissertation, there are methods to prevent this process, by creating a physical barrier between the sample and the environment, including various surface modifications and coatings. Nonetheless, these methods of achieving air stability in BP crosses out its applications for surface interactions, such as sensors and catalysis [99]. Raman spectra recorded for BP (Fig. 33i) and b-AsP (Fig. 33j) nanoribbons reveal that incorporating 10% of weight concentration of As into BP can increase air-stability of the material from less than 24 hours for BP to at least 2 weeks for b-$As_{0.1}P_{0.9}$, after which the intensity starts to decrease slightly (Fig. 33j). The vast improvement in air-stability of b-AsP in comparison to BP thin layers was also reported by other scientific groups [105,240,253,254].

Here, a time-efficient and reliable method for the development of b-AsP nanoribbons has been proposed. The CVT approach enables the controllable of b-AsP columns with a wide range of sizes, which can be further exfoliated to b-AsP nanoribbons of designated dimensions. The b-AsP exhibits a regular chemical composition across the entire length of the ribbons. Introducing As atoms to the phosphorene structure slightly influences the optical properties of the material. However, Raman studies presented for BP the b-AsP nanoribbons show a significant improvement in air-stability, which could be convincing enough to substitute phosphorene with arsenic-modified phosphorene nanostructures in electronic applications, such as b-AsP FETs [243,255,256], proving **hypothesis II** of this dissertation.

5.6 Black arsenic-phosphorus-modified TiO_2 nanotubes

Black arsenic-phosphorus compound materials play a vital role in a range of applications due to their uncommon physical, electrochemical, and optical properties, and flexible architectures. Here, b-AsP-modified titania nanotubes (b-AsP TiO_2 NTs) were synthesized by a gas phase transport method (Fig. 34). SEM images and EDS mapping were used to investigate surface morphology and chemical composition of modified nanotubes. Raman spectra reveal the synthesized structures to have high crystallinity showing characteristic modes for both b-AsP compound [257] and TiO_2 NTs [258].

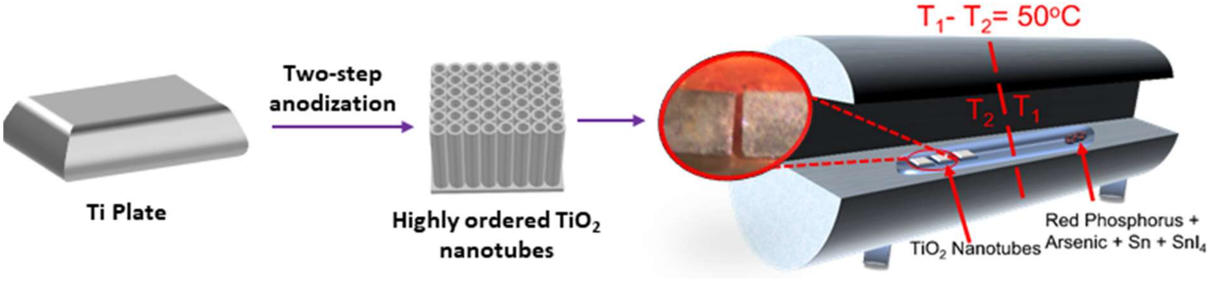

Figure 34. Graphical representation of the fabrication and modification process of TiO_2 nanotubes.

In this study, Raman spectra and SEM images were collected with the same equipment as in section 5.4 for BP-modified TiO_2 nanotubes (Renishaw inVia Raman Microscope and FEI Nova 600 SEM) and analyzed using local maximum peak finding algorithm in OriginLab software [232]. The photo-electrochemical and electrochemical measurements were carried out in a three-electrode arrangement with Pt mesh as a counter electrode, Ag/AgCl/0.1 M KCl as a reference electrode and pristine, b-AsP- and BP-modified TiO_2 NTs as a working electrode. The CV scan rate was 50 mV/s and the potential range from -1.2 to +1.0 V was applied. Transient photocurrent response were registered at +0.5 V vs. Ag/AgCl/0.1 M KCl with pristine and b-AsP-modified TiO_2 nanotubes serving as a working electrode.

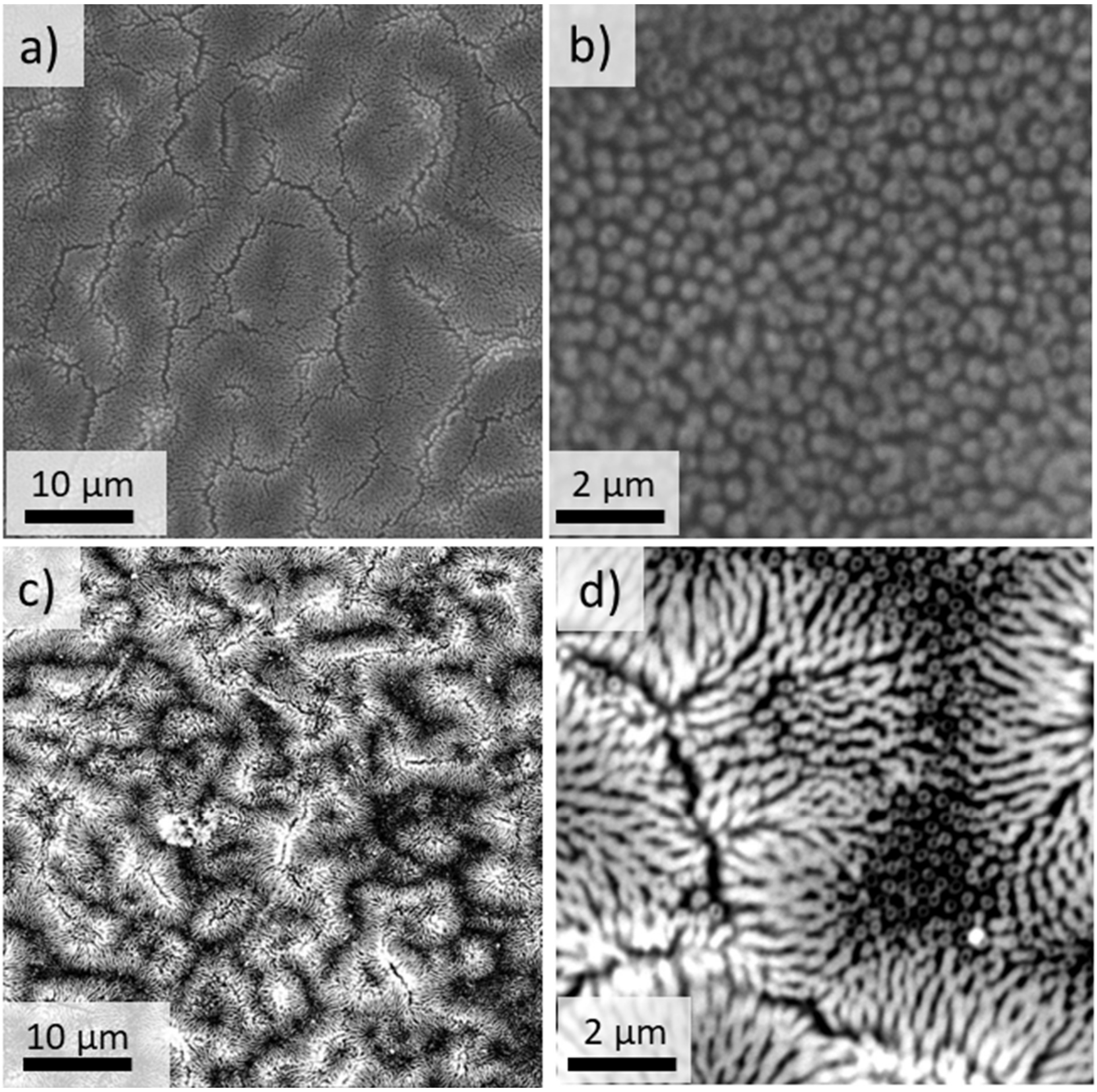

Figure 35. Surface morphology of a,b) pristine and c,d) b-AsP TiO_2 nanotubes.

The fabrication process is similar to the surface modification of TiO_2 NTs with pristine BP using the chemical vapor transport process, which is described in previous chapters. The phosphorus-to-arsenic ratio can vary depending on the amount of used precursors (b-$As_{0.1}P_{0.9}$ for this experiment). Highly ordered TiO_2 nanotubes were placed in an evacuated down to 10^{-5} Torr quartz ampule with red phosphorus (300 mg), arsenic (80 mg), Sn (10 mg), and SnI_4 (5 mg). At the end of the process, with the TiO_2 NTs reaching 21°C, a localized layer of b-AsP was found to have formed on the substrate surface (Fig. 35,36).

Scanning electron microscopy was applied to investigate the surface morphology and homogeneity of the fabricated structures (Fig. 35). The surface of b-AsP-modified TiO_2 NTs looks different than in case of BP-modification. The cracks in nanotubes layer aren't filled with b-AsP but seem further enhanced with the modification having a localized character (Fig. 35c) instead of forming a homogenous layer like it was reported for BP TiO_2 NTs (Fig. 25c). SEM images obtained with a higher magnification also indicates that the surface of nanotubes have been selectively modified leaving some nanotubes intact by the modification process, which can be further investigated by EDS mapping.

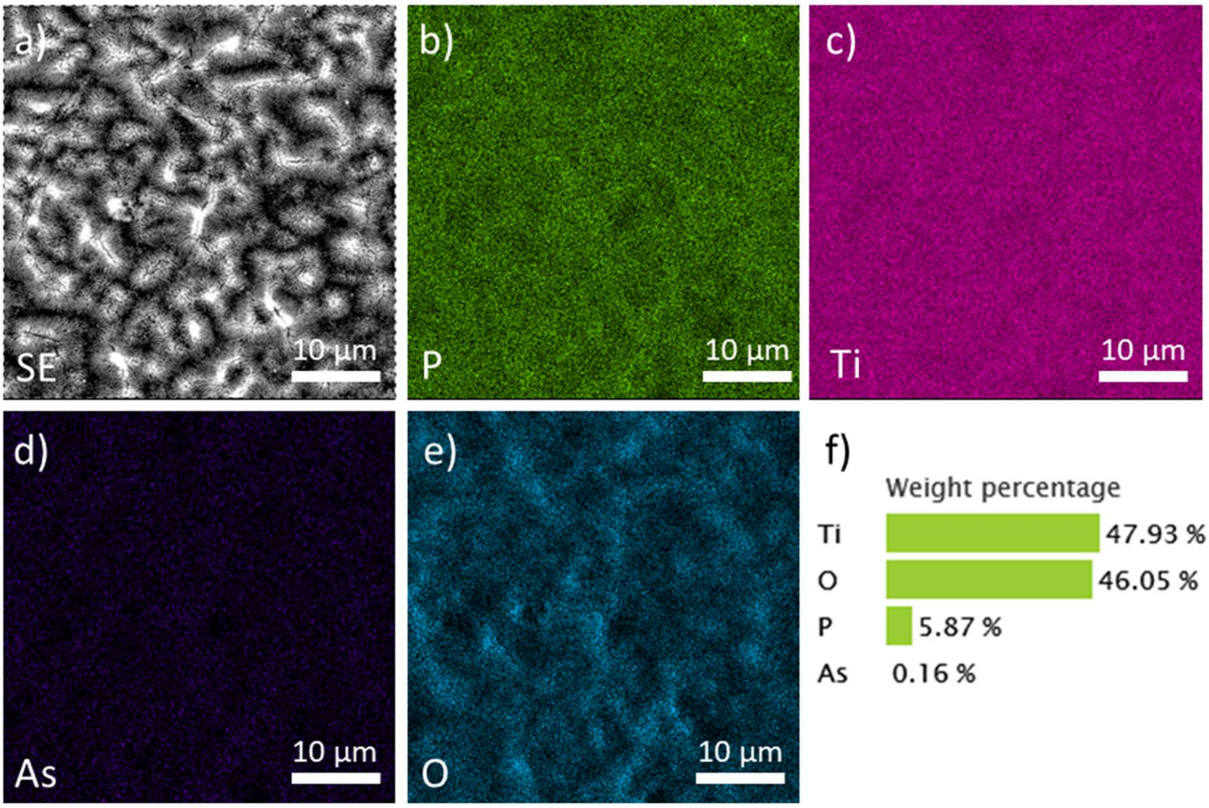

Figure 36. a) surface morphology, b-e) EDS mapping and f) chemical composition) b-AsP TiO_2 nanotubes.

Following SEM analysis of the modified samples, the chemical composition of the b-AsP TiO_2 NTs was investigated by Energy-dispersive X-ray spectroscopy. Contradictory to the results of SEM analysis, the surface of the titania nanotubes is regularly covered with b-AsP (Fig. 36) with a few localized cavities of P. The darker spots on EDS map for phosphorus is however consistent with local lower concentration of titanium, thus can be attributed to imperfections in beam focusing due possible elevation of cracks above titania surface. It is possible that b-AsP creates a homogeneous layer on the inside and outside of the nanotubes, similarly to how it was demonstrated with the TEM results of pristine BP modification, however additional studies need to be conducted. Energy-dispersive X-ray spectroscopy (Fig. 36f) confirms the modified nanotubes to contain all of the expected elements, which are: titanium, oxygen, phosphorus and arsenic.

In order to investigate the structural properties, Raman spectroscopy of bulk b-AsP (orange), pristine (blue) and b-AsP-modified TiO_2 nanotubes (black) was conducted (Fig. 37). The modified nanotubes have high crystallinity and display characteristic A^1_g, B^2_g, and A^2_g modes for both black phosphorus and arsenic and $E_{g(1)}$, $E_{g(2)}$, B_{1g}, A_{1g}, and $E_{g(3)}$ of anatase TiO_2 nanotubes. Raman spectra of b-AsP modified nanotubes is difficult to analyze due to the fact that some of the TiO_2 and BP and As modes overlap slightly. Nonetheless, using a peak finding algorithm of OriginLab [232], most of the visible peaks can be attributed to the appropriate vibrational modes of anatase, arsenic and black phosphorus, proving the successful modification with b-AsP (Table 3). Moreover, three identified peak can be found in the modified titania NTs spectrum, which are not present in reference b-AsP and TiO_2 NTs. Their position (200,29 cm^{-1}, 221,68 cm^{-1} and 221,98 cm^{-1}) is however almost identical to black arsenic B_{2g} (201 cm^{-1}) and twin A^2_g+B_{3g} (223 cm^{-1}) vibrational modes reported by Antonatos et al. and were identified as such [259]. The general knowledge of black arsenic-phosphorus has recently started to expand with only a few reports of utilizing it for modification and doping purposes [244,260] and a deeper analysis of Raman spectra would require computational Raman simulation studies in order to compare the experiment with theoretical behavior of such structure.

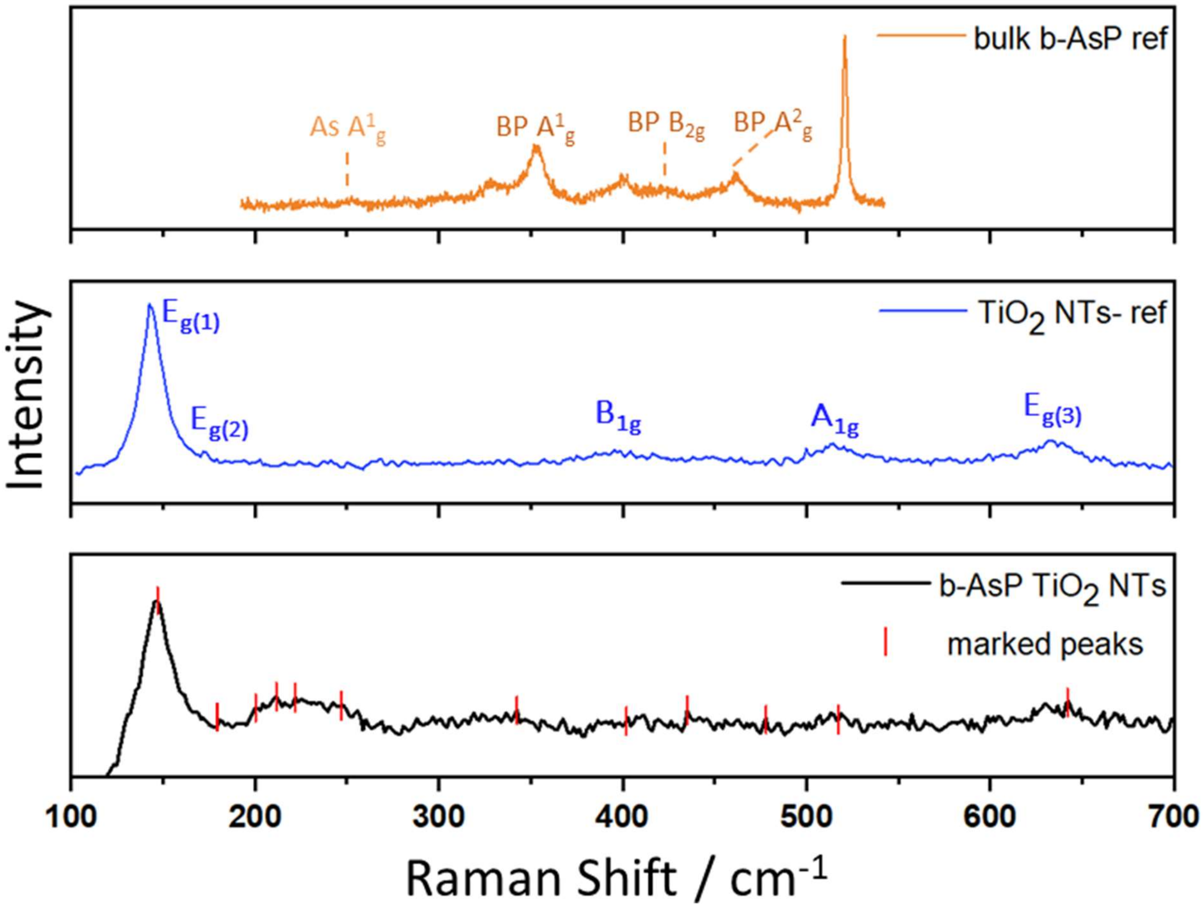

Figure 37. a) Raman spectra of pristine and b-AsP-modified TiO_2 nanotubes, b) chemical composition of fabricated b-AsP TiO_2 nanotubes.

Table 3. Marked peak position of Raman spectra recorded for b-AsP-modified TiO_2 NTs, reference TiO_2 NTs and reference bulk BP and their attribution to corresponding vibrational modes.

Fitted Modes Maxima / cm^{-1}			**Modes Identified as:**
B-AsP-TiO_2 NTs	**TiO_2 NTs ref**	**Bulk b-AsP ref**	
146,96	**142,13**	**-------**	**$E_{g(1)}$**
181,44	**171,61**	**-------**	**$E_{g(2)}$**
200,29	**-------**	**-------**	**As B_{2g}**
221,68	**-------**	**-------**	**As A^2_g**
221,98	**-------**	**-------**	**As B_{3g}**
246,98	**-------**	**252,25**	**As A^1_g**
342,59	**-------**	**353,91**	**BP A^1_g**
402,01	**391,47**	**-------**	**B_{1g}**
435,25	**-------**	**422,26**	**BP B_{2g}**
478,11	**-------**	**461,17**	**BP A^2_g**
517,32	**516,79**	**-------**	**A_{1g}**
642,03	**635,97**	**-------**	**$E_{g(3)}$**

The electrochemical activity was investigated cyclic voltammetry of pristine (TiO_2 NTs-ref) (red), BP- (black) and b-AsP-(multiple colors) modified titania NTs (Fig. 38). The measurement were performed for 5 different b-AsP-modified samples, each cycled 3 times, to ensure the repeatability of the modification process. It can be noticed that the b-AsP-modified electrodes exhibit much higher current values, showing an increase in electrochemical activity in comparison to pristine and BP-modified titania nanotubes. Moreover, the b-AsP-modified NTs exhibit a reversible redox behavior in the cathodic range, showing high stability despite 3 cycles. In the anodic range upon subsequent cycles, the activity is going down. Furthermore, BP-modified nanotubes show a slight increase in current density of the anodic range in the first cycle, which then falls rapidly to values achieved by pristine titania NTs. This behavior is not observed for b-AsP modification despite 3 recorded cycles and suggest a rapid oxidation of BP in the aqueous solution pointing out a higher stability of b-AsP in comparison to BP modification upon contact with water.

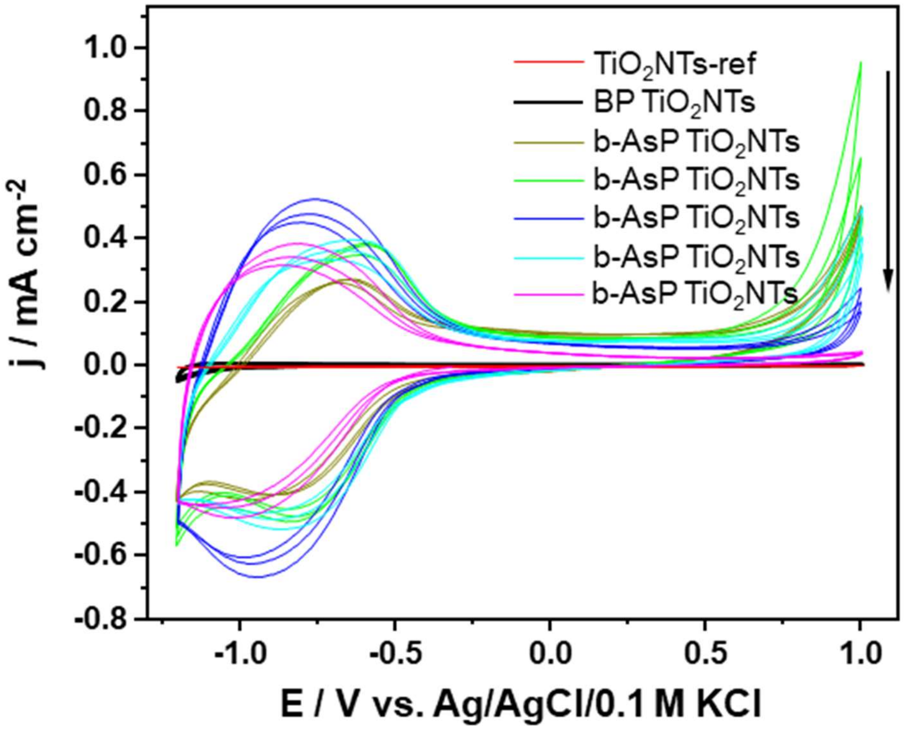

Figure 38. Cyclic voltammetry of pristine, BP- and b-AsP-modified TiO_2 NTs, in 0.5 M solution of Na_2SO_4.

The photocurrent response for pristine (red) and b-AsP-modified (orange) TiO_2 nanotubes was recorded by on and off cycle registered under UV-Vis radiation (Fig. 39). The obtained chronoamperometry curves exhibit rapid changes in current density equal to ΔJ=0,24 μA/cm^2 for pristine and ΔJ=3,78 μA/cm^2 for b-AsP-modified TiO_2 NTs when the irradiation was switched off and on (Fig. 39). The chronoamperometry responses for TiO_2 NTs modified with b-AsP exhibit improved photoactivity showing more than 15 times higher current density compared to unmodified nanotubes.

Here, a novel method for the surface modification of nanoribbons with b-AsP has been proposed. The CVT approach enables the controllable phosphorus-to-arsenic ratio, which can further enhance photoelectrochemical and electrochemical responses of modified nanotubes. Surface morphology of AsP-modified TiO_2 NTs vastly varies from the one presented for BP modification with numerous cracks and holes. Nevertheless, the EDS mapping and Raman spectra confirm the modification process to be successful. Moreover, cyclic voltammetry measurements of b-AsP modified nanotubes show a significant increase in electrochemical activity in comparison to BP-modified and pristine titania NTs proving **hypothesis III**. Furthermore, a lack of rapid decrease in current density for b-AsP modified NTs show a superior water-stability in comparison to BP modifications, proves **hypothesis II**. Also, the chronoamperometry responses for TiO_2 NTs modified with b-AsP show improvement of over 15 times in current density compared to unmodified nanotubes, once again proving **hypothesis III**.

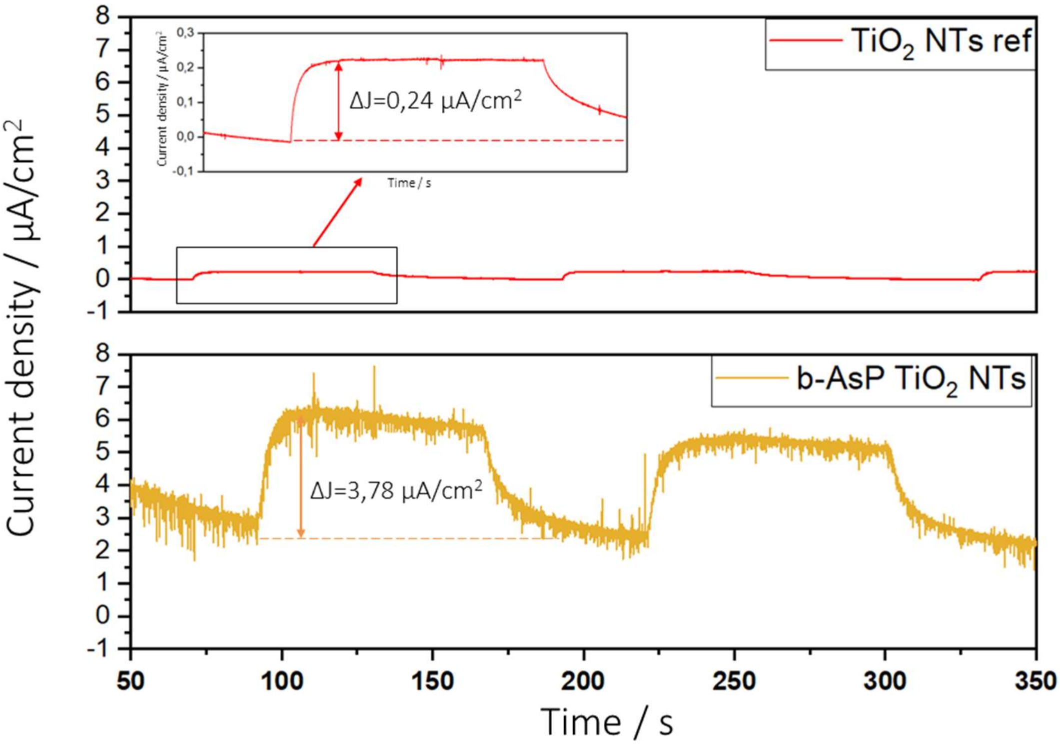

Figure 39. Transient photocurrent response of pristine (red) and b-AsP-modified (orange) TiO_2 nanotubes registered at +0.5 V vs. Ag/AgCl/0.1 M KCl.

5.7 Black phosphorus and black arsenic-phosphorus-modified electrode materials

The studies presented below show the results the CVT-based BP and b-AsP modification of other materials, such as of interdigitated gold array and boron-doped diamond electrodes. The experiments provide preliminary results such as the surface morphology and the chemical composition of gold array electrodes. In case of BDD, in addition to SEM and EDS analysis, electrochemical and structural properties were investigated. Ordered arrays electrodes have been widely recognized for their paramount properties in sensing applications, such as electrochemical [261], optical [262,263], and field-effect transistor platforms [264,265], making it an interesting choice for surface modifications.

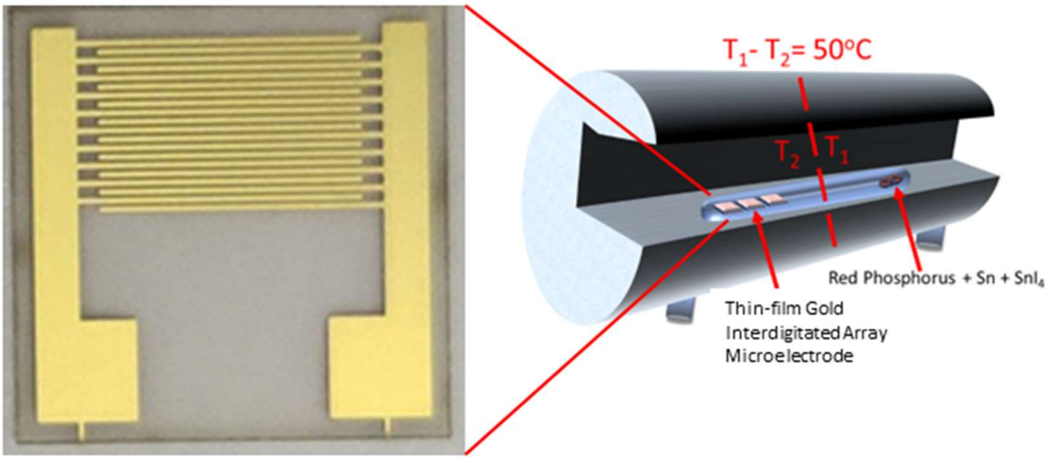

Figure 40. Modification process of interdigitated array gold electrodes with BP and b-AsP.

Boron-doped diamond is known for its high electrochemical and physical stability due to the sp^3 hybridization featuring in its structure [266]. Moreover, exceptional electrochemical characteristics like the possibility of working in a wide window in aqueous solutions and low background current made BDD electrodes widely used as electroanalytical sensors [267]. Nevertheless, the BDD applications is hampered on a wider scale due to time-consuming pretreatment increasing the time of analysis or lack of signal repeatability if overlooked [268]. These characteristics, highly reproducible structures and surface adequate for using as a matrix for the growth of other materials make BDD electrodes a potential substrate for modification [269,270].

In this study, surface morphology of the samples was investigated using FEI Nova 600 SEM equipped with light element EDS X-ray detector for chemical composition studies of modified electrode materials. Raman spectra were collected on a Renishaw inVia Raman Microscope, equipped with a 532 nm emission line Nd:YAG laser operating at 10 mW. Electrochemical studies of modified BDD electrodes were performed in a three-electrode arrangement with Pt mesh as a counter electrode, Ag/AgCl as a reference electrode 1 M KNO_3.

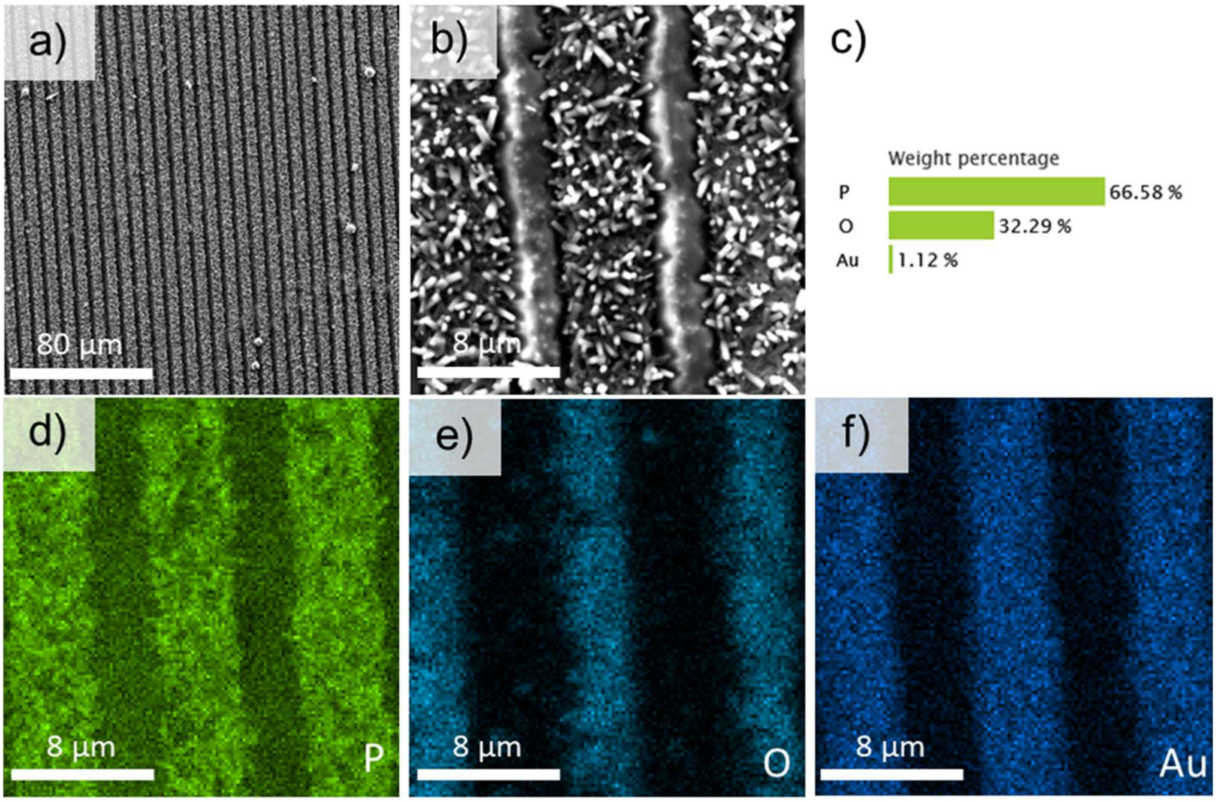

Figure 41.a,b) Surface morphology c) chemical composition and d-f) EDS mapping of BP-modified interdigitated array gold electrodes.

In this study, a commercially available interdigitated array gold electrode (Fig. 40) was utilized as a substrate in the CVT process for its surface modification with BP and b-AsP. The CVT technique was performed similarly to the process previously described in detail (section 5.1). The SEM images reveal that both BP (Fig. 41) and b-AsP (Fig. 42) form needle-like structures on top of Au arrays. The EDS mapping of BP-modified electrodes (Fig. 41c), reveal that phosphorus is growing mostly on top of gold, recreating its pattern with numerous phosphorus columns of submicron dimensions. The chemical composition reveal the BP structures to have oxidized heavily by the time of the measurement.

Nevertheless, recreating an air-stable and similarly shaped BP-based structure would be highly beneficial for sensing purposes, due to a massive increase in surface-to-volume ratio and active sites number.

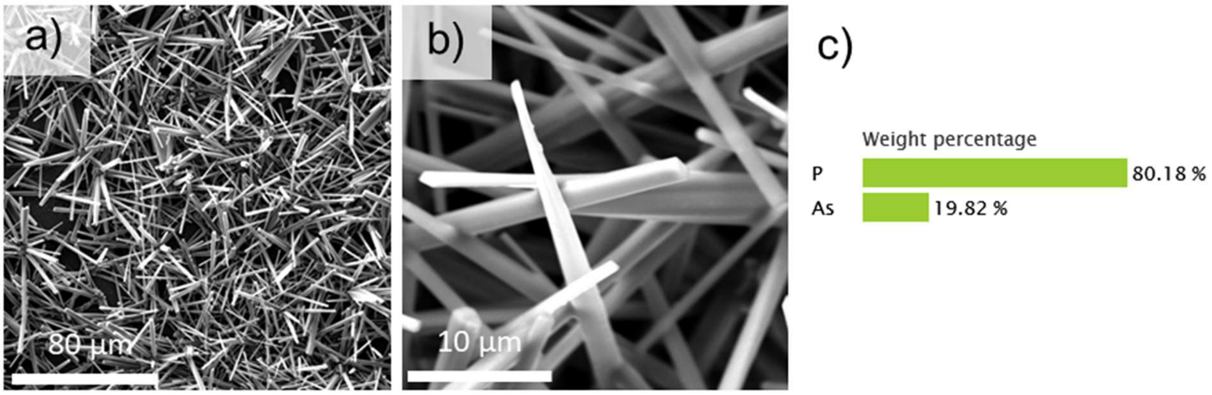

Figure 42.a,b) Surface morphology and c) chemical composition of b-AsP-modified BDD electrodes.

The b-AsP-modified gold array electrode shows a slightly different structure (Fig. 42a). The b-AsP columns are not localized on gold array but are regularly spread across the whole electrode surface. The b-AsP grown columns are also much longer and thicker (at least one order of magnitude) in comparison to the ones grown in phosphorus modification. SEM images obtained with a higher magnification (Fig. 42b), reveal the b-AsP columns to have sharper, well defined edges, which as it was demonstrated in section 5.1, points to the high crystallinity of the columns. The chemical composition of these structures reveal that the b-AsP columns do not oxidize as easily as in case in phosphorus modification, which indicates air-stability of these structures, validating **hypothesis II**. The full coverage of Au electrodes with b-AsP structures undoubtedly excludes its application in FETs, but can still be utilized for gas and electroanalytical sensors. Black phosphorus is currently under investigation by various scientific groups for its sensing capabilities. Due to their enormous surface-to-volume ratio, layers of BP and b-AsP needle structures grown on electrode materials could be easily applied for such a purpose, and further investigation of these samples will be conducted in the future.

The boron-doped diamond was synthesized in an MW PA CVD (Seki Technotron AX5200S) system using sonication of p-type Si wafers in a nanodiamond suspension. The Si substrates were dried under a stream of nitrogen and kept at 1100°C during the deposition. The plasma microwave power was kept at 1300 W (2.45 GHz Seki Astex 6400) and the gas mixture ratio was a 1% molar ratio of Ch_4-H_2. The substrates were doped with diborane (B_2H_6) dopant precursor and the [B]/[C] ratio in plasma was 10,000 ppm. The growth time of the polycrystalline BDD layer was 180 min with a 5.56 nm/min growth rate, which provides a thickness of the deposited film of ca. 1 µm [271].

The BP and b-AsP modification was, as previously mentioned, carried out using the CVT technique, with a BDD substrate used instead of Si wafers in an ampule. The SEM and EDS analysis show the surface of pristine (Fig. 43a) and BP- (Fig. 43b) and b-AsP- (Fig. 43c) modified BDD electrodes, with the chemical composition of the last (Fig. 43d). It can be noticed that, similarly to the modification of other electrode materials, BP does not visibly change the structure of the top layer of the substrate. On the other hand, black arsenic-phosphorus crystallites can be clearly seen on top of the BDD substrate after the modification process. The implementation of BDD in chemical vapor transport strongly influences the growth process of b-AsP with the fabricated columns growing horizontally rather than vertically (Fig. 43c). The EDS analysis reveal, that the chemical composition of b-AsP modified BDDs consists of all expected elements and oxygen, which is common for BDD films grown on Si [272].

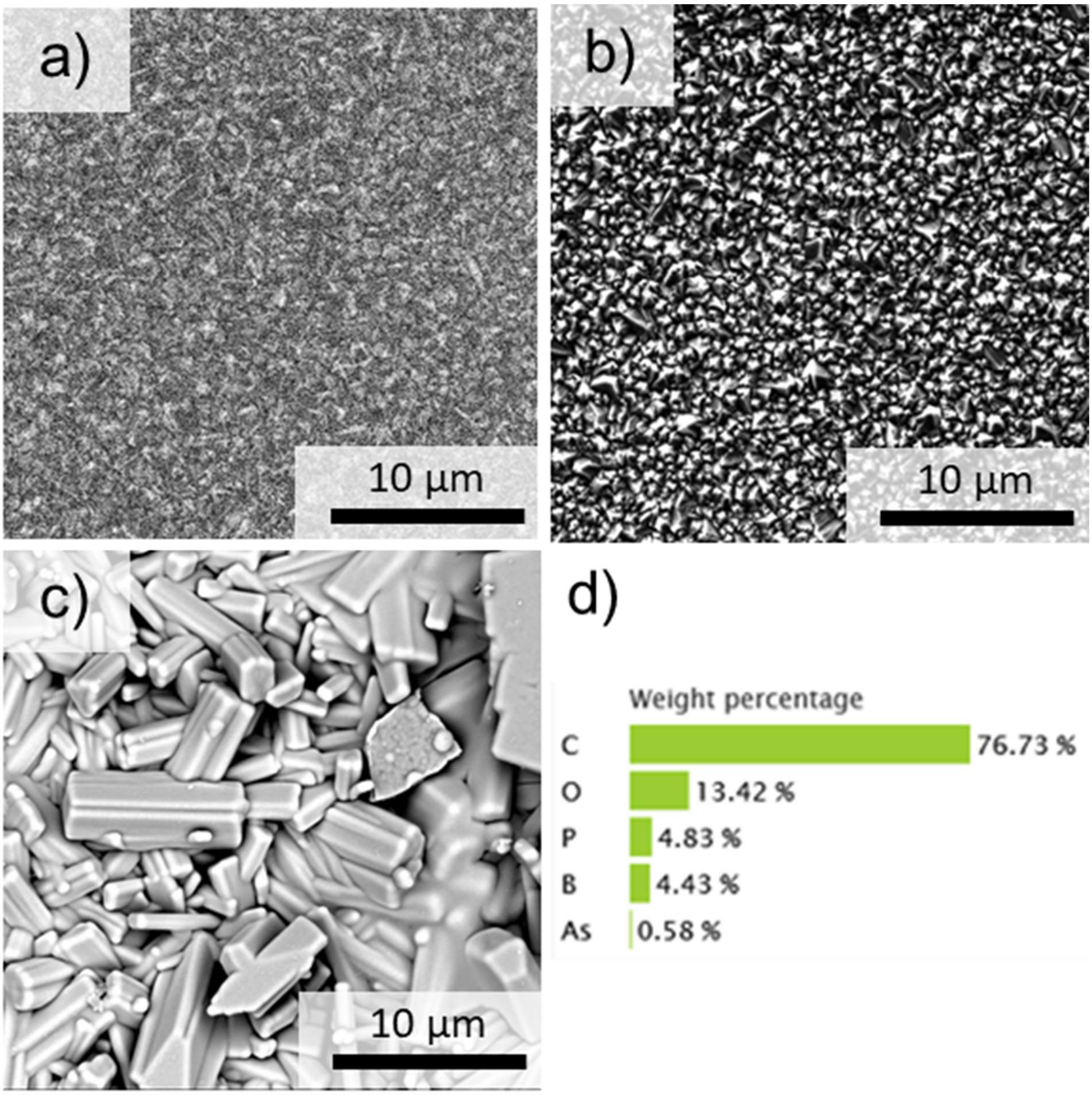

Figure 43. Surface morphology of a) pristine, b) BP-modified and c) b-AsP-modified BDD electrodes; d) chemical composition of modified electrodes.

The crystallinity of b-AsP modified BDD electrodes were investigated using Raman spectroscopy Fig. 44). The recorded spectra exhibit similar character as it was presented for b-AsP modified TiO_2 NTs, however in this case, the As vibrational modes show even better peak separation with A^1_g, B^2_g, A^2_g and B_{3g} modes being easily identified at 276^{-1}, 199 cm^{-1}, 223 cm^{-1} and 232 cm^{-1}, respectively. The slight shift of As modes towards lower wavenumbers, in comparison to nanotubes modification, can be attributed to bigger sizes of b-AsP structures grown during the modification process, according to Vishnoi et al. [273]. BP vibrational modes can be also easily identified with Raman lines at

349 cm^{-1}, 415 cm^{-1} and 453 cm^{-1} attributed to A^1_g, B^2_g, A^2_g modes, which in comparison to BP structures exhibit additional red-shifted, as reported by Hou et al. [246].

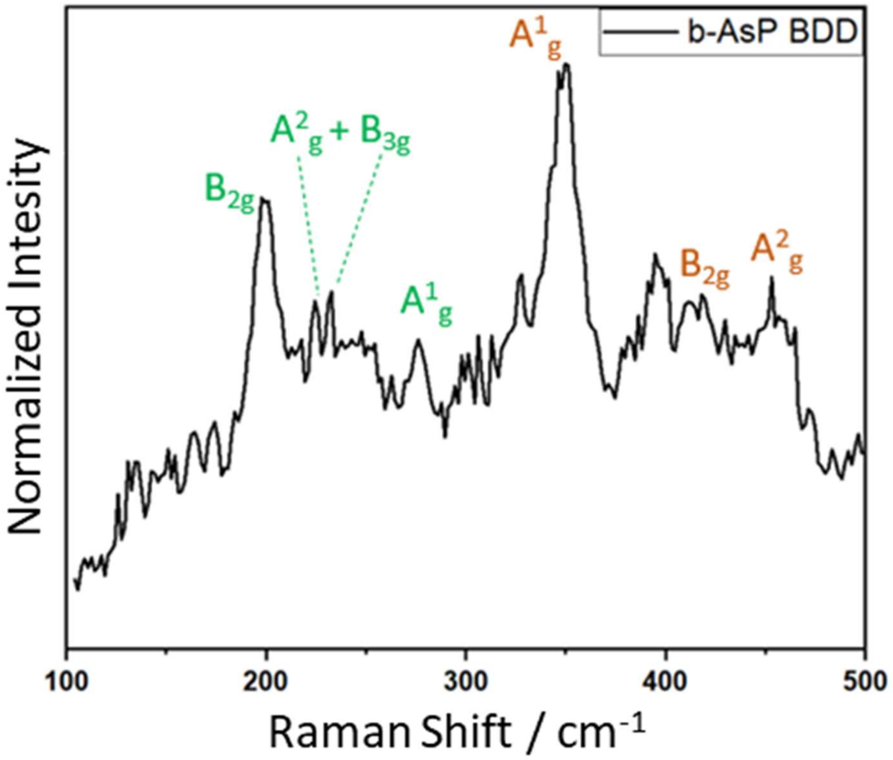

Figure 44. Raman spectra of b-AsP-modified BDD electrodes.

Table 2. Marked peak position of Raman spectra recorded for b-AsP-modified BDD electrodes and their attribution to corresponding vibrational modes.

Fitted Modes Maxima / cm^{-1}	Modes Identified as:
199	As B_{2g}
223	As A^2_g
232	As B_{3g}
276	As A^1_g
349	BP A^1_g
415	BP B_{2g}
453	BP A^2_g

In order to investigate the electrochemical performance of BP and b-AsP modified BDD electrode, potential window in 1 M KNO_3 linear sweep (LSV) and cyclic voltammetry (CV) and electrochemical impedance spectroscopy (EIS) were conducted. The electrochemical measurements were carried out in a three-electrode system, where the RE was an Ag/AgCl electrode in 1 M KCl, and a platinum wire was the CE. The potential window in 1 M KNO_3 shown in Fig. 45a is definitely smaller for b-AsP than for BP obtained by the CVT method. This may suggest the possibility of using the b-AsP structure in water splitting reactions [274]. Therefore, linear sweep voltammetry in 1 M NaOH was performed to compare the properties of BP- and b-AsP-modified BDD electrodes in oxygen evolution reactions (Fig. 45b). The obtained results show that b-AsP has a lower oxygen evolution potential, which suggests that this is the right direction and optimization of the composition could further improve the obtained results.

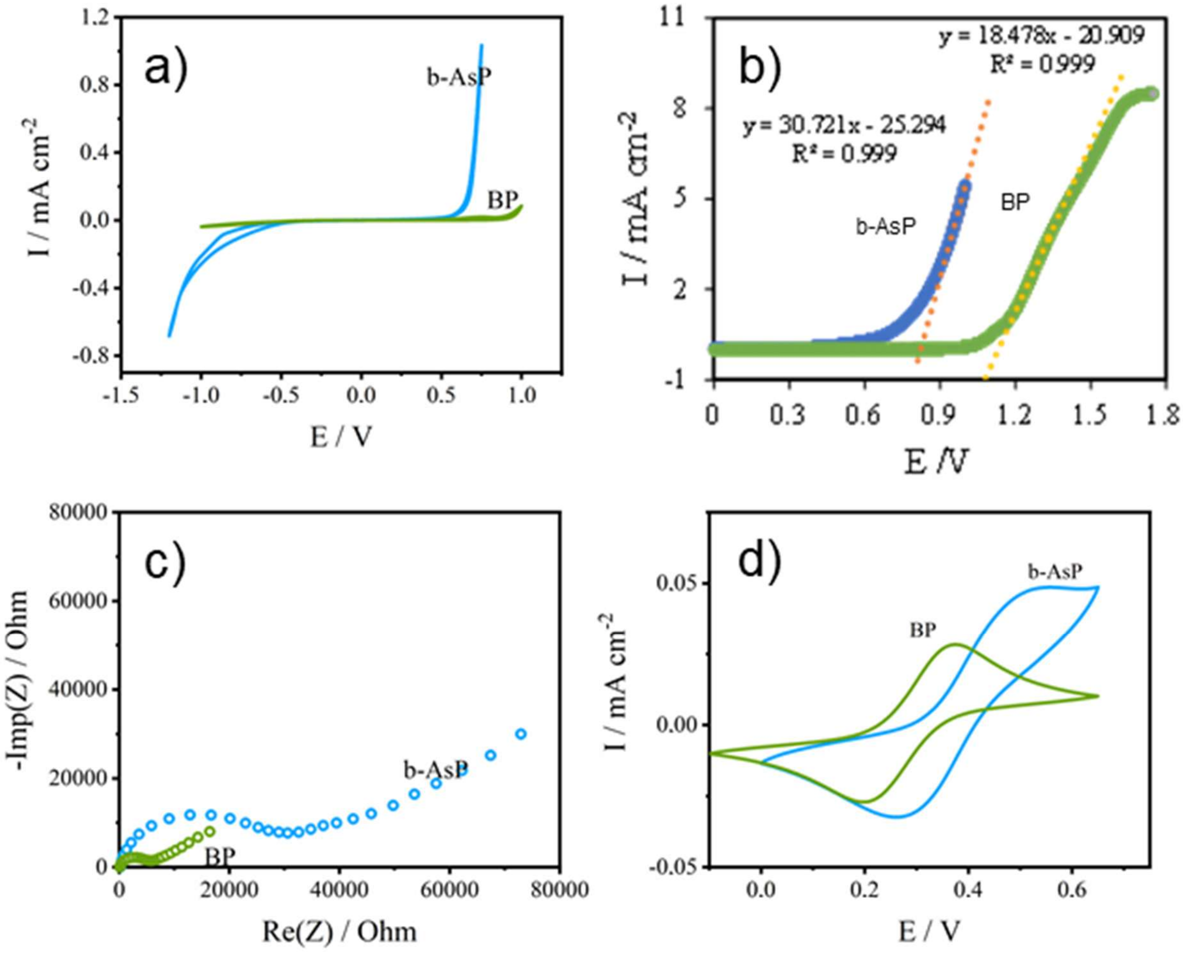

Figure 45. Electrochemical studies on BP- and b-AsP-modified BDD electrodes; a) Potential window in 1 M KNO_3, b) LSV for OER activity, c) impedance in 1 mM $Fe(CN)_6^{3-/4-}$/1 M KNO_3 solution, d) CV in 1 mM $Fe(CN)_6^{3-/4-}$/1 M KNO_3 solution for BP- and b-AsP-modified BDD electrodes.

The CV recorded in 1 M $Fe(CN)_6^{3-/4-}$/1 M KNO_3 solution for BP and b-AsP shows that the oxidation and reduction reactions taking place on the b-AsP electrode exhibit higher peak-to-peak separation (Fig. 45d), and consequently higher charge transfer resistance, which is also confirmed by the electrochemical impedance spectroscopy (Fig. 45c). During EIS, ferrocyanides can gather on the surface of the electrode, which cannot be removed without affecting the structure, due to previously mentioned poor air-stability of BP structures, possibly influencing the reliability of the results. It should also be noted that higher currents of the redox reaction were revealed for the b-AsP electrode, which may indicate a larger active surface area of the obtained structure. The obtained results show the possibility of controlling electrochemical properties, such as the size of the potential window and oxygen evolution reactions, by incorporating of a portion of the As atoms into BP-based structures, enabling sensing applications of b-AsP modified BDD.

In this chapter, the surface morphology and the chemical composition of BP and b-AsP modified gold array and BDD electrodes were investigated. The successful process of surface modification of chosen electrodes was demonstrated using SEM and EDS analysis, along with Raman spectroscopy in case of BDD electrodes. Moreover the electrochemical properties of BP and b-AsP modified BDD electrodes were investigated. It was proved that the incorporation of arsenic atoms into black phosphorus structures increases the electrochemical activity of the material, lowering oxygen evolution potential and while increasing the potential window and peak-to-peak separation. The additional As atoms in the modification process was shown to vastly influence the dimensions of grown nanostructures, which could influence the structural and electrochemical properties of electrode materials. Overall, the electrochemical studies of black arsenic-phosphorus coatings of electrode materials show an increase in electrochemical performance in comparison to black phosphorus.

Chapter 6. Summary, conclusions and possible further research directions

6.1 Summary of the obtained results

In this thesis, various BP-based structures were fabricated and investigated for their structural, optical, electrochemical and photoelectrochemical properties. These structures include:

- black phosphorus nanoflakes,
- black phosphorus columns,
- black phosphorus nanoribbon,
- black phosphorus coating,
- black arsenic-phosphorus columns,
- black arsenic-phosphorus ribbons,
- black arsenic-phosphorus crystallites,
- black arsenic-phosphorus coating.

All of the above-mentioned structures can be fabricated using the chemical vapor transport technique, and the form of the final product significantly depends on the substrate utilized in the process. The demonstrated results show that a lack of substrate will conclude in fabrication of bulk BP, substrates of flat and homogenous surface, such as Si and gold array electrode, will cause a more complicated structures formation (BP and b-AsP columns), whereas using electrode materials of high complexity like nanotubes and BDD electrodes will conclude in formation of BP-based coatings and crystallites. It was proved that among a number of possible methods for BP exfoliation, sonication-aided exfoliation is the most convenient. This method was proved to be effective and, as presented for BP nanoflakes, choosing specific solvents will influence the shape, distribution, and size of the fabricated nanostructures, all of which have a substantial impact on their properties. Sonication-based exfoliation is also time-saving in comparison to mechanical exfoliation, where one might need to exfoliate BP a number of times before obtaining expected dimensions. Whereas liquid-based exfoliation allows to fabricate nanostructures on a wide spectrum of sizes, leaving only the aspect of transporting the desired structure onto another substrate. Moreover, the final product is dispersed in a solution that, as presented for BP nanoflakes, stall the degradation process of the BP nanostructures allowing the fabrication process to be performed outside of a glovebox.

Black phosphorus nanosheets were synthesized by liquid-phase exfoliation of bulk BP in 3 organic solvents: NMP, DMSO, and Et_2O. The surface morphology analysis of all samples reveals a strong influence of the solvent chosen for the fabrication process on the shape, size, and distribution of the synthesized BP nanosheets. The anhydrous polar solvents used in the experiment, do not cause decomposition of the black phosphorus structure and for each spectrum, characteristic mods can be identified. The absorbance spectra recorded BP nanosheets dispersed in DMSO and NMP revealed the sample to be optically active across the whole analyzed range, with the intensity increasing toward lower wavelengths. The UV-Vis absorption spectra showed that the optical activity of BP flakes dispersed in

NMP vastly decreases as soon as 1 day after the fabrication process, which can be attributed to reaction with residual water/oxygen. The high chemical stability, the enormous surface-to-volume ratio and the optical activity across the whole UV-Vis range allows BP nanosheets to be applied in specific biosensing solutions and as electrode materials unachievable for bulk material proving **hypothesis I**.

As described in chapter 1, the optical, electronic, electrical and electrochemical properties of phosphorene and b-AsP low-dimensional structures are highly anisotropic. Moreover, the tunable bandgap of BP and b-AsP, possible quantum confinement effects, and the a wide range of dimensions of the BP nanostructures influence the electronic structure and carrier mobility of the material. The properties of phosphorene will differ along the ZZ and AC directions, thus the fabrication of the nanoribbons will require utilization of properties arising from just one of these directions. This phenomenon allows BP nanoribbons to surpass the optical and mechanical properties of BP nanosheets. The AC and ZZ directions can be identified by angle-dependent Raman spectroscopy, as presented in parts 5.3 and 5.5, revealing the CVT-fabricated BP nanoribbons to form along the ZZ direction. The results presented for BP nanoribbons also indicated that liquid phase exfoliation makes it possible to preserve the original width and length of the exfoliated 3D structures. Despite the lack of precise control over the dimensions of the fabricated structures, this method offers an approach for a simultaneous fabrication of nanostructures of various sizes. The structural properties of BP-based nanoribbons do not solely depend on the fabrication technique, and as presented in part 5.5, incorporating arsenic atoms into phosphorene diversified its structure, changing the shape and size of the fabricated b-AsP columns. Samples of various arsenic-to-phosphorus mass ratios varied in length and surface morphology, which makes it possible to design individual nanoribbons and columns for specific optoelectronic applications proving **hypothesis I**. Furthermore, the EDS studies of b-AsP nanoribbons showed high regularity of the chemical composition along the entire structure, which is necessary for implementing this material in electrical and optical devices. The angle-dependent Raman spectroscopy revealed, that similarly to BP columns, the CVT-fabricated b-AsP columns grow along the ZZ direction. Moreover, the temperature-dependent studies showed that the A^1_g, B_{2g}, and A^2_g modes display a rapid blue shift when lowering the temperature from 300 K and stabilizing the position of the modes at 100 K, suggesting a weakening of the tensile stress along the structure of the nanoribbons. The b-AsP ribbons presented in this dissertation were more stable in ambient conditions than pristine BP nanoribbons. Raman studies conducted for BP and b-AsP nanoribbons revealed that incorporating 10% of weight concentration of As into BP can increase air-stability of the material from less than 24 hours for BP to at least 2 weeks proving **hypothesis II**.

Besides BP and b-AsP nanoflakes and nanoribbons, the CVT technique was utilized for the surface modification of electrode materials. Titania nanotubes, boron-doped diamond thin films, and interdigitated array gold electrodes were successfully coated with BP and b-AsP. Titania nanotubes are known for their biocompatibility, chemical and physical stability, non-toxicity, and high corrosion resistance. Nonetheless, they are active only in the ultraviolet area and have a high carrier recombination rate during photocatalytic processes. However, surface modification with phosphorus-based coatings vastly improved their photoactivity and electrochemical performance. The surface morphology of BP-modified TiO_2 NTs showed the high regularity with BP covering both nanotubes and cracks in the whole layer. Raman studies confirmed high crystallinity of the structure, with spectra including all expected vibrational modes: A^1_g, B^{2g}, and A^2_g, characteristic for black phosphorus and the $E_{g(1)}$, $E_{g(2)}$, B_{1g}, A_{1g}, and $E_{g(3)}$ modes of anatase TiO_2 nanotubes. Moreover, the HRTEM and EDS studies revealed that a phosphorus layer was formed on both the inside and outside walls of the nanotubes, which could be utilized for the first experimentally fabricated phosphorene nanoribbons. Unlike for b-AsP, the electrochemical studies of BP-modified TiO_2 NTs were not reliable due to their rapid oxidation. The cracks occurring in the surface of nanotubes layer were not filled with b-AsP but are enhanced with the modification having a localized character. The modified nanotubes exhibited high crystallinity and displayed A^1_g, B^{2g}, and A^2_g modes for both BP and As, and $E_{g(1)}$, $E_{g(2)}$, B_{1g}, A_{1g}, and $E_{g(3)}$ of anatase TiO_2 NTs. The electrochemical studies revealed, that the b-AsP-modified electrodes display higher current values, suggesting an increase in electrochemical activity in comparison to pristine and BP-modified TiO_2 NTs, proving **hypothesis III**. Moreover, unlike for BP-modification, the b-AsP-modified TiO_2 nanotubes exhibited a reversible redox behavior in the cathodic range, as well as high stability after 3 cycles, proving **hypothesis II**. The photoactivity of the b-AsP-modified nanotubes was also vastly improved, with over 15 times higher current density obtained from the chronoamperometry curves in relation to the pristine nanotubes. The photoelectrochemical studies proved b-AsP TiO_2 NTs to be far more suitable for energy harvesting in comparison to unmodified nanotubes, once again validating **hypothesis III**.

The CVT technique was also be implemented for the modification of interdigitated array gold electrodes with BP and b-AsP. These studies showed the possibility of synthesizing of BP and b-AsP needle-like shapes. The surface morphology of the electrode after the modification process showed BP to form solely on top of Au arrays, creating a pattern of structures with an enormous surface-to-volume ratio, which might be successfully applied for sensing purposes. However, the EDS analysis reveals the BP structures to have oxidized heavily. The b-AsP-modified gold array electrode showed a slightly different structure, with b-AsP columns regularly spread across the whole electrode surface. The b-AsP grown columns were also much longer and thicker in comparison to the ones grown in phosphorus modification. The chemical composition of these structures revealed that the b-AsP columns do not oxidize as easily as in case in phosphorus modification, which indicates air-stability of these structures proving **hypothesis II**. The full coverage of Au electrodes with b-AsP structures undoubtedly excludes its application in FETs, but can still be utilized for gas and electroanalytical sensors.

The last studied electrode material for the modification of BP and b-AsP was boron-doped diamond thin film. The modification was carried out using the CVT technique with a BDD substrate used instead of Si wafers in a glass ampule. The surface morphology of BDD electrodes after modification show, that BP was not visibly change the structure of the top layer of the substrate, unlike black arsenic-phosphorus, where crystallites were clearly seen on top of the BDD substrate after the modification process. Moreover, the implementation of BDD in chemical vapor transport strongly influences the growth process of b-AsP with the fabricated columns growing horizontally rather than vertically. Raman studies and EDS analysis conducted for the b-AsP-modified BDD electrodes indicated the modification process to be successful, with desired chemical composition and As and BP modes present in the Raman spectra. The electrochemical studies revealed the b-AsP modification to be more chemically stable, but to also exhibited a lower oxygen evolution potential, higher peak-to-peak separation, and higher charge transfer resistance in comparison to BP-modified BDD. Moreover, the b-AsP-modified electrode showed higher currents of the redox reaction, indicating a larger active surface area of the obtained structure.

In summary, controlling the structural properties of BP and b-AsP nanostructures led to creating materials that exhibit quantum confinement, a high surface-to-volume ratio and a large number of active sites, all of which are desirable for electrochemical, electrical and sensing devices. The electrochemical and Raman studies showed the b-AsP structures to not only be more stable in an oxygen atmosphere and aqueous solutions than BP structures, but also display an increase in the electrochemical and photoelectrochemical properties in comparison to BP-modified and unmodified electrode materials, thus proving **all 3 of the formulated hypotheses**.

6.2 Future plans

Most of the studies presented in this dissertation focus on the electrochemical and optical properties of BP and b-AsP nanostructures. The ongoing research and future plans include further Raman investigations of b-AsP nanoribbons of various P-to-As ratios. Moreover, a field effect transistor constructed from b-AsP nanoribbons in order to establish their electrical properties is also being investigated. Similarly, the influence of the P-to-As ratio will be investigated for the photoactivity and electrochemical performance of AsP-modified TiO_2 NTs. Furthermore, the possibility to synthesize b-AsP and BP nanoribbons from modified nanotubes is also considered to be accomplished in the future. Finally, BDD and gold array electrodes will be studied for their sensing applications and electrochemical performance.

REFERENCES

1. Bridgman, P.W. TWO NEW MODIFICATIONS OF PHOSPHORUS. *J. Am. Chem. Soc.* **1914**, *36*, 1344–1363, doi:10.1021/ja02184a002.

2. Keyes, R.W. The Electrical Properties of Black Phosphorus. *Phys. Rev.* **1953**, *92*, 580–584, doi:10.1103/PhysRev.92.580.

3. Brown, A.; Rundqvist, S. Refinement of the Crystal Structure of Black Phosphorus. *Acta Crystallogr.* **1965**, *19*, 684–685, doi:10.1107/S0365110X65004140.

4. Lange, S.; Schmidt, P.; Nilges, T. Au3SnP7@black Phosphorus: An Easy Access to Black Phosphorus. *Inorg. Chem.* **2007**, *46*, 4028–4035, doi:10.1021/ic062192q.

5. Köpf, M.; Eckstein, N.; Pfister, D.; Grotz, C.; Krüger, I.; Greiwe, M.; Hansen, T.; Kohlmann, H.; Nilges, T. Access and in Situ Growth of Phosphorene-Precursor Black Phosphorus. *J. Cryst. Growth* **2014**, *405*, 6–10, doi:10.1016/j.jcrysgro.2014.07.029.

6. Cai, Y.; Zhang, G.; Zhang, Y.-W. *Phosphorene: Physical Properties, Synthesis, and Fabrication*; CRC Press, 2019; ISBN 978-1-351-35834-7.

7. Hultgren, R.; Gingrich, N.S.; Warren, B.E. The Atomic Distribution in Red and Black Phosphorus and the Crystal Structure of Black Phosphorus. *J. Chem. Phys.* **1935**, *3*, 351–355, doi:10.1063/1.1749671.

8. Clark, S.M.; Zaug, J.M. Compressibility of Cubic White, Orthorhombic Black, Rhombohedral Black, and Simple Cubic Black Phosphorus. *Phys. Rev. B* **2010**, *82*, 134111, doi:10.1103/PhysRevB.82.134111.

9. Ribeiro-Soares, J.; Almeida, R.M.; Cançado, L.G.; Dresselhaus, M.S.; Jorio, A. Group Theory for Structural Analysis and Lattice Vibrations in Phosphorene Systems. *Phys. Rev. B* **2015**, *91*, 205421, doi:10.1103/PhysRevB.91.205421.

10. Lopez-Bezanilla, A. Effect of Atomic-Scale Defects and Dopants on Phosphorene Electronic Structure and Quantum Transport Properties. *Phys. Rev. B* **2016**, *93*, 035433, doi:10.1103/PhysRevB.93.035433.

11. Liang, L.; Wang, J.; Lin, W.; Sumpter, B.G.; Meunier, V.; Pan, M. Electronic Bandgap and Edge Reconstruction in Phosphorene Materials. *Nano Lett.* **2014**, *14*, 6400–6406, doi:10.1021/nl502892t.

12. Kharche, N.; Nayak, S.K. Quasiparticle Band Gap Engineering of Graphene and Graphone on Hexagonal Boron Nitride Substrate. *Nano Lett.* **2011**, *11*, 5274–5278, doi:10.1021/nl202725w.

13. Edgar, J.H.; Hoffman, T.B.; Clubine, B.; Currie, M.; Du, X.Z.; Lin, J.Y.; Jiang, H.X. Characterization of Bulk Hexagonal Boron Nitride Single Crystals Grown by the Metal Flux Technique. *J. Cryst. Growth* **2014**, *403*, 110–113, doi:10.1016/j.jcrysgro.2014.06.006.

14. Churchill, H.O.H.; Jarillo-Herrero, P. Phosphorus Joins the Family. *Nat. Nanotechnol.* **2014**, *9*, 330–331, doi:10.1038/nnano.2014.85.

15. Wang, G.; Pandey, R.; Karna, S.P. Effects of Extrinsic Point Defects in Phosphorene: B, C, N, O, and F Adatoms. *Appl. Phys. Lett.* **2015**, *106*, 173104, doi:10.1063/1.4919389.

16. Ge, X.; Xia, Z.; Guo, S. Recent Advances on Black Phosphorus for Biomedicine and Biosensing. *Adv. Funct. Mater.* **2019**, *29*, 1900318, doi:10.1002/adfm.201900318.

17. Pumera, M. Phosphorene and Black Phosphorus for Sensing and Biosensing. *TrAC Trends Anal. Chem.* **2017**, *93*, 1–6, doi:10.1016/j.trac.2017.05.002.

18. Cai, Y.; Zhang, G.; Zhang, Y.-W. Layer-Dependent Band Alignment and Work Function of Few-Layer Phosphorene. *Sci. Rep.* **2014**, *4*, 6677, doi:10.1038/srep06677.

19. Tran, V.; Soklaski, R.; Liang, Y.; Yang, L. Layer-Controlled Band Gap and Anisotropic Excitons in Few-Layer Black Phosphorus. *Phys. Rev. B* **2014**, *89*, 235319, doi:10.1103/PhysRevB.89.235319.

20. Molas, M.R.; Macewicz, Ł.; Wieloszyńska, A.; Jakóbczyk, P.; Wysmołek, A.; Bogdanowicz, R.; Jasinski, J.B. Photoluminescence as a Probe of Phosphorene Properties. *Npj 2D Mater. Appl.* **2021**, *5*, 1–24, doi:10.1038/s41699-021-00263-8.

21. Berry, V. Impermeability of Graphene and Its Applications. *Carbon* **2013**, *62*, 1–10, doi:10.1016/j.carbon.2013.05.052.

22. Mir, S.H.; Yadav, V.K.; Singh, J.K. Recent Advances in the Carrier Mobility of Two-Dimensional Materials: A Theoretical Perspective. *ACS Omega* **2020**, *5*, 14203–14211, doi:10.1021/acsomega.0c01676.

23. Long, Y.; Zhang, C.; Wang, X.; Gao, J.; Wang, W.; Liu, Y. Oxidation of SO2 to SO3 Catalyzed by Graphene Oxide Foams. *J. Mater. Chem.* **2011**, *21*, 13934–13941, doi:10.1039/C1JM12031J.

24. Xiang, Q.; Yu, J. Graphene-Based Photocatalysts for Hydrogen Generation. *J. Phys. Chem. Lett.* **2013**, *4*, 753–759, doi:10.1021/jz302048d.

25. Zhang, L.; Xia, Z. Mechanisms of Oxygen Reduction Reaction on Nitrogen-Doped Graphene for Fuel Cells. *J. Phys. Chem. C* **2011**, *115*, 11170–11176, doi:10.1021/jp201991j.

26. Zhang, K.; Feng, Y.; Wang, F.; Yang, Z.; Wang, J. Two Dimensional Hexagonal Boron Nitride (2D-HBN): Synthesis, Properties and Applications. *J. Mater. Chem. C* **2017**, *5*, 11992–12022, doi:10.1039/C7TC04300G.

27. Yu, W.J.; Liu, Y.; Zhou, H.; Yin, A.; Li, Z.; Huang, Y.; Duan, X. Highly Efficient Gate-Tunable Photocurrent Generation in Vertical Heterostructures of Layered Materials. *Nat. Nanotechnol.* **2013**, *8*, 952–958, doi:10.1038/nnano.2013.219.

28. Amin, B.; Singh, N.; Schwingenschlögl, U. Heterostructures of Transition Metal Dichalcogenides. *Phys. Rev. B* **2015**, *92*, 075439, doi:10.1103/PhysRevB.92.075439.

29. Brent, J.R.; Savjani, N.; O'Brien, P. Synthetic Approaches to Two-Dimensional Transition Metal Dichalcogenide Nanosheets. *Prog. Mater. Sci.* **2017**, *89*, 411–478, doi:10.1016/j.pmatsci.2017.06.002.

30. Cheng, F.; Xu, H.; Xu, W.; Zhou, P.; Martin, J.; Loh, K.P. Controlled Growth of 1D MoSe2 Nanoribbons with Spatially Modulated Edge States. *Nano Lett.* **2017**, *17*, 1116–1120, doi:10.1021/acs.nanolett.6b04715.

31. Wang, Q.H.; Kalantar-Zadeh, K.; Kis, A.; Coleman, J.N.; Strano, M.S. Electronics and Optoelectronics of Two-Dimensional Transition Metal Dichalcogenides. *Nat. Nanotechnol.* **2012**, *7*, 699–712, doi:10.1038/nnano.2012.193.

32. Miao, J.; Zhang, L.; Wang, C. Black Phosphorus Electronic and Optoelectronic Devices. *2D Mater.* **2019**, *6*, 032003, doi:10.1088/2053-1583/ab1ebd.

33. Meshginqalam, B.; Barvestani, J. Performance Enhancement of SPR Biosensor Based on Phosphorene and Transition Metal Dichalcogenides for Sensing DNA Hybridization. *IEEE Sens. J.* **2018**, *18*, 7537–7543, doi:10.1109/JSEN.2018.2861829.

34. Gogotsi, Y.; Anasori, B. The Rise of MXenes. *ACS Nano* **2019**, *13*, 8491–8494, doi:10.1021/acsnano.9b06394.

35. Shukla, V. The Tunable Electric and Magnetic Properties of 2D MXenes and Their Potential Applications. *Mater. Adv.* **2020**, *1*, 3104–3121, doi:10.1039/D0MA00548G.

36. Li, J.; Guo, C.; Li, C.M. Recent Advances of Two-Dimensional (2 D) MXenes and Phosphorene for High-Performance Rechargeable Batteries. *ChemSusChem* **2020**, *13*, 1047–1070, doi:10.1002/cssc.202000061.

37. Kang, M.-H.; Lee, D.; Sung, J.; Kim, J.; Kim, B.H.; Park, J. 2.04 - Structure and Chemistry of 2D Materials. In *Comprehensive Nanoscience and Nanotechnology (Second Edition)*; Andrews, D.L., Lipson, R.H., Nann, T., Eds.; Academic Press: Oxford, 2019; pp. 55–90 ISBN 978-0-12-812296-9.

38. Timmerman, M.A.; Xia, R.; Wang, Y.; Sotthewes, K.; Huijben, M.; Elshof, J.E. ten Long-Range Ordering of Two-Dimensional Wide Bandgap Tantalum Oxide Nanosheets in Printed Films. *J. Mater. Chem. C* **2021**, *9*, 5699–5705, doi:10.1039/D1TC00801C.

39. Mohamad Nasir, M.Z.; Pumera, M. Emerging Mono-Elemental 2D Nanomaterials for Electrochemical Sensing Applications: From Borophene to Bismuthene. *TrAC Trends Anal. Chem.* **2019**, *121*, 115696, doi:10.1016/j.trac.2019.115696.

40. Zhao, J.; Liu, H.; Yu, Z.; Quhe, R.; Zhou, S.; Wang, Y.; Liu, C.C.; Zhong, H.; Han, N.; Lu, J.; et al. Rise of Silicene: A Competitive 2D Material. *Prog. Mater. Sci.* **2016**, *83*, 24–151, doi:10.1016/j.pmatsci.2016.04.001.

41. Tao, L.; Cinquanta, E.; Chiappe, D.; Grazianetti, C.; Fanciulli, M.; Dubey, M.; Molle, A.; Akinwande, D. Silicene Field-Effect Transistors Operating at Room Temperature. *Nat. Nanotechnol.* **2015**, *10*, 227–231, doi:10.1038/nnano.2014.325.

42. Du, Y.; Zhuang, J.; Liu, H.; Xu, X.; Eilers, S.; Wu, K.; Cheng, P.; Zhao, J.; Pi, X.; See, K.W.; et al. Tuning the Band Gap in Silicene by Oxidation. *ACS Nano* **2014**, *8*, 10019–10025, doi:10.1021/nn504451t.

43. Zhu, F.; Chen, W.; Xu, Y.; Gao, C.; Guan, D.; Liu, C.; Qian, D.; Zhang, S.-C.; Jia, J. Epitaxial Growth of Two-Dimensional Stanene. *Nat. Mater.* **2015**, *14*, 1020–1025, doi:10.1038/nmat4384.

44. Liu, N.; Bo, G.; Liu, Y.; Xu, X.; Du, Y.; Dou, S.X. Recent Progress on Germanene and Functionalized Germanene: Preparation, Characterizations, Applications, and Challenges. *Small* **2019**, *15*, 1805147, doi:10.1002/smll.201805147.

45. Pumera, M.; Sofer, Z. 2D Monoelemental Arsenene, Antimonene, and Bismuthene: Beyond Black Phosphorus. *Adv. Mater.* **2017**, *29*, 1605299, doi:10.1002/adma.201605299.

46. Zhang, S.; Yan, Z.; Li, Y.; Chen, Z.; Zeng, H. Atomically Thin Arsenene and Antimonene: Semimetal–Semiconductor and Indirect–Direct Band-Gap Transitions. *Angew. Chem.* **2015**, *127*, 3155–3158, doi:10.1002/ange.201411246.

47. Rangel, N.L.; Sotelo, J.C.; Seminario, J.M. Mechanism of Carbon Nanotubes Unzipping into Graphene Ribbons. *J. Chem. Phys.* **2009**, *131*, 031105, doi:10.1063/1.3170926.

48. Guo, Z.; Zhang, H.; Lu, S.; Wang, Z.; Tang, S.; Shao, J.; Sun, Z.; Xie, H.; Wang, H.; Yu, X.-F.; et al. From Black Phosphorus to Phosphorene: Basic Solvent Exfoliation, Evolution of Raman Scattering, and Applications to Ultrafast Photonics. *Adv. Funct. Mater.* **2015**, *25*, 6996–7002, doi:10.1002/adfm.201502902.

49. Jia, J.; Jang, S.K.; Lai, S.; Xu, J.; Choi, Y.J.; Park, J.-H.; Lee, S. Plasma-Treated Thickness-Controlled Two-Dimensional Black Phosphorus and Its Electronic Transport Properties. *ACS Nano* **2015**, *9*, 8729–8736, doi:10.1021/acsnano.5b04265.

50. Mu, Y.; Si, M.S. The Mechanical Exfoliation Mechanism of Black Phosphorus to Phosphorene: A First-Principles Study. *EPL Europhys. Lett.* **2015**, *112*, 37003, doi:10.1209/0295-5075/112/37003.

51. Ciesielski, A.; Samorì, P. Graphene via Sonication Assisted Liquid-Phase Exfoliation. *Chem. Soc. Rev.* **2014**, *43*, 381–398, doi:10.1039/C3CS60217F.

52. Brodie, B.C. XIII. On the Atomic Weight of Graphite. *Philos. Trans. R. Soc. Lond.* **1859**, *149*, 249–259, doi:10.1098/rstl.1859.0013.

53. Ambrosetti, A.; Silvestrelli, P.L. Hidden by Graphene – Towards Effective Screening of Interface van Der Waals Interactions via Monolayer Coating. *Carbon* **2018**, *139*, 486–491, doi:10.1016/j.carbon.2018.07.011.

54. Xu, Y.; Cao, H.; Xue, Y.; Li, B.; Cai, W. Liquid-Phase Exfoliation of Graphene: An Overview on Exfoliation Media, Techniques, and Challenges. *Nanomaterials* **2018**, *8*, 942, doi:10.3390/nano8110942.

55. Brent, J.R.; Savjani, N.; Lewis, E.A.; Haigh, S.J.; Lewis, D.J.; O'Brien, P. Production of Few-Layer Phosphorene by Liquid Exfoliation of Black Phosphorus. *Chem. Commun.* **2014**, *50*, 13338–13341, doi:10.1039/C4CC05752J.

56. Yasaei, P.; Kumar, B.; Foroozan, T.; Wang, C.; Asadi, M.; Tuschel, D.; Indacochea, J.E.; Klie, R.F.; Salehi-Khojin, A. High-Quality Black Phosphorus Atomic Layers by Liquid-Phase Exfoliation. *Adv. Mater.* **2015**, *27*, 1887–1892, doi:10.1002/adma.201405150.

57. Kumar, A. Simultaneous Passivation and Encapsulation of Black Phosphorus Nanosheets (Phosphorene) by Optically Active Polypeptide Micelles for Biosensors. *ACS Appl. Nano Mater.* **2019**, *2*, 2397–2404, doi:10.1021/acsanm.9b00265.

58. Fang, Y.; Li, X.; Li, J.; Yao, C.; Hoh, H.Y.; Hai, X.; Lu, J.; Su, C. Janus Electrochemical Exfoliation of Two-Dimensional Materials. *J. Mater. Chem. A* **2019**, *7*, 25691–25711, doi:10.1039/C9TA10487A.

59. Ambrosi, A.; Sofer, Z.; Pumera, M. Electrochemical Exfoliation of Layered Black Phosphorus into Phosphorene. *Angew. Chem.* **2017**, *129*, 10579–10581, doi:10.1002/ange.201705071.

60. Erande, M.B.; Suryawanshi, S.R.; More, M.A.; Late, D.J. Electrochemically Exfoliated Black Phosphorus Nanosheets – Prospective Field Emitters. *Eur. J. Inorg. Chem.* **2015**, *2015*, 3102–3107, doi:10.1002/ejic.201500145.

61. Li, Y.; Yan, H.; Xu, B.; Zhen, L.; Xu, C. Electrochemical Intercalation in Atomically Thin van Der Waals Materials for Structural Phase Transition and Device Applications. *Adv. Mater.* **2021**, *33*, 2000581, doi:10.1002/adma.202000581.

62. Stark, M.S.; Kuntz, K.L.; Martens, S.J.; Warren, S.C. Intercalation of Layered Materials from Bulk to 2D. *Adv. Mater.* **2019**, *31*, 1808213, doi:10.1002/adma.201808213.

63. Nishii, T.; Maruyama, Y.; Inabe, T.; Shirotani, I. Synthesis and Characterization of Black Phosphorus Intercalation Compounds. *Synth. Met.* **1987**, *18*, 559–564, doi:10.1016/0379-6779(87)90940-4.

64. Huang, G.Q.; Xing, Z.W.; Xing, D.Y. Prediction of Superconductivity in Li-Intercalated Bilayer Phosphorene. *Appl. Phys. Lett.* **2015**, *106*, 113107, doi:10.1063/1.4916100.

65. Watts, M.C.; Picco, L.; Russell-Pavier, F.S.; Cullen, P.L.; Miller, T.S.; Bartuś, S.P.; Payton, O.D.; Skipper, N.T.; Tileli, V.; Howard, C.A. Production of Phosphorene Nanoribbons. *Nature* **2019**, *568*, 216–220, doi:10.1038/s41586-019-1074-x.

66. Han, Z.J.; Murdock, A.T.; Seo, D.H.; Bendavid, A. Recent Progress in Plasma-Assisted Synthesis and Modification of 2D Materials. *2D Mater.* **2018**, *5*, 032002, doi:10.1088/2053-1583/aabb81.

67. Sun, H.; Dong, J.; Liu, F.; Ding, F. Etching of Two-Dimensional Materials. *Mater. Today* **2021**, *42*, 192–213, doi:10.1016/j.mattod.2020.09.031.

68. Lu, W.; Nan, H.; Hong, J.; Chen, Y.; Zhu, C.; Liang, Z.; Ma, X.; Ni, Z.; Jin, C.; Zhang, Z. Plasma-Assisted Fabrication of Monolayer Phosphorene and Its Raman Characterization. *Nano Res.* **2014**, *7*, 853–859, doi:10.1007/s12274-014-0446-7.

69. Huang, H.; Gao, M.; Kang, Y.; Li, J.; Wang, J.; Wu, L.; Chu, P.K.; Huang, Y.; Ibarra, M.R.; Yu, X.-F. Rapid and Scalable Production of High-Quality Phosphorene by Plasma–Liquid Technology. *Chem. Commun.* **2019**, *56*, 221–224, doi:10.1039/C9CC07640A.

70. Rajabali, M.; Esfandiari, M.; Rajabali, S.; Vakili-Tabatabaei, M.; Mohajerzadeh, S.; Mohajerzadeh, S. High-Performance Phosphorene-Based Transistors Using a Novel Exfoliation-Free Direct Crystallization on Silicon Substrates. *Adv. Mater. Interfaces* **2020**, *7*, 2000774, doi:10.1002/admi.202000774.

71. Lee, Y.-H.; Zhang, X.-Q.; Zhang, W.; Chang, M.-T.; Lin, C.-T.; Chang, K.-D.; Yu, Y.-C.; Wang, J.T.-W.; Chang, C.-S.; Li, L.-J.; et al. Synthesis of Large-Area MoS2 Atomic Layers with Chemical Vapor Deposition. *Adv. Mater. Deerfield Beach Fla* **2012**, *24*, 2320–2325, doi:10.1002/adma.201104798.

72. Shen, P.-C.; Lin, Y.; Wang, H.; Park, J.-H.; Leong, W.S.; Lu, A.-Y.; Palacios, T.; Kong, J. CVD Technology for 2-D Materials. *IEEE Trans. Electron Devices* **2018**, *65*, 4040–4052, doi:10.1109/TED.2018.2866390.

73. Hyun, C.-M.; Choi, J.-H.; Lee, S.W.; Park, J.H.; Lee, K.-T.; Ahn, J.-H. Synthesis Mechanism of MoS2 Layered Crystals by Chemical Vapor Deposition Using MoO3 and Sulfur Powders. *J. Alloys Compd.* **2018**, *765*, 380–384, doi:10.1016/j.jallcom.2018.06.183.

74. Zhao, B.; Shen, D.; Zhang, Z.; Lu, P.; Hossain, M.; Li, J.; Li, B.; Duan, X. 2D Metallic Transition-Metal Dichalcogenides: Structures, Synthesis, Properties, and Applications. *Adv. Funct. Mater.* **2021**, *31*, 2105132, doi:10.1002/adfm.202105132.

75. Han, W.; Liu, K.; Yang, S.; Wang, F.; Su, J.; Jin, B.; Li, H.; Zhai, T. Salt-Assisted Chemical Vapor Deposition of Two-Dimensional Materials. *Sci. China Chem.* **2019**, *62*, 1300–1311, doi:10.1007/s11426-019-9525-y.

76. Fan, Y.; Li, L.; Zhang, Y.; Zhang, X.; Geng, D.; Hu, W. Recent Advances in Growth of Transition Metal Carbides and Nitrides (MXenes) Crystals. *Adv. Funct. Mater.* **2022**, *32*, 2111357, doi:10.1002/adfm.202111357.

77. Butler, J.E.; Sumant, A.V. The CVD of Nanodiamond Materials. *Chem. Vap. Depos.* **2008**, *14*, 145–160, doi:10.1002/cvde.200700037.

78. Li, X.; Deng, B.; Wang, X.; Chen, S.; Vaisman, M.; Karato, S.; Pan, G.; Lee, M.L.; Cha, J.; Wang, H.; et al. Synthesis of Thin-Film Black Phosphorus on a Flexible Substrate. *2D Mater.* **2015**, *2*, 031002, doi:10.1088/2053-1583/2/3/031002.

79. Smith, J.B.; Hagaman, D.; Ji, H.-F. Growth of 2D Black Phosphorus Film from Chemical Vapor Deposition. *Nanotechnology* **2016**, *27*, 215602, doi:10.1088/0957-4484/27/21/215602.

80. Qiu, L.; C. Dong, J.; Ding, F. Selective Growth of Two-Dimensional Phosphorene on Catalyst Surface. *Nanoscale* **2018**, *10*, 2255–2259, doi:10.1039/C7NR08507A.

81. Binnewies, M.; Glaum, R.; Schmidt, M.; Schmidt, P. *Chemical Vapor Transport Reactions*; De Gruyter, 2012; ISBN 978-3-11-025465-5.

82. Wang, D.; Luo, F.; Lu, M.; Xie, X.; Huang, L.; Huang, W. Chemical Vapor Transport Reactions for Synthesizing Layered Materials and Their 2D Counterparts. *Small* **2019**, *15*, 1804404, doi:10.1002/smll.201804404.

83. Ferreira, S.O. *Advanced Topics on Crystal Growth*; 2013; ISBN 978-953-51-1010-1.

84. Lei, W.; Liu, G.; Zhang, J.; Liu, M. Black Phosphorus Nanostructures: Recent Advances in Hybridization, Doping and Functionalization. *Chem. Soc. Rev.* **2017**, *46*, 3492–3509, doi:10.1039/C7CS00021A.

85. Sakthivel, T.; Huang, X.; Wu, Y.; Rtimi, S. Recent Progress in Black Phosphorus Nanostructures as Environmental Photocatalysts. *Chem. Eng. J.* **2020**, *379*, 122297, doi:10.1016/j.cej.2019.122297.

86. Yuan, H.; Liu, X.; Afshinmanesh, F.; Li, W.; Xu, G.; Sun, J.; Lian, B.; Curto, A.G.; Ye, G.; Hikita, Y.; et al. Polarization-Sensitive Broadband Photodetector Using a Black Phosphorus Vertical p–n Junction. *Nat. Nanotechnol.* **2015**, *10*, 707–713, doi:10.1038/nnano.2015.112.

87. Zhang, W.; Yin, J.; Zhang, P.; Ding, Y. Strain/Stress Engineering on the Mechanical and Electronic Properties of Phosphorene Nanosheets and Nanotubes. *RSC Adv.* **2017**, *7*, 51466–51474, doi:10.1039/C7RA09668B.

88. Yang, Z.; Hao, J.; Yuan, S.; Lin, S.; Yau, H.M.; Dai, J.; Lau, S.P. Field-Effect Transistors Based on Amorphous Black Phosphorus Ultrathin Films by Pulsed Laser Deposition. *Adv. Mater.* **2015**, *27*, 3748–3754, doi:10.1002/adma.201500990.

89. Lewis, E.A.; Brent, J.R.; Derby, B.; Haigh, S.J.; Lewis, D.J. Solution Processing of Two-Dimensional Black Phosphorus. *Chem. Commun.* **2017**, *53*, 1445–1458, doi:10.1039/C6CC09658A.

90. Debu, D.T.; Bauman, S.J.; French, D.; Churchill, H.O.H.; Herzog, J.B. Tuning Infrared Plasmon Resonance of Black Phosphorene Nanoribbon with a Dielectric Interface. *Sci. Rep.* **2018**, *8*, 1–10, doi:10.1038/s41598-018-21365-2.

91. Carvalho, A.; Rodin, A.S.; Neto, A.H.C. Phosphorene Nanoribbons. *EPL Europhys. Lett.* **2014**, *108*, 47005, doi:10.1209/0295-5075/108/47005.

92. Campos-Delgado, J.; Romo-Herrera, J.M.; Jia, X.; Cullen, D.A.; Muramatsu, H.; Kim, Y.A.; Hayashi, T.; Ren, Z.; Smith, D.J.; Okuno, Y.; et al. Bulk Production of a New Form of Sp2 Carbon: Crystalline Graphene Nanoribbons. *Nano Lett.* **2008**, *8*, 2773–2778, doi:10.1021/nl801316d.

93. Peng, X.; Copple, A.; Wei, Q. Edge Effects on the Electronic Properties of Phosphorene Nanoribbons. *J. Appl. Phys.* **2014**, *116*, 144301, doi:10.1063/1.4897461.

94. Kumar, A. Controlled Nanostructures and Simultaneous Passivation of Black Phosphorus (Phosphorene) with Nafion. *J. Mater. Res.* **2020**, *35*, 141–152, doi:10.1557/jmr.2019.395.

95. Guo, H.; Lu, N.; Dai, J.; Wu, X.; Zeng, X.C. Phosphorene Nanoribbons, Phosphorus Nanotubes, and van Der Waals Multilayers. *J. Phys. Chem. C* **2014**, *118*, 14051–14059, doi:10.1021/jp505257g.

96. Yu, S.; Zhu, H.; Eshun, K.; Arab, A.; Badwan, A.; Li, Q. A Computational Study of the Electronic Properties of One-Dimensional Armchair Phosphorene Nanotubes. *J. Appl. Phys.* **2015**, *118*, 164306, doi:10.1063/1.4934852.

97. Fernández-Escamilla, H.N.; Guerrero-Sánchez, J.; Martínez-Guerra, E.; Takeuchi, N. Structural and Electronic Properties of Double-Walled Black Phosphorene Nanotubes: A Density Functional Theory Study. *J. Phys. Chem.* **2019**.

98. Wang, G.; Slough, W.J.; Pandey, R.; Karna, S.P. Degradation of Phosphorene in Air: Understanding at Atomic Level. *2D Mater.* **2016**, *3*, 025011, doi:10.1088/2053-1583/3/2/025011.

99. Pei, J.; Gai, X.; Yang, J.; Wang, X.; Yu, Z.; Choi, D.-Y.; Luther-Davies, B.; Lu, Y. Producing Air-Stable Monolayers of Phosphorene and Their Defect Engineering. *Nat. Commun.* **2016**, *7*, 10450, doi:10.1038/ncomms10450.

100. Zheng, Y.; Chen, Y.; Gao, B.; Lin, B.; Wang, X. Phosphorene-Based Heterostructured Photocatalysts. *Engineering* **2021**, *7*, 991–1001, doi:10.1016/j.eng.2021.06.004.

101. Mo, J.; Xie, Q.; Wei, W.; Zhao, J. Revealing the Immune Perturbation of Black Phosphorus Nanomaterials to Macrophages by Understanding the Protein Corona. *Nat. Commun.* **2018**, *9*, 2480, doi:10.1038/s41467-018-04873-7.

102. Favron, A.; Gaufrès, E.; Fossard, F.; Phaneuf-L’Heureux, A.-L.; Tang, N.Y.-W.; Lévesque, P.L.; Loiseau, A.; Leonelli, R.; Francoeur, S.; Martel, R. Photooxidation and Quantum Confinement Effects in Exfoliated Black Phosphorus. *Nat. Mater.* **2015**, *14*, 826–832, doi:10.1038/nmat4299.

103. Wood, J.D.; Wells, S.A.; Jariwala, D.; Chen, K.-S.; Cho, E.; Sangwan, V.K.; Liu, X.; Lauhon, L.J.; Marks, T.J.; Hersam, M.C. Effective Passivation of Exfoliated Black Phosphorus Transistors against Ambient Degradation. *Nano Lett.* **2014**, *14*, 6964–6970, doi:10.1021/nl5032293.

104. Long, M.; Gao, A.; Wang, P.; Xia, H.; Ott, C.; Pan, C.; Fu, Y.; Liu, E.; Chen, X.; Lu, W.; et al. Room Temperature High-Detectivity Mid-Infrared Photodetectors Based on Black Arsenic Phosphorus. *Sci. Adv. 3*, e1700589, doi:10.1126/sciadv.1700589.

105. Yuan, S.; Shen, C.; Deng, B.; Chen, X.; Guo, Q.; Ma, Y.; Abbas, A.; Liu, B.; Haiges, R.; Ott, C.; et al. Air-Stable Room-Temperature Mid-Infrared Photodetectors Based on HBN/Black Arsenic Phosphorus/HBN Heterostructures. *Nano Lett.* **2018**, *18*, 3172–3179, doi:10.1021/acs.nanolett.8b00835.

106. Wang, H.; Yu, X.-F. Few-Layered Black Phosphorus: From Fabrication and Customization to Biomedical Applications. *Small* **2018**, *14*, 1702830, doi:10.1002/smll.201702830.

107. Chen, P.; Li, N.; Chen, X.; Ong, W.-J.; Zhao, X. The Rising Star of 2D Black Phosphorus beyond Graphene: Synthesis, Properties and Electronic Applications. *2D Mater.* **2017**, *5*, 014002, doi:10.1088/2053-1583/aa8d37.

108. Zhou, Y.; Zhang, M.; Guo, Z.; Miao, L.; Han, S.-T.; Wang, Z.; Zhang, X.; Zhang, H.; Peng, Z. Recent Advances in Black Phosphorus-Based Photonics, Electronics, Sensors and Energy Devices. *Mater. Horiz.* **2017**, *4*, 997–1019, doi:10.1039/C7MH00543A.

109. Cheng, J.; Gao, L.; Li, T.; Mei, S.; Wang, C.; Wen, B.; Huang, W.; Li, C.; Zheng, G.; Wang, H.; et al. Two-Dimensional Black Phosphorus Nanomaterials: Emerging Advances in Electrochemical Energy Storage Science. *Nano-Micro Lett.* **2020**, *12*, 179, doi:10.1007/s40820-020-00510-5.

110. Wu, S.; Hui, K.S.; Hui, K.N. 2D Black Phosphorus: From Preparation to Applications for Electrochemical Energy Storage. *Adv. Sci.* **2018**, *5*, 1700491, doi:10.1002/advs.201700491.

111. Zhang, Y.; Jiang, Q.; Lang, P.; Yuan, N.; Tang, J. Fabrication and Applications of 2D Black Phosphorus in Catalyst, Sensing and Electrochemical Energy Storage. *J. Alloys Compd.* **2021**, *850*, 156580, doi:10.1016/j.jallcom.2020.156580.

112. Batmunkh, M.; Bat-Erdene, M.; Shapter, J.G. Black Phosphorus: Synthesis and Application for Solar Cells. *Adv. Energy Mater.* **2018**, *8*, 1701832, doi:10.1002/aenm.201701832.

113. Shaikh, J.S.; Shaikh, N.S.; Sabale, S.; Parveen, N.; Patil, S.P.; Mishra, Y.K.; Kanjanaboos, P.; Praserthdam, S.; Lokhande, C.D. A Phosphorus Integrated Strategy for Supercapacitor: 2D Black Phosphorus–Doped and Phosphorus-Doped Materials. *Mater. Today Chem.* **2021**, *21*, 100480, doi:10.1016/j.mtchem.2021.100480.

114. Jin, H.; Wang, H.; Qi, Z.; Bin, D.-S.; Zhang, T.; Wan, Y.; Chen, J.; Chuang, C.; Lu, Y.-R.; Chan, T.-S.; et al. A Black Phosphorus–Graphite Composite Anode for Li-/Na-/K-Ion Batteries. *Angew. Chem.* **2020**, *132*, 2338–2342, doi:10.1002/ange.201913129.

115. Mulwa, W.M.; Ouma, C.N.M.; Onani, M.O.; Dejene, F.B. Energetic, Electronic and Optical Properties of Lanthanide Doped TiO2: An Ab Initio LDA+U Study. *J. Solid State Chem.* **2016**, *237*, 129–137, doi:10.1016/j.jssc.2016.02.003.

116. Ozkan, S.; Mazare, A.; Schmuki, P. Extracting the Limiting Factors in Photocurrent Measurements on TiO2 Nanotubes and Enhancing the Photoelectrochemical Properties by Nb Doping. *Electrochimica Acta* **2015**, *176*, 819–826, doi:10.1016/j.electacta.2015.07.023.

117. Nakata, K.; Fujishima, A. TiO2 Photocatalysis: Design and Applications. *J. Photochem. Photobiol. C Photochem. Rev.* **2012**, *13*, 169–189, doi:10.1016/j.jphotochemrev.2012.06.001.

118. Bavykin, D.V.; Walsh, F.C. *Titanate and Titania Nanotubes*; 2009; ISBN 978-1-84755-910-4.

119. Hou, X.; Aitola, K.; Lund, P.D. TiO2 Nanotubes for Dye-Sensitized Solar Cells—A Review. *Energy Sci. Eng.* **2021**, *9*, 921–937, doi:10.1002/ese3.831.

120. Bogdanowicz, R.; Dettlaff, A.; Skiba, F.; Trzcinski, K.; Szkoda, M.; Sobaszek, M.; Ficek, M.; Dec, B.; Macewicz, L.; Wyrębski, K.; et al. Enhanced Charge Storage Mechanism and Long-Term Cycling Stability in Diamondized Titania Nanocomposite Supercapacitors Operating in Aqueous Electrolytes. *J. Phys. Chem. C* **2020**, *124*, 15698–15712, doi:10.1021/acs.jpcc.0c02792.

121. Zhang, M.-M.; Chen, J.-Y.; Li, H.; Wang, C.-R. Recent Progress in Li-Ion Batteries with TiO2 Nanotube Anodes Grown by Electrochemical Anodization. *Rare Met.* **2021**, *40*, 249–271, doi:10.1007/s12598-020-01499-x.

122. Terracciano, M.; Galstyan, V.; Rea, I.; Casalino, M.; De Stefano, L.; Sbervegleri, G. Chemical Modification of TiO2 Nanotube Arrays for Label-Free Optical Biosensing Applications. *Appl. Surf. Sci.* **2017**, *419*, 235–240, doi:10.1016/j.apsusc.2017.05.029.

123. Yin, B.; Qian, Q.; Xiong, Z.; Jiang, H.; Lin, Y.; Feng, D. Growth Orientation Mechanism of TiO$\less$sub$\greater$2$\less$/Sub$\greater$ Nanotubes Fabricated by Anodization. *Nanotechnology* **2019**, *30*, 155702, doi:10.1088/1361-6528/aafd54.

124. One-Dimensional Titanium Dioxide Nanomaterials: Nanotubes | Chemical Reviews Available online: https://pubs.acs.org/doi/10.1021/cr500061m (accessed on 24 April 2022).

125. Macak, J.M.; Tsuchiya, H.; Ghicov, A.; Yasuda, K.; Hahn, R.; Bauer, S.; Schmuki, P. TiO2 Nanotubes: Self-Organized Electrochemical Formation, Properties and Applications. *Curr. Opin. Solid State Mater. Sci.* **2007**, *11*, 3–18, doi:10.1016/j.cossms.2007.08.004.

126. Kowalski, D.; Kim, D.; Schmuki, P. TiO2 Nanotubes, Nanochannels and Mesosponge: Self-Organized Formation and Applications. *Nano Today* **2013**, *8*, 235–264, doi:10.1016/j.nantod.2013.04.010.

127. Bavykin, D.V.; Gordeev, S.N.; Moskalenko, A.V.; Lapkin, A.A.; Walsh, F.C. Apparent Two-Dimensional Behavior of TiO2 Nanotubes Revealed by Light Absorption and Luminescence. *J. Phys. Chem. B* **2005**, *109*, 8565–8569, doi:10.1021/jp050762m.

128. Huang, J.-Y.; Zhang, K.-Q.; Lai, Y.-K. Fabrication, Modification, and Emerging Applications of TiO2 Nanotube Arrays by Electrochemical Synthesis: A Review. *Int. J. Photoenergy* **2013**, *2013*, e761971, doi:10.1155/2013/761971.

129. Zhang, D.; Chen, J.; Xiang, Q.; Li, Y.; Liu, M.; Liao, Y. Transition-Metal-Ion (Fe, Co, Cr, Mn, Etc.) Doping of TiO2 Nanotubes: A General Approach. *Inorg. Chem.* **2019**, *58*, 12511–12515, doi:10.1021/acs.inorgchem.9b01889.

130. Yalçın, Y.; Kılıç, M.; Çınar, Z. Fe+3-Doped TiO2: A Combined Experimental and Computational Approach to the Evaluation of Visible Light Activity. *Appl. Catal. B Environ.* **2010**, *99*, 469–477, doi:10.1016/j.apcatb.2010.05.013.

131. Yu, J.; Xiang, Q.; Zhou, M. Preparation, Characterization and Visible-Light-Driven Photocatalytic Activity of Fe-Doped Titania Nanorods and First-Principles Study for Electronic Structures. *Appl. Catal. B Environ.* **2009**, *90*, 595–602, doi:10.1016/j.apcatb.2009.04.021.

132. Sim, L.C.; Ng, K.W.; Ibrahim, S.; Saravanan, P. Preparation of Improved P-n Junction NiO/TiO_2 Nanotubes for Solar-Energy-Driven Light Photocatalysis. *Int. J. Photoenergy* **2013**, *2013*, e659013, doi:10.1155/2013/659013.

133. Tsui, L.; Zangari, G. Modification of TiO2 Nanotubes by Cu2O for Photoelectrochemical, Photocatalytic, and Photovoltaic Devices. *Electrochimica Acta* **2014**, *128*, 341–348, doi:10.1016/j.electacta.2013.09.150.

134. Perini, J.A.L.; Cardoso, J.C.; Brito, J.F. de; Zanoni, M.V.B. Contribution of Thin Films of ZrO2 on TiO2 Nanotubes Electrodes Applied in the Photoelectrocatalytic CO2 Conversion. *J. CO2 Util.* **2018**, *25*, 254–263, doi:10.1016/j.jcou.2018.04.005.

135. Lynch, R.P.; Ghicov, A.; Schmuki, P. A Photo-Electrochemical Investigation of Self-Organized TiO2 Nanotubes. *J. Electrochem. Soc.* **2010**, *157*, G76, doi:10.1149/1.3276455.

136. Pan, R.; Wu, Y.; Li, Z.; Fang, Z. Effect of Irradiation on Deposition of CdS in Fabricating Co-Axial Heterostructure of TiO2 Nanotube Arrays via Chemical Deposition. *Appl. Surf. Sci.* **2014**, *292*, 886–891, doi:10.1016/j.apsusc.2013.12.073.

137. Li, Q.; Kako, T.; Ye, J. PbS/CdS Nanocrystal-Sensitized Titanate Network Films: Enhanced Photocatalytic Activities and Super-Amphiphilicity. *J. Mater. Chem.* **2010**, *20*, 10187–10192, doi:10.1039/C0JM02111C.

138. Wang, L.S.; Xiao, M.W.; Huang, X.J.; Wu, Y.D. Synthesis, Characterization, and Photocatalytic Activities of Titanate Nanotubes Surface-Decorated by Zinc Oxide Nanoparticles. *J. Hazard. Mater.* **2009**, *161*, 49–54, doi:10.1016/j.jhazmat.2008.03.080.

139. Szkoda, M.; Siuzdak, K.; Lisowska-Oleksiak, A. Non-Metal Doped TiO2 Nanotube Arrays for High Efficiency Photocatalytic Decomposition of Organic Species in Water. *Phys. E Low-Dimens. Syst. Nanostructures* **2016**, *84*, 141–145, doi:10.1016/j.physe.2016.06.004.

140. Zheng, L.; Ye, X.; Deng, X.; Wang, Y.; Zhao, Y.; Shi, X.; Zheng, H. Black Phosphorus Quantum Dot-Sensitized TiO2 Nanotube Arrays with Enriched Oxygen Vacancies for Efficient Photoelectrochemical Water Splitting. *ACS Sustain. Chem. Eng.* **2020**, *8*, 15906–15914, doi:10.1021/acssuschemeng.0c04819.

141. Song, T.; Chen, H.; Li, Z.; Xu, Q.; Liu, H.; Wang, Y.; Xia, Y. Creating an Air-Stable Sulfur-Doped Black Phosphorus-TiO2 Composite as High-Performance Anode Material for Sodium-Ion Storage. *Adv. Funct. Mater.* **2019**, *29*, 1900535, doi:10.1002/adfm.201900535.

142. Qu, G.; Xia, T.; Zhou, W.; Zhang, X.; Zhang, H.; Hu, L.; Shi, J.; Yu, X.-F.; Jiang, G. Property–Activity Relationship of Black Phosphorus at the Nano–Bio Interface: From Molecules to Organisms. *Chem. Rev.* **2020**, *120*, 2288–2346, doi:10.1021/acs.chemrev.9b00445.

143. Liu, H.; Qian, Z.; Liao, G.; Wang, X. Integration of Magnetic Phase-Change Microcapsules with Black Phosphorus Nanosheets for Efficient Harvest of Solar Photothermal Energy. *ACS Appl. Energy Mater.* **2021**, *4*, 13248–13262, doi:10.1021/acsaem.1c02835.

144. Panizza, M.; Cerisola, G. Application of Diamond Electrodes to Electrochemical Processes. *Electrochimica Acta* **2005**, *51*, 191–199, doi:10.1016/j.electacta.2005.04.023.

145. T. Luong, J.H.; B. Male, K.; D. Glennon, J. Boron -Doped Diamond Electrode : Synthesis, Characterization, Functionalization and Analytical Applications. *Analyst* **2009**, *134*, 1965–1979, doi:10.1039/B910206J.

146. Periyasamy, S.; Lin, X.; Ganiyu, S.O.; Kamaraj, S.-K.; Thiam, A.; Liu, D. Insight into BDD Electrochemical Oxidation of Florfenicol in Water: Kinetics, Reaction Mechanism, and Toxicity. *Chemosphere* **2022**, *288*, 132433, doi:10.1016/j.chemosphere.2021.132433.

147. Schmalz, V.; Dittmar, T.; Haaken, D.; Worch, E. Electrochemical Disinfection of Biologically Treated Wastewater from Small Treatment Systems by Using Boron-Doped Diamond (BDD) Electrodes – Contribution for Direct Reuse of Domestic Wastewater. *Water Res.* **2009**, *43*, 5260–5266, doi:10.1016/j.watres.2009.08.036.

148. Einaga, Y. Diamond Electrodes for Electrochemical Analysis. *J. Appl. Electrochem.* **2010**, *40*, 1807–1816, doi:10.1007/s10800-010-0112-z.

149. Sun, J.; Lu, H.; Lin, H.; Du, L.; Huang, W.; Li, H.; Cui, T. Electrochemical Oxidation of Aqueous Phenol at Low Concentration Using Ti/BDD Electrode. *Sep. Purif. Technol.* **2012**, *88*, 116–120, doi:10.1016/j.seppur.2011.12.022.

150. Marton, M.; Michniak, P.; Behul, M.; Rehacek, V.; Vojs Stanova, A.; Redhammer, R.; Vojs, M. Bismuth Modified Boron Doped Diamond Electrode for Simultaneous Determination of Zn, Cd and Pb Ions by Square Wave Anodic Stripping Voltammetry: Influence of Boron Concentration and Surface Morphology. *Vacuum* **2019**, *167*, 182–188, doi:10.1016/j.vacuum.2019.06.012.

151. Zhang, C.; Wu, J.; Fu, D. Fractals in Several Electrode Materials. *Appl. Surf. Sci.* **2014**, *313*, 750–754, doi:10.1016/j.apsusc.2014.06.065.

152. Medeiros de Araújo, D.; Cañizares, P.; Martínez-Huitle, C.A.; Rodrigo, M.A. Electrochemical Conversion/Combustion of a Model Organic Pollutant on BDD Anode: Role of Sp3/Sp2 Ratio. *Electrochem. Commun.* **2014**, *47*, 37–40, doi:10.1016/j.elecom.2014.07.017.

153. Kissinger, P.T.; Heineman, W.R. Cyclic Voltammetry. *J. Chem. Educ.* **1983**, *60*, 702, doi:10.1021/ed060p702.

154. Wang, L.; Sofer, Z.; Pumera, M. Voltammetry of Layered Black Phosphorus: Electrochemistry of Multilayer Phosphorene. *ChemElectroChem* **2015**, *2*, 324–327, doi:10.1002/celc.201402363.

155. Niu, X.; Weng, W.; Yin, C.; Niu, Y.; Li, G.; Dong, R.; Men, Y.; Sun, W. Black Phosphorene Modified Glassy Carbon Electrode for the Sensitive Voltammetric

Detection of Rutin. *J. Electroanal. Chem.* **2018**, *811*, 78–83, doi:10.1016/j.jelechem.2018.01.038.

156. Li, X.; Niu, X.; Zhao, W.; Chen, W.; Yin, C.; Men, Y.; Li, G.; Sun, W. Black Phosphorene and PEDOT:PSS-Modified Electrode for Electrochemistry of Hemoglobin. *Electrochem. Commun.* **2018**, *86*, 68–71, doi:10.1016/j.elecom.2017.11.017.

157. Ivanishchev, A.V.; Churikov, A.V.; Ivanishcheva, I.A.; Ushakov, A.V. Lithium Diffusion in Li3V2(PO4)3-Based Electrodes: A Joint Analysis of Electrochemical Impedance, Cyclic Voltammetry, Pulse Chronoamperometry, and Chronopotentiometry Data. *Ionics* **2016**, *22*, 483–501, doi:10.1007/s11581-015-1568-y.

158. Xu, G.; Li, H.; R. Bati, A.S.; Bat-Erdene, M.; J. Nine, M.; Losic, D.; Chen, Y.; G. Shapter, J.; Batmunkh, M.; Ma, T. Nitrogen-Doped Phosphorene for Electrocatalytic Ammonia Synthesis. *J. Mater. Chem. A* **2020**, *8*, 15875–15883, doi:10.1039/D0TA03237A.

159. Mayorga-Martinez, C.C.; Sofer, Z.; Pumera, M. Binary Phosphorene Redox Behavior in Oxidoreductase Enzymatic Systems. *ACS Nano* **2019**, *13*, 13217–13224, doi:10.1021/acsnano.9b06230.

160. Vernon-Parry, K.D. Scanning Electron Microscopy: An Introduction. *III-Vs Rev.* **2000**, *13*, 40–44, doi:10.1016/S0961-1290(00)80006-X.

161. Zhang, X.; Xie, H.; Liu, Z.; Tan, C.; Luo, Z.; Li, H.; Lin, J.; Sun, L.; Chen, W.; Xu, Z.; et al. Black Phosphorus Quantum Dots. *Angew. Chem. Int. Ed.* **2015**, *54*, 3653–3657, doi:10.1002/anie.201409400.

162. Chen, H.; Huang, P.; Guo, D.; Xie, G. Anisotropic Mechanical Properties of Black Phosphorus Nanoribbons. *J. Phys. Chem. C* **2016**, *120*, 29491–29497, doi:10.1021/acs.jpcc.6b10644.

163. Eswaraiah, V.; Zeng, Q.; Long, Y.; Liu, Z. Black Phosphorus Nanosheets: Synthesis, Characterization and Applications. *Small* **2016**, *12*, 3480–3502, doi:10.1002/smll.201600032.

164. Sun, L.; Wang, X.; Wang, Y.; Xiao, D.; Cai, W.; Jing, Y.; Wang, Y.; Hu, F.; Zhang, Q. In-Situ Functionalization of Metal Electrodes for Advanced Asymmetric Supercapacitors. *Front. Chem.* **2019**, *7*, doi:10.3389/fchem.2019.00512.

165. Phakatkar, A.H.; Shahbazian-Yassar, R.; Shokuhfar, T. STEM-EDS and STEM-EELS Studies of Antibacterial Behavior of Phosphorene. *Microsc. Microanal.* **2020**, *26*, 2294–2297, doi:10.1017/S1431927620021108.

166. Yehliu, K.; Vander Wal, R.L.; Boehman, A.L. Development of an HRTEM Image Analysis Method to Quantify Carbon Nanostructure. *Combust. Flame* **2011**, *158*, 1837–1851, doi:10.1016/j.combustflame.2011.01.009.

167. Zhang, L.; Huang, H.; Zhang, B.; Gu, M.; Zhao, D.; Zhao, X.; Li, L.; Zhou, J.; Wu, K.; Cheng, Y.; et al. Structure and Properties of Violet Phosphorus and Its Phosphorene Exfoliation. *Angew. Chem.* **2020**, *132*, 1090–1096, doi:10.1002/ange.201912761.

168. Qiao, H.; Liu, H.; Huang, Z.; Ma, Q.; Luo, S.; Li, J.; Liu, Y.; Zhong, J.; Qi, X. Black Phosphorus Nanosheets Modified with Au Nanoparticles as High Conductivity and High Activity Electrocatalyst for Oxygen Evolution Reaction. *Adv. Energy Mater.* **2020**, *10*, 2002424, doi:10.1002/aenm.202002424.

169. Eaton, P.; West, P. *Atomic Force Microscopy*; Oxford University Press, 2010; ISBN 978-0-19-957045-4.

170. Mulvaney, S.P.; Keating, C.D. Raman Spectroscopy. *Anal. Chem.* **2000**, *72*, 145–158, doi:10.1021/a10000155.

171. Ribeiro, H.B.; Pimenta, M.A.; de Matos, C.J.S. Raman Spectroscopy in Black Phosphorus. *J. Raman Spectrosc.* **2018**, *49*, 76–90, doi:10.1002/jrs.5238.

172. Akhtar, M.; Anderson, G.; Zhao, R.; Alruqi, A.; Mroczkowska, J.E.; Sumanasekera, G.; Jasinski, J.B. Recent Advances in Synthesis, Properties, and Applications of Phosphorene. *Npj 2D Mater. Appl.* **2017**, *1*, 5, doi:10.1038/s41699-017-0007-5.

173. Boutahir, O.; Lakhlifi, S.; Abdelkader, S.A.A.; Boutahir, M.; Rahmani, A.; Chadli, H.; Mejía-López, J.; Rahmani, A. Force-Constant Model for the Vibrational Modes in Black-Phosphorene and Phosphorene Nanoribbons (PNRs). *Phys. E Low-Dimens. Syst. Nanostructures* **2021**, *132*, 114757, doi:10.1016/j.physe.2021.114757.

174. Feng, Y.; Zhou, J.; Du, Y.; Miao, F.; Duan, C.-G.; Wang, B.; Wan, X. Raman Spectra of Few-Layer Phosphorene Studied from First-Principles Calculations. *J. Phys. Condens. Matter* **2015**, *27*, 185302, doi:10.1088/0953-8984/27/18/185302.

175. Förster, H. UV/VIS Spectroscopy. In *Characterization I: -/-*; Karge, H.G., Weitkamp, J., Eds.; Molecular Sieves – Science and Technology; Springer: Berlin, Heidelberg, 2004; pp. 337–426 ISBN 978-3-540-69751-0.

176. Gao, L.-F.; Xu, J.-Y.; Zhu, Z.-Y.; Hu, C.-X.; Zhang, L.; Wang, Q.; Zhang, H.-L. Small Molecule-Assisted Fabrication of Black Phosphorus Quantum Dots with a Broadband Nonlinear Optical Response. *Nanoscale* **2016**, *8*, 15132–15136, doi:10.1039/C6NR04773D.

177. Pan, L.; Zhu, X.-D.; Sun, K.-N.; Liu, Y.-T.; Xie, X.-M.; Ye, X.-Y. Molecular Level Distribution of Black Phosphorus Quantum Dots on Nitrogen-Doped Graphene Nanosheets for Superior Lithium Storage. *Nano Energy* **2016**, *30*, 347–354, doi:10.1016/j.nanoen.2016.10.019.

178. Liu, H.; Lian, P.; Zhang, Q.; Yang, Y.; Mei, Y. The Preparation of Holey Phosphorene by Electrochemical Assistance. *Electrochem. Commun.* **2019**, *98*, 124–128, doi:10.1016/j.elecom.2018.12.007.

179. Shen, Z.; Hu, Z.; Wang, W.; Lee, S.-F.; Li, Y.; Gu, T.; Yu, J.C. Crystalline Phosphorus Fibers: Controllable Synthesis and Visible-Light-Driven Photocatalytic Activity. **2012**, 5.

180. Xiao, H.; Xia, Y.; Gan, Y.; Huang, H.; Liang, C.; Tao, X.; Xu, L.; Zhang, W. Facile Fabrication of Red Phosphorus/TiO2 Composites for Lithium Ion Batteries. *RSC Adv.* **2014**, *4*, 60914–60919, doi:10.1039/C4RA09836F.

181. Durig, J.R.; Casper, J.M. On the Vibrational Spectra and Structure of Red Phosphorus11Taken in Part from the Thesis of J.M. Casper Submitted to the Department of Chemistry in Partial Fulfillment of the Ph. D. Degree. *J. Mol. Struct.* **1970**, *5*, 351–358, doi:10.1016/0022-2860(70)80040-0.

182. Rissi, E.N.; Soignard, E.; McKiernan, K.A.; Benmore, Chris.J.; Yarger, J.L. Pressure-Induced Crystallization of Amorphous Red Phosphorus. *Solid State Commun.* **2012**, *152*, 390–394, doi:10.1016/j.ssc.2011.12.003.

183. Pawbake, A.S.; Erande, M.B.; Jadkar, S.R.; Late, D.J. Temperature Dependent Raman Spectroscopy of Electrochemically Exfoliated Few Layer Black Phosphorus Nanosheets. *RSC Adv.* **2016**, *6*, 76551–76555, doi:10.1039/C6RA15996F.

184. Gui, R.; Jin, H.; Wang, Z.; Li, J. Black Phosphorus Quantum Dots: Synthesis, Properties, Functionalized Modification and Applications. *Chem. Soc. Rev.* **2018**, *47*, 6795–6823, doi:10.1039/C8CS00387D.

185. Pang, J.; Bachmatiuk, A.; Yin, Y.; Trzebicka, B.; Zhao, L.; Fu, L.; Mendes, R.G.; Gemming, T.; Liu, Z.; Rummeli, M.H. Applications of Phosphorene and Black Phosphorus in Energy Conversion and Storage Devices. *Adv. Energy Mater.* **2018**, *8*, 1702093, doi:10.1002/aenm.201702093.

186. Gómez-Pérez, J.; Kónya, Z.; Kukovecz, Á. Acetone Improves the Topographical Homogeneity of Liquid Phase Exfoliated Few-Layer Black Phosphorus Flakes. *Nanotechnology* **2018**, *29*, 365303, doi:10.1088/1361-6528/aacc23.

187. Fei, R.; Yang, L. Lattice Vibrational Modes and Raman Scattering Spectra of Strained Phosphorene. *Appl. Phys. Lett.* **2014**, *105*, 083120, doi:10.1063/1.4894273.

188. Liang, S.; Hasan, M.N.; Seo, J.-H. Direct Observation of Raman Spectra in Black Phosphorus under Uniaxial Strain Conditions. *Nanomaterials* **2019**, *9*, 566, doi:10.3390/nano9040566.

189. Wang, M.; Xu, Z.; Zhang, X.; Yang, J.; Liu, J.; Qiao, G.; Liu, G. B-Modified Phosphorene for N2 Fixation: A Highly Efficient Metal-Free Photocatalyst. *Appl. Surf. Sci.* **2021**, *554*, 149614, doi:10.1016/j.apsusc.2021.149614.

190. Pan, S.; He, J.; Wang, C.; Zuo, Y. Exfoliation of Two-Dimensional Phosphorene Sheets with Enhanced Photocatalytic Activity under Simulated Sunlight. *Mater. Lett.* **2018**, *212*, 311–314, doi:10.1016/j.matlet.2017.10.090.

191. Taheri, R.; Farbod, M. Superb Photocatalytic Performance of Single/Few Layer Phosphorene Prepared via Sonication Method. *Phys. E Low-Dimens. Syst. Nanostructures* **2020**, *119*, 114009, doi:10.1016/j.physe.2020.114009.

192. Lee, H.U.; Park, S.Y.; Lee, S.C.; Choi, S.; Seo, S.; Kim, H.; Won, J.; Choi, K.; Kang, K.S.; Park, H.G.; et al. Black Phosphorus (BP) Nanodots for Potential Biomedical Applications. *Small* **2016**, *12*, 214–219, doi:10.1002/smll.201502756.

193. Woomer, A.H.; Farnsworth, T.W.; Hu, J.; Wells, R.A.; Donley, C.L.; Warren, S.C. Phosphorene: Synthesis, Scale-Up, and Quantitative Optical Spectroscopy. *ACS Nano* **2015**, *9*, 8869–8884, doi:10.1021/acsnano.5b02599.

194. Lin, S.; Chui, Y.; Li, Y.; Lau, S.P. Liquid-Phase Exfoliation of Black Phosphorus and Its Applications. *FlatChem* **2017**, *2*, 15–37, doi:10.1016/j.flatc.2017.03.001.

195. Zhang, Y.; Wang, H.; Luo, Z.; Tan, H.T.; Li, B.; Sun, S.; Li, Z.; Zong, Y.; Xu, Z.J.; Yang, Y.; et al. An Air-Stable Densely Packed Phosphorene–Graphene Composite Toward Advanced Lithium Storage Properties. *Adv. Energy Mater.* **2016**, *6*, 1600453, doi:10.1002/aenm.201600453.

196. Musa, M.R.K.; Zhang, C.; Rajapakse, M.; Jasinski, J.B.; Sumanasekera, G.; Yu, M. Li Interaction-Induced Phase Transition from Black to Blue Phosphorene. *Phys. Rev. Mater.* **2021**, *5*, 024007, doi:10.1103/PhysRevMaterials.5.024007.

197. Dettlaff, A.; Skowierzak, G.; MacEwicz, Ł.; Sobaszek, M.; Karczewski, J.; Sawczak, M.; Ryl, J.; Ossowski, T.; Bogdanowicz, R. Electrochemical Stability of Few-Layered Phosphorene Flakes on Boron-Doped Diamond: A Wide Potential Range of Studies in Aqueous Solutions. *J. Phys. Chem. C* **2019**, *123*, 20233–20240, doi:10.1021/acs.jpcc.9b03028.

198. Yang, A.; Wang, D.; Wang, X.; Zhang, D.; Koratkar, N.; Rong, M. Recent Advances in Phosphorene as a Sensing Material. *Nano Today* **2018**, *20*, 13–32, doi:10.1016/j.nantod.2018.04.001.

199. Tao, Y.; Huang, T.; Ding, C.; Yu, F.; Tan, D.; Wang, F.; Xie, Q.; Yao, S. Few-Layer Phosphorene: An Emerging Electrode Material for Electrochemical Energy Storage. *Appl. Mater. Today* **2019**, *15*, 18–33, doi:10.1016/j.apmt.2018.12.008.

200. Kaewmaraya, T.; Ngamwongwan, L.; Moontragoon, P.; Karton, A.; Hussain, T. Drastic Improvement in Gas-Sensing Characteristics of Phosphorene Nanosheets under Vacancy Defects and Elemental Functionalization. *J. Phys. Chem. C* **2018**, *122*, 20186–20193, doi:10.1021/acs.jpcc.8b06803.

201. Zhu, Y.; Xie, Z.; Li, J.; Liu, Y.; Li, C.; Liang, W.; Huang, W.; Kang, J.; Cheng, F.; Kang, L.; et al. From Phosphorus to Phosphorene: Applications in Disease Theranostics. *Coord. Chem. Rev.* **2021**, *446*, 214110, doi:10.1016/j.ccr.2021.214110.

202. Jiang, H.; Xia, Q.; Liu, D.; Ling, K. Calcium-Cation-Doped Polydopamine-Modified 2D Black Phosphorus Nanosheets as a Robust Platform for Sensitive and Specific Biomolecule Sensing. *Anal. Chim. Acta* **2020**, *1121*, 1–10, doi:10.1016/j.aca.2020.04.072.

203. Rabiei Baboukani, A.; Khakpour, I.; Drozd, V.; Wang, C. Liquid-Based Exfoliation of Black Phosphorus into Phosphorene and Its Application for Energy Storage Devices. *Small Struct.* **2021**, *2*, 2000148, doi:10.1002/sstr.202000148.

204. Jeon, Y.; Rhee, D.; Wu, B.; Mazanek, V.; Kim, I.S.; Son, D.; Sofer, Z.; Kang, J. Electrochemically Exfoliated Phosphorene Nanosheet Thin Films for Wafer-Scale near-Infrared Phototransistor Array. *Npj 2D Mater. Appl.* **2022**, *6*, 1–8, doi:10.1038/s41699-022-00360-2.

205. Li, W.; Li, M.; Li, J.; Liang, J.; Adair, K.R.; Hu, Y.; Xiao, Q.; Cui, X.; Li, R.; Brandys, F.; et al. Phosphorene Nanosheets Exfoliated from Low-Cost and High-Quality Black

Phosphorus for Hydrogen Evolution. *ACS Appl. Nano Mater.* **2020**, *3*, 7508–7515, doi:10.1021/acsanm.0c01101.

206. Liu, Y.; Bo, M.; Yang, X.; Zhang, P.; Q. Sun, C.; Huang, Y. Size Modulation Electronic and Optical Properties of Phosphorene Nanoribbons: DFT–BOLS Approximation. *Phys. Chem. Chem. Phys.* **2017**, *19*, 5304–5309, doi:10.1039/C6CP08011A.

207. Jing, Y.; Zhang, X.; Zhou, Z. Phosphorene: What Can We Know from Computations? *WIREs Comput. Mol. Sci.* **2016**, *6*, 5–19, doi:10.1002/wcms.1234.

208. Lee, S.; Yang, F.; Suh, J.; Yang, S.; Lee, Y.; Li, G.; Sung Choe, H.; Suslu, A.; Chen, Y.; Ko, C.; et al. Anisotropic In-Plane Thermal Conductivity of Black Phosphorus Nanoribbons at Temperatures Higher than 100 K. *Nat. Commun.* **2015**, *6*, 8573, doi:10.1038/ncomms9573.

209. Li, L.L.; Peeters, F.M. Quantum Transport in Defective Phosphorene Nanoribbons: Effects of Atomic Vacancies. *Phys. Rev. B* **2018**, *97*, 075414, doi:10.1103/PhysRevB.97.075414.

210. G Klapetek P, Nečas D, Anderson C: Gwyddion user guide.[http://gwyddion.net].

211. Takao, Y.; Asahina, H.; Morita, A. Electronic Structure of Black Phosphorus in Tight Binding Approach. *J. Phys. Soc. Jpn.* **1981**, *50*, 3362–3369, doi:10.1143/JPSJ.50.3362.

212. Qiao, J.; Kong, X.; Hu, Z.-X.; Yang, F.; Ji, W. High-Mobility Transport Anisotropy and Linear Dichroism in Few-Layer Black Phosphorus. *Nat. Commun.* **2014**, *5*, 4475, doi:10.1038/ncomms5475.

213. Macewicz, L.; Pyrchla, K.; Bogdanowicz, R.; Sumanasekera, G.; Jasinski, J.B. Chemical Vapor Transport Route toward Black Phosphorus Nanobelts and Nanoribbons. *J. Phys. Chem. Lett.* **2021**, *12*, 8347–8354, doi:10.1021/acs.jpclett.1c02064.

214. Liu, H.; Neal, A.T.; Zhu, Z.; Luo, Z.; Xu, X.; Tománek, D.; Ye, P.D. Phosphorene: An Unexplored 2D Semiconductor with a High Hole Mobility. *ACS Nano* **2014**, *8*, 4033–4041, doi:10.1021/nn501226z.

215. Akhtar, M.; Zhang, C.; Rajapakse, M.; Musa, M.R.K.; Yu, M.; Sumanasekera, G.; Jasinski, J.B. Bilayer Phosphorene under High Pressure: In Situ Raman Spectroscopy. *Phys. Chem. Chem. Phys.* **2019**, *21*, 7298–7304, doi:10.1039/C9CP00816K.

216. Favron, A.; Goudreault, F.A.; Gosselin, V.; Groulx, J.; Côté, M.; Leonelli, R.; Germain, J.-F.; Phaneuf-L'Heureux, A.-L.; Francoeur, S.; Martel, R. Second-Order Raman Scattering in Exfoliated Black Phosphorus. *Nano Lett.* **2018**, *18*, 1018–1027, doi:10.1021/acs.nanolett.7b04486.

217. Sorkin, V.; Zhang, Y.W. The Deformation and Failure Behaviour of Phosphorene Nanoribbons under Uniaxial Tensile Strain. *2D Mater.* **2015**, *2*, 035007, doi:10.1088/2053-1583/2/3/035007.

218. Tran, V.; Yang, L. Scaling Laws for the Band Gap and Optical Response of Phosphorene Nanoribbons. *Phys. Rev. B* **2014**, *89*, 245407, doi:10.1103/PhysRevB.89.245407.

219. Neupane, B.; Tang, H.; Nepal, N.K.; Ruzsinszky, A. Bending as a Control Knob for the Electronic and Optical Properties of Phosphorene Nanoribbons. *Phys. Rev. Mater.* **2022**, *6*, 014010, doi:10.1103/PhysRevMaterials.6.014010.

220. Wu, Q.; Shen, L.; Yang, M.; Cai, Y.; Huang, Z.; Feng, Y.P. Electronic and Transport Properties of Phosphorene Nanoribbons. *Phys. Rev. B* **2015**, *92*, 035436, doi:10.1103/PhysRevB.92.035436.

221. Poljak, M.; Suligoj, T. The Potential of Phosphorene Nanoribbons as Channel Material for Ultrascaled Transistors. *IEEE Trans. Electron Devices* **2018**, *65*, 290–294, doi:10.1109/TED.2017.2771345.

222. Meshginqalam, B.; Barvestani, J. Vacancy Defected Blue and Black Phosphorene Nanoribbons as Gas Sensor of NOx and SOx Molecules. *Appl. Surf. Sci.* **2020**, *526*, 146692, doi:10.1016/j.apsusc.2020.146692.

223. Lv, Y.; Huang, Q.; Chang, S.; Wang, H.; He, J. Highly Sensitive Bilayer Phosphorene Nanoribbon Pressure Sensor Based on the Energy Gap Modulation Mechanism: A Theoretical Study. *IEEE Electron Device Lett.* **2017**, *38*, 1313–1316, doi:10.1109/LED.2017.2734909.

224. Paramasivam, I.; Jha, H.; Liu, N.; Schmuki, P. A Review of Photocatalysis Using Self-Organized TiO2 Nanotubes and Other Ordered Oxide Nanostructures. *Small* **2012**, *8*, 3073–3103, doi:10.1002/smll.201200564.

225. Szaciłowski, K.; Macyk, W.; Stochel, G. Light-Driven OR and XOR Programmable Chemical Logic Gates. *J. Am. Chem. Soc.* **2006**, *128*, 4550–4551, doi:10.1021/ja060694x.

226. Licht, S.; Myung, N.; Sun, Y. A Light Addressable Photoelectrochemical Cyanide Sensor. *Anal. Chem.* **1996**, *68*, 954–959, doi:10.1021/ac9507449.

227. Liu, Z.; Zhou, Y.; Li, Z.; Wang, Y.; Ge, C. Preparation and Characterization of (Metal, Nitrogen)-Codoped TiO2 by TiCl4 Sol-Gel Auto-Igniting Synthesis. *Rare Met.* **2007**, *26*, 263–270, doi:10.1016/S1001-0521(07)60212-5.

228. Di Paola, A.; Marcì, G.; Palmisano, L.; Schiavello, M.; Uosaki, K.; Ikeda, S.; Ohtani, B. Preparation of Polycrystalline TiO2 Photocatalysts Impregnated with Various Transition Metal Ions: Characterization and Photocatalytic Activity for the Degradation of 4-Nitrophenol. *J. Phys. Chem. B* **2002**, *106*, 637–645, doi:10.1021/jp013074l.

229. Qu, A.; Xie, H.; Xu, X.; Zhang, Y.; Wen, S.; Cui, Y. High Quantum Yield Graphene Quantum Dots Decorated TiO2 Nanotubes for Enhancing Photocatalytic Activity. *Appl. Surf. Sci.* **2016**, *375*, 230–241, doi:10.1016/j.apsusc.2016.03.077.

230. Mohammadi, T.; Sharifi, S.; Ghayeb, Y.; Sharifi, T.; Momeni, M.M. Photoelectrochemical Water Splitting and H2 Generation Enhancement Using an Effective Surface Modification of W-Doped TiO2 Nanotubes (WT) with Co-Deposition of Transition Metal Ions. *Sustainability* **2022**, *14*, 13251, doi:10.3390/su142013251.

231. Soares, P.; Dias-Netipanyj, M.F.; Elifio-Esposito, S.; Leszczak, V.; Popat, K. Effects of Calcium and Phosphorus Incorporation on the Properties and Bioactivity of TiO2 Nanotubes. *J. Biomater. Appl.* **2018**, *33*, 410–421, doi:10.1177/0885328218797549.

232. Peak Analysis Available online: https://www.originlab.com/index.aspx?go=products/origin/dataanalysis/peakanalysis.

233. Roy, P.; Berger, S.; Schmuki, P. TiO2 Nanotubes: Synthesis and Applications. *Angew. Chem. Int. Ed.* **2011**, *50*, 2904–2939, doi:10.1002/anie.201001374.

234. Carvalho, A.; Wang, M.; Zhu, X.; Rodin, A.S.; Su, H.; Neto, A.H.C. Phosphorene: From Theory to Applications. *Nat. Rev. Mater.* **2016**, *1*, 16061, doi:10.1038/natrevmats.2016.61.

235. Shi, H.; Ge, S.; Wang, Y.; Gao, C.; Yu, J. Wide-Spectrum-Responsive Paper-Supported Photoelectrochemical Sensing Platform Based on Black Phosphorus-Sensitized TiO2. *ACS Appl. Mater. Interfaces* **2019**, *11*, 41062–41068, doi:10.1021/acsami.9b14555.

236. Luo, Y.; Wu, H.; Liu, L.; Li, Q.; Jiang, K.; Fan, S.; Li, J.; Wang, J. TiO2-Nanocoated Black Phosphorus Electrodes with Improved Electrochemical Performance. *ACS Appl. Mater. Interfaces* **2018**, *10*, 36058–36066, doi:10.1021/acsami.8b14703.

237. Zheng, L.; Ye, X.; Deng, X.; Wang, Y.; Zhao, Y.; Shi, X.; Zheng, H. Black Phosphorus Quantum Dot-Sensitized TiO2 Nanotube Arrays with Enriched Oxygen Vacancies for Efficient Photoelectrochemical Water Splitting. *ACS Sustain. Chem. Eng.* **2020**, *8*, 15906–15914, doi:10.1021/acssuschemeng.0c04819.

238. Bhuvaneswari, R.; Nagarajan, V.; Chandiramouli, R. Molecular Interaction Studies of Styrene on Single and Double-Walled Square-Octagon Phosphorene Nanotubes – First-Principles Investigation. *Chem. Phys. Lett.* **2021**, *785*, 139149, doi:10.1016/j.cplett.2021.139149.

239. Kim, J.-S.; Liu, Y.; Zhu, W.; Kim, S.; Wu, D.; Tao, L.; Dodabalapur, A.; Lai, K.; Akinwande, D. Toward Air-Stable Multilayer Phosphorene Thin-Films and Transistors. *Sci. Rep.* **2015**, *5*, 8989, doi:10.1038/srep08989.

240. Han, R.; Feng, S.; Sun, D.-M.; Cheng, H.-M. Properties and Photodetector Applications of Two-Dimensional Black Arsenic Phosphorus and Black Phosphorus. *Sci. China Inf. Sci.* **2021**, *64*, 140402, doi:10.1007/s11432-020-3172-1.

241. Liu, Y.; Wang, H.; Wang, S.; Wang, Y.; Wang, Y.; Guo, Z.; Xiao, S.; Yao, Y.; Song, Q.; Zhang, H.; et al. Highly Efficient Silicon Photonic Microheater Based on Black Arsenic–Phosphorus. *Adv. Opt. Mater.* **2020**, *8*, 1901526, doi:10.1002/adom.201901526.

242. Ghashghaee, M.; Azizi, Z.; Ghambarian, M. Substitutional Doping of Black Phosphorene with Boron, Nitrogen, and Arsenic for Sulfur Trioxide Detection: A Theoretical Perspective. *J. Sulfur Chem.* **2020**, *41*, 399–420, doi:10.1080/17415993.2020.1752692.

243. Liu, B.; Köpf, M.; Abbas, A.N.; Wang, X.; Guo, Q.; Jia, Y.; Xia, F.; Weihrich, R.; Bachhuber, F.; Pielnhofer, F.; et al. Black Arsenic-Phosphorus: Layered Anisotropic

Infrared Semiconductors with Highly Tunable Compositions and Properties. *Adv. Mater. Deerfield Beach Fla* **2015**, *27*, 4423–4429, doi:10.1002/adma.201501758.

244. Shi, X.; Wang, T.; Wang, J.; Xu, Y.; Yang, Z.; Yu, Q.; Wu, J.; Zhang, K.; Zhou, P. Synthesis of Black Arsenic-Phosphorus and Its Application for Er-Doped Fiber Ultrashort Laser Generation. *Opt. Mater. Express* **2019**, *9*, 2348, doi:10.1364/OME.9.002348.

245. Karki, B.; Rajapakse, M.; Sumanasekera, G.U.; Jasinski, J.B. Structural and Thermoelectric Properties of Black Arsenic–Phosphorus. *ACS Appl. Energy Mater.* **2020**, *3*, 8543–8551, doi:10.1021/acsaem.0c01172.

246. Hou, Y.; Ma, S.; Liu, Q.; Zhang, S.; Chu, Y.; Hao, X.; Han, B.; Xu, B. 2D Black Arsenic Phosphorus and Its Application for Anodes of Lithium Ion Batteries. *CrystEngComm* **2020**, *22*, 8228–8235, doi:10.1039/D0CE01226B.

247. Zhang, S.; Yang, J.; Xu, R.; Wang, F.; Li, W.; Ghufran, M.; Zhang, Y.-W.; Yu, Z.; Zhang, G.; Qin, Q.; et al. Extraordinary Photoluminescence and Strong Temperature/Angle-Dependent Raman Responses in Few-Layer Phosphorene. *ACS Nano* **2014**, *8*, 9590–9596, doi:10.1021/nn503893j.

248. Young, E.P.; Park, J.; Bai, T.; Choi, C.; DeBlock, R.H.; Lange, M.; Poust, S.; Tice, J.; Cheung, C.; Dunn, B.S.; et al. Wafer-Scale Black Arsenic–Phosphorus Thin-Film Synthesis Validated with Density Functional Perturbation Theory Predictions. *ACS Appl. Nano Mater.* **2018**, *1*, 4737–4745, doi:10.1021/acsanm.8b00951.

249. Karki, B.; Freelon, B.; Rajapakse, M.; Musa, R.; Riyadh, S.M.S.; Morris, B.; Abu, U.; Yu, M.; Sumanasekera, G.; Jasinski, J.B. Strain-Induced Vibrational Properties of Few Layer Black Phosphorus and MoTe2 via Raman Spectroscopy. *Nanotechnology* **2020**, *31*, 425707, doi:10.1088/1361-6528/aba13e.

250. Weng, S.; Zhen, W.; Li, Y.; Yan, X.; Han, H.; Huang, H.; Pi, L.; Zhu, W.; Li, H.; Zhang, C. Air-Stable Wide-Bandgap 2D Semiconductor ZnIn2S4. *Phys. Status Solidi RRL – Rapid Res. Lett.* **2020**, *14*, 2000085, doi:10.1002/pssr.202000085.

251. Zhao, Y.; Qiao, J.; Yu, Z.; Yu, P.; Xu, K.; Lau, S.P.; Zhou, W.; Liu, Z.; Wang, X.; Ji, W.; et al. High-Electron-Mobility and Air-Stable 2D Layered PtSe $_2$ FETs. *Adv. Mater.* **2017**, *29*, 1604230, doi:10.1002/adma.201604230.

252. Carey, T.; Arbab, A.; Anzi, L.; Bristow, H.; Hui, F.; Bohm, S.; Wyatt-Moon, G.; Flewitt, A.; Wadsworth, A.; Gasparini, N.; et al. Inkjet Printed Circuits with 2D Semiconductor Inks for High-Performance Electronics. *Adv. Electron. Mater.* **2021**, *7*, 2100112, doi:10.1002/aelm.202100112.

253. Na, J.; Park, K.; Kim, J.T.; Choi, W.K.; Song, Y.-W. Air-Stable Few-Layer Black Phosphorus Phototransistor for near-Infrared Detection. *Nanotechnology* **2017**, *28*, 085201, doi:10.1088/1361-6528/aa55e4.

254. Zhu, W.; Yogeesh, M.N.; Yang, S.; Aldave, S.H.; Kim, J.-S.; Sonde, S.; Tao, L.; Lu, N.; Akinwande, D. Flexible Black Phosphorus Ambipolar Transistors, Circuits and AM Demodulator. *Nano Lett.* **2015**, *15*, 1883–1890, doi:10.1021/nl5047329.

255. Wu, F.; Li, Q.; Wang, P.; Xia, H.; Wang, Z.; Wang, Y.; Luo, M.; Chen, L.; Chen, F.; Miao, J.; et al. High Efficiency and Fast van Der Waals Hetero-Photodiodes with a Unilateral Depletion Region. *Nat. Commun.* **2019**, *10*, 4663, doi:10.1038/s41467-019-12707-3.

256. Zhou, W.; Zhang, S.; Wang, Y.; Guo, S.; Qu, H.; Bai, P.; Li, Z.; Zeng, H. Anisotropic In-Plane Ballistic Transport in Monolayer Black Arsenic-Phosphorus FETs. *Adv. Electron. Mater.* **2020**, *6*, 1901281, doi:10.1002/aelm.201901281.

257. Pradhan, N.R.; Garcia, C.; Lucking, M.C.; Pakhira, S.; Martinez, J.; Rosenmann, D.; Divan, R.; Sumant, A.V.; Terrones, H.; Mendoza-Cortes, J.L.; et al. Raman and Electrical Transport Properties of Few-Layered Arsenic-Doped Black Phosphorus. *Nanoscale* **2019**, *11*, 18449–18463, doi:10.1039/C9NR04598H.

258. Ambroziak, R.; Hołdyński, M.; Płociński, T.; Pisarek, M.; Kudelski, A. Cubic Silver Nanoparticles Fixed on TiO2 Nanotubes as Simple and Efficient Substrates for Surface Enhanced Raman Scattering. *Materials* **2019**, *12*, 3373, doi:10.3390/ma12203373.

259. Antonatos, N.; Mazánek, V.; Lazar, P.; Sturala, J.; Sofer, Z. Acetonitrile-Assisted Exfoliation of Layered Grey and Black Arsenic: Contrasting Properties. *Nanoscale Adv.* **2020**, *2*, 1282–1289, doi:10.1039/C9NA00754G.

260. Liang, J.; Hu, Y.; Zhang, K.; Wang, Y.; Song, X.; Tao, A.; Liu, Y.; Jin, Z. 2D Layered Black Arsenic-Phosphorus Materials: Synthesis, Properties, and Device Applications. *Nano Res.* **2022**, *15*, 3737–3752, doi:10.1007/s12274-021-3974-y.

261. Wang, X.; Wang, Y.; Ye, X.; Wu, T.; Deng, H.; Wu, P.; Li, C. Sensing Platform for Neuron Specific Enolase Based on Molecularly Imprinted Polymerized Ionic Liquids in between Gold Nanoarrays. *Biosens. Bioelectron.* **2018**, *99*, 34–39, doi:10.1016/j.bios.2017.07.037.

262. Song, H.Y.; Wong, T.I.; Sadovoy, A.; Wu, L.; Bai, P.; Deng, J.; Guo, S.; Wang, Y.; Knoll, W.; Zhou, X. Imprinted Gold 2D Nanoarray for Highly Sensitive and Convenient PSA Detection via Plasmon Excited Quantum Dots. *Lab. Chip* **2014**, *15*, 253–263, doi:10.1039/C4LC00978A.

263. Fan, X.; Hao, Q.; Jin, R.; Huang, H.; Luo, Z.; Yang, X.; Chen, Y.; Han, X.; Sun, M.; Jing, Q.; et al. Assembly of Gold Nanoparticles into Aluminum Nanobowl Array. *Sci. Rep.* **2017**, *7*, 2322, doi:10.1038/s41598-017-02552-z.

264. Gao, Z.; Kang, H.; Naylor, C.H.; Streller, F.; Ducos, P.; Serrano, M.D.; Ping, J.; Zauberman, J.; Rajesh; Carpick, R.W.; et al. Scalable Production of Sensor Arrays Based on High-Mobility Hybrid Graphene Field Effect Transistors. *ACS Appl. Mater. Interfaces* **2016**, *8*, 27546–27552, doi:10.1021/acsami.6b09238.

265. Ban, T.; Uenuma, M.; Migita, S.; Okamoto, N.; Ishikawa, Y.; Uraoka, Y.; Yamashita, I.; Yamamoto, S. One-Dimensional Array of Gold Nanoparticles Fabricated Using Biotemplate and Its Application to Fine FET. *Jpn. J. Appl. Phys.* **2018**, *57*, 06HC05, doi:10.7567/JJAP.57.06HC05.

266. Živcová, Z.V.; Frank, O.; Petrák, V.; Tarábková, H.; Vacík, J.; Nesládek, M.; Kavan, L. Electrochemistry and in Situ Raman Spectroelectrochemistry of Low and High Quality

Boron Doped Diamond Layers in Aqueous Electrolyte Solution. *Electrochimica Acta* **2013**, *87*, 518–525, doi:10.1016/j.electacta.2012.09.031.

267. Muzyka, K.; Sun, J.; Fereja, T.H.; Lan, Y.; Zhang, W.; Xu, G. Boron-Doped Diamond: Current Progress and Challenges in View of Electroanalytical Applications. *Anal. Methods* **2019**, *11*, 397–414, doi:10.1039/C8AY02197J.

268. Dornellas, R.M.; Franchini, R.A.A.; da Silva, A.R.; Matos, R.C.; Aucelio, R.Q. Determination of the Fungicide Kresoxim-Methyl in Grape Juices Using Square-Wave Voltammetry and a Boron-Doped Diamond Electrode. *J. Electroanal. Chem.* **2013**, *708*, 46–53, doi:10.1016/j.jelechem.2013.09.015.

269. Jiwanti, P.K.; Natsui, K.; Nakata, K.; Einaga, Y. The Electrochemical Production of C2/C3 Species from Carbon Dioxide on Copper-Modified Boron-Doped Diamond Electrodes. *Electrochimica Acta* **2018**, *266*, 414–419, doi:10.1016/j.electacta.2018.02.041.

270. Hanawa, A.; Asai, K.; Ogata, G.; Hibino, H.; Einaga, Y. Electrochemical Measurement of Lamotrigine Using Boron-Doped Diamond Electrodes. *Electrochimica Acta* **2018**, *271*, 35–40, doi:10.1016/j.electacta.2018.03.112.

271. Bogdanowicz, R.; Sawczak, M.; Niedzialkowski, P.; Zieba, P.; Finke, B.; Ryl, J.; Karczewski, J.; Ossowski, T. Novel Functionalization of Boron-Doped Diamond by Microwave Pulsed-Plasma Polymerized Allylamine Film. *J. Phys. Chem. C* **2014**, *118*, 8014–8025, doi:10.1021/jp5003947.

272. Ashcheulov, P.; Taylor, A.; Vlčková Živcová, Z.; Hubík, P.; Honolka, J.; Vondráček, M.; Remzová, M.; Kopeček, J.; Klimša, L.; Lorinčik, J.; et al. Low Temperature Synthesis of Transparent Conductive Boron Doped Diamond Films for Optoelectronic Applications: Role of Hydrogen on the Electrical Properties. *Appl. Mater. Today* **2020**, *19*, 100633, doi:10.1016/j.apmt.2020.100633.

273. Vishnoi, P.; Mazumder, M.; Pati, S.K.; Rao, C.N.R. Arsenene Nanosheets and Nanodots. *New J. Chem.* **2018**, *42*, 14091–14095, doi:10.1039/C8NJ03186J.

274. Rahman, M.Z.; Kwong, C.W.; Davey, K.; Qiao, S.Z. 2D Phosphorene as a Water Splitting Photocatalyst: Fundamentals to Applications. *Energy Environ. Sci.* **2016**, *9*, 709–728, doi:10.1039/C5EE03732H.